Swansea University
Prifysgol Abertawe

Developing and Assessing a Nuclear Magnetic Resonance Method for Measuring Nuclear Spin Conversion of Ground State Polyatomic Molecules

Thomas Carter

Swansea University

Submitted to Swansea University in fulfilment of the requirements for the degree programme:

Doctor of Philosophy in Chemistry

March 2026

Abstract:

The phenomenon of nuclear spin conversion is observed in a wide variety of molecules with a wide variety of experimental methods. This thesis presents and NMR method for measuring nuclear spin conversion in water isolated in an argon cryomatrix. The work serves as a complement to existing fourier transform infrared spectroscopy (FTIR) studies of nuclear spin conversion in the same system. FTIR has traditionally been preferred over NMR due to its significantly higher sensitivity, however, the results obtained here evidence that measuring the nuclear spin conversion (NSC) of matrix-isolated water samples with NMR is entirely feasible, with potential to outperform FTIR in high concentration measurements where the presence of broad background peaks renders FTIR infeasible.

As a compliment to this work, the thesis also discusses experiments attempting to measure hyperpolarised signal from a magnetically focussed methane beam. A hyperpolarisation method which theoretically should allow the NMR detection of molecules at a scale equivalent to a single surface layer. While the overall measurements were unsuccessful, the technique is highlighted as a potential method for answering the currently outstanding question: “Is molecular hyperpolarisation preserved during adsorption to a cold surface?”

Declarations:

This work has not previously been accepted in substance for any degree and is not being concurrently submitted in candidature for any degree.

Signed: 

Date: 26/03/26

This thesis is the result of my own investigations, except where otherwise stated. Other sources are acknowledged by footnotes giving explicit references. A bibliography is appended.

Signed: 

Date: 26/03/26

I hereby give consent for my thesis, if accepted, to be available for electronic sharing

Signed: 

Date: 26/03/26

The University's ethical procedures have been followed and, where appropriate, that ethical approval has been granted.

Signed: 

Date: 26/03/26

Contents:

Abstract 2
Declarations 3
Acknowledgements / Funding 7
List of Figures 8
List of Tables 9
Chapter 1 : Introduction: 10
Section 1.1 Overview: 10
Section 1.2 : Nuclear Spin Isomerism: 10
Section 1.3 : Motivation for Studying Water NSC: 11
Section 1.4 : Introduction to NMR: Net Magnetisation and how to Measure it: 12
Nuclear Spin Magnetic Moment 13
Spin in a magnetic field: Origins of net magnetisation: 13
Measuring $\boldsymbol{M}$: 14
Equipment requirements for an NMR experiment: 16
Section 1.5 : NMR Signals, time constants and measurement types: 16
90° Pulses, tip angle tests and FID's: 16
Types of relaxation: 18
T_2*: 19
Spin echoes and measuring T_2: 19
T_1: Spoiler pulses and inversion recovery: 21
Chapter 2 : Measurements of Nuclear Spin Conversion in Water Isolated in an Argon Cryomatrix: 23
Section 2.1 Introduction: 23
Section 2.2 : Spin Isomerism in Water: 23
Section 2.3 Sample Preparation: 24
Section 2.4 Verification of Sample Concentration: 29
Impact of Nozzle Temperature: 29
Concentration testing with H_2O: 31
Concentration testing with D_2O: 33
Section 2.5 Sample Characterisation: 36
Presentation of an echo / T2*: 36
Measuring T_1: 37
Echo trains / T_2: 38
Section 2.6 Data Collection: 42

Measurement Method: 42
Pulse Sequence for NSC Measurements: 42
Section 2.7 Raw Data and Definition of Signal: 45
Section 2.8 Pre-Processing / Factors Impacting Signal Extraction: 47
Window Size, T_2* and Pulse artifacts: 47
Echo Shape: 48
Spiking / Coil arcing: 49
Conclusions from pre-processing: 51
Section 2.9 : Initial Analysis: 53
First Presentation of data: Cooling: 53
First presentation of data: Heating: 54
Signal Level Analysis: Introduction: 55
Signal Level Analysis: Cooling Data 56
Signal Level Analysis: Heating Data: 61
Signal Level Analysis: Conclusions: 63
Section 2.10 Fitting NSC Curves: 64
Overview: 64
Cooling Experiment Fitting: 64
First order fits: 64
Second order fits: 65
Fits to Experimental Data: 66
Heating Experiment Fitting: 68
Conclusions: 71
Section 2.11 : Next Steps: 73
Chapter 3 : Towards Hyperpolarised Deposition with Methane: 74
Section 3.1 : Hyperpolarisation: 74
Overview of hyperpolarisation methods: 74
Applicability to MIS NSC Measurements: 74
Magnetically focused polarised molecular beams: 75
Section 3.2 : Methane, Characteristics and comparison to water: 78
Molecular Structure and Rotational States: 78
Nuclear Spin Modifications, degeneracies and rotational populations: 79
Advantages of methane for hyperpolarised NMR measurements: 80
Section 3.3 : Apparatus Overview: 82
Section 3.4 : The Source: 83

Source Construction and Relevant Theory: 83
Source Optimisation: 84
Source Modelling: 84
Section 3.5 : The Hexapole: 86
Overview and Structure: 86
Working Principle: 87
Hexapole Modelling: 88
Section 3.6 : Beam Profiling: 90
Introduction and profiler construction: 90
Initial Profiling: 92
Second Profiling Run: 93
Estimation of Beam Flux and Final Polarisation: 100
Section 3.7 : The deposition target and NMR probe: 101
Section 3.8 : Designing HPD measurement Sequence: 103
Macroscopic Deposition Procedure: 103
Acquisition window size: T_2*: 104
Measurement repetition rate: Measuring T_1: 105
Measurement Repetition Rate: Modelling the Signal: 106
T2: 111
Chosen Hyperpolarised Measurement Structure: 112
Section 3.9 : Experimental Procedure and Results: 115
Results: 115
Discussion: 118
Chapter 4 : Summary and Outlook: 120
Section 4.1 : Overview: 120
Section 4.2 : Change of Sample: Hydrogen NSC 121
Section 4.3 : Modification of apparatus: Surface Coils: 122
Section 4.4 : Modification of the apparatus: Deposition System: 123
Section 4.5 : Reconstruction of apparatus: Combined NMR/IR 123
References: 126

Acknowledgments:

I would like to thank my supervisors Prof. Gil Alexandrowicz and Dr. Helen Chadwick for their academic guidance, continuous support and genuine human compassion throughout my PhD without which I would not be in the position to submit my PhD thesis.

I would like to thank my parents and family whose unconditional support and love has seen me through numerous hardships.

I would like to thank my housemate, Dale Hargrove, and fellow student Morgan Lowe for the companionship they have provided me over my time at Swansea.

And finally, I would like to thank all members of the Swansea Surface Dynamics research group, past and current, for the fascinating work they have and continue to do and exciting research environment said work provides.

Funding:

The research work presented in this thesis was funded by an ERC consolidator grant: Horizon 2020 Research and Innovation Programme grant 772228.

List of figures (Descriptions Abbreviated):

Figure 1.5.1: Simple schematic of a one-pulse NMR experiment structure. 17
Figure 1.5.2: An example experimental FID 18
Figure 1.5.3: Schematic of a basic echo measurement. 20
Figure 1.5.4: Example single echo measurement from a CH_4@Ar sample 20
Figure 1.5.5: Schematic of an echo train measurement. 21
Figure 1.5.6: Schematic of a T1 measurement sequence. 22
Figure 2.2.1: Simple schematic of Water. 24
Figure 2.3.1: Diagrammatic representation of set up for a H_2O@Ar experiment. 25
Figure 2.3.2: Diagram of the gas handling system. 26
Figure 2.3.3: Photographs of sapphire pre and post deposition. 27
Figure 2.3.4: Nozzle-retracted image of sample in previous figure. 28
Figure 2.4.1: Photograph and schematic of the nozzle and thermocouple. 29
Figure 2.4.2: Mass spectrometer counts during H_2O@Ar exposure. 32
Figure 2.4.3: Mass spectrometer counts during D_2O@Ar exposure. 34
Figure 2.5.1: Average NMR signal from a 1% H_2O@Ar sample. 37
Figure 2.5.2: T1 measurement on the same sample shown in Figure 2.5.1. 37
Figure 2.5.3: T2 measurement for the sample shown Figure 2.5.1. 39
Figure 2.5.4: NMR signal produced by a CPMG echo train sequence. 40
Figure 2.6.1: Pulse sequence used for water NSC data collection. 43
Figure 2.7.1: First 10 echoes of an echo train taken after temperature decrease 45
Figure 2.7.2: Figures showing variance in echo shape within a train. 46
Figure 2.8.1: Figures showing impact of masking on averaged echoes. 47
Figure 2.8.2: Comparisons of first and 5^{th} echoes in a train. 48
Figure 2.8.3: Example average train with arc induced spiking. 50
Figure 2.8.4: Comparisons of averaged trains with and without filtering 51
Figure 2.9.1: Exaple result of a "cooling" temperature jump measurement. 53
Figure 2.9.2: Exaple result of a "heating" temperature jump measurement. 54
Figure 2.9.3: Normalised data from all 20 to 6K temperature jump experiments. 56
Figure 2.9.4: Fitting final signal level to cooling data. 57
Figure 2.9.5: Map of temperature space pairs required to explain previous figure. 58
Figure 2.9.6: Fitting initial signal level for heating data. 62
Figure 2.9.7: Fitting final signal level for heating data. 62
Figure 2.10.1: Fitting of NSC for cooling data alongside residuals. 66
Figure 2.10.2: Linearised plots for fits in previous figure. 67
Figure 2.10.3: Fitting of NSC for heating data alongside residuals. 70
Figure 2.10.4: Linearised plots for first fit in previous figure. 70
Figure 3.2.1: Schematic representation of Methane. 78
Figure 3.3.1: Schematic of the experimental apparatus. 82
Figure 3.4.1: Subsection of Figure 3.3.1 regarding source region. 83
Figure 3.5.1: Subsection of Figure 3.3.1 regarding the hexapole lens. 86
Figure 3.5.2: Photographs of lens elements. 86
Figure 3.5.3: Perpendicular Slices through model methane beams. 89
Figure 3.6.1: Subsection of Figure 3.3.1 regarding profiling region. 90
Figure 3.6.2: Design schematics for the profiling flags. 91
Figure 3.6.3: Single Flag profiling scans. 92

Figure 3.6.4: Dual flag scans and fits. 94
Figure 3.6.5: Heatmap of RMSR values between model / experimental profiles 97
Figure 3.6.6: Heatmap of proton polarisation arriving at the deposition surface. 99
Figure 3.7.1: Images of deposition surface mount. 101
Figure 3.7.2: Photograph of nozzle-coil assembly with circuit diagram. 102
Figure 3.7.3: Images of the deposition surface illuminated by the laser. 102
Figure 3.8.1: Diagram of the gas handling system for methane depositions. 104
Figure 3.8.2: Example $T2^*$ fit for a ~6% CH_4@Ar sample. 105
Figure 3.8.3: Example of a T1 measurement on a ~6% CH_4@Ar sample. 106
Figure 3.8.4: Plot of number of hyperpolarised spins $\mathrm{N}\downarrow$ vs deposition time. 108
Figure 3.8.5: Model single echo SNR vs measurement number. 110
Figure 3.8.6: Example T_2 measurement on a ~6% CH_4@Ar sample. 111
Figure 3.8.7: Example methane echo train measurement showing T_2 extension. 112
Figure 3.8.8: Diagram of pulse sequence for methane experiments. 113
Figure 3.8.9: Model train averaged SNR vs measurement number 114
Figure 3.9.1: Example signals from a HPD experiment. 116
Figure 3.9.2: FT of signals for regions with/out the methane beam. 117

List of tables (Descriptions Abbreviated):

Table 1.2.1: Table of the nuclear spin wavefunctions of ordinary dihydrogen. 11
Table 2.9.1: Values of F for the three cooling experiments 61
Table 2.9.2: Values of F for the three heating experiments shown in Figure 2.9.7 63
Table 2.10.1: Extracted first order rate constants for NSC curves captured at 20K 71
Table 2.10.2: Average first and second order rate constants from NSC curves. 71
Table 3.2.1: Numbers of degenerate states for methane at varying *J*. 79

Chapter 1: Introduction:

Section 1.1 Overview:

The experiments described in this thesis are efforts to further the application of matrix isolation spectroscopy (MIS) in the understanding and measurement of nuclear spin conversion (NSC) in water, and in the measurement of hyperpolarised spin in methane. Historical MIS work regarding NSC has largely been conducted using Fourier-Transform-Infrared-Spectroscopy (FTIR), which takes advantage of the coupling between nuclear spin and molecular rotational states to track NSC by observing changes in the intensity of a samples various ro-vibrational peaks. This typically requires an infrared source, and in cases where the light must pass through the sample to reach a reflective surface, samples with favourable optical qualities.

This work compliments FTIR studies by performing nuclear magnetic resonance (NMR) experiments on molecules trapped within isolation matrices. NMR works by manipulating and measuring nuclear spin directly. Employed on a wide scale for applications from studying molecular motion[1] to medical imaging[2-4], NMR is widely regarded as a gentle spectroscopic method which has little perturbing effect on the sample under study (due to the low energy required to change the projection state of individual spins). The largest obstacle in the study of NSC with NMR is low signal to noise ratio. While FTIR can detect concentrations of molecules as low as 0.2% in mm scale samples[5, 6], NMR typically has much lower sensitivity, mostly due to thermodynamical constraints in creating population differences (see Section 1.4). Chapter 2 of this work demonstrates that while this low sensitivity presents difficulties it does not preclude measurement entirely, while Chapter 3 discusses a potential method by which samples typically too dilute to be studied with conventional NMR methods may be made measurable.

The remainder of this first chapter is given over to introducing the basic concepts used and discussed in later chapters. Starting with an introduction to nuclear spin isomerism.

Section 1.2: Nuclear Spin Isomerism:

NSC is the process of conversion of a molecule from one total nuclear spin state to another. Molecules of the same species but in differing total spin states may be referred to as nuclear spin-isomers (NSI's) or nuclear spin modifications (NSM's). There are relations between the total nuclear spin state of a molecule, and the rotational energy states it can occupy, as a result different NSI's can have significantly different rotational energies. The distribution of isomers amongst these energies depends on the total molecular wavefunction, spin statistics and symmetry rules.

The textbook[7] example of a molecule which exhibits nuclear spin isomerism is ordinary dihydrogen $^1H_2$. The molecule has two spin-half nuclei and therefore may occupy total nuclear spin states of $I = 0$ or $I = 1$. The overall state of the hydrogen molecule is described by its total molecular wavefunction (φ_{tot}). This may be expressed as a product of individual wavefunctions, overall taking a form akin to:

$$\varphi_{tot} = \varphi_{trans}\,\varphi_{vib}\,\varphi_{rot}\,\varphi_{spin}\,\varphi_{elec} \quad \text{(Eq. 1.2.1)}$$

Where the terms on the right-hand side represent the translational, vibrational, rotational, nuclear spin and electronic wavefunctions respectively. The nuclei of both atoms comprising the molecule are spin-half and therefore fermions. The Pauli-exclusion principle therefore requires that the total molecular wavefunction be antisymmetric (must change sign) under exchange of the two protons.

In the ground vibrational and electronic states φ_{trans}, φ_{vib} and φ_{elec} are symmetric under particle exchange. For φ_{tot} to be antisymmetric the product $\varphi_{rot}\varphi_{spin}$ must therefore be antisymmetric. Labelling the nuclei in the molecule A and B, and denoting spin up as α and down as β, the four possible expressions for φ_{spin} separated by total nuclear spin (I) value are:

Table 1.2.1: Table of the nuclear spin wavefunctions of ordinary dihydrogen ($^1H_2$), divided by total nuclear spin value. There are three functions leading to I=1, while only a single solution exists for I=0.

$I = 0$	$I = 1$
$\varphi_{spin} = \alpha(A)\beta(B) - \alpha(B)\beta(A)$	$\varphi_{spin} = \alpha(A)\alpha(B)$
	$\varphi_{spin} = \alpha(A)\beta(B) + \alpha(B)\beta(A)$
	$\varphi_{spin} = \beta(A)\beta(B)$

Exchanging the positions of A and B within the functions displayed in Table 1.2.1 reveals that only the function associated with $I = 0$ exhibits a change of sign (is antisymmetric). For $\varphi_{rot}\varphi_{spin}$ to be antisymmetric overall, φ_{rot} must be symmetric when $I = 0$ and antisymmetric when $I = 1$. As a homonuclear diatomic molecule, the symmetry of φ_{rot} for $^1H_2$ changes as a function of the rotational quantum number J, states with even J have symmetric φ_{rot}, while states with odd J have antisymmetric φ_{rot}.

The overall result is a partitioning of the nuclear spin isomers (referred to as para and ortho hydrogen for $I = 0$ and $I = 1$ respectively) between the even and odd rotational states of hydrogen. This partitioning is a boon for FTIR methods of measuring NSC, as it allows different rotational peaks in the spectra to be assigned a nuclear spin state without directly measuring the spins themselves. For NMR it is less relevant, as only the $I = 1$ state is NMR active. The partitioning of nuclear spin isomers across rotational energy levels for the molecules under study in this work (water and methane) are covered in Section 2.2 and Section 3.2 respectively.

Section 1.3: Motivation for Studying Water NSC:

The study of nuclear spin conversion is an active field with a wide variety of chemical species under investigation[8]. A molecule of particular interest is water[9], much like hydrogen water has two spin isomers (see Section 2.2), also termed para and ortho. The rate of conversion in this species is noted to be slow, slow enough that spectroscopic observation of the ortho-to-para ratio of water in the interstellar medium (ISM) is earmarked[10] as a potential “molecular clock” which can be used to date the formation of ices and other solids making up the ISM.

MIS studies of water in various rare gas matrices using FTIR has already been the subject of at least one thesis[5], with recent NMR studies of water NSC being confined to water isolated in C_{60} (Buckminster fullerene)[11, 12]. In both cases, isolation is presented as a way of constraining the water molecules for measurement while preserving the characteristic free-rotation of the gas phase water molecule (and therefore preserving its gas-phase energy level structure). In reality a better term would be “nearly” free rotation, with recent spectroscopic work[13] for water in an argon matrix in particular describing the energy level via a “confined asymmetric rotor model”. Water is abundant, easy to source in very high purity and safe to work with. Of its two spin isomers only one is NMR active, allowing for measurement of NSC simply by observing the change in signal level over time[11].

In the FTIR work[5], abrupt temperature changes on the order of 10s of kelvin were demonstrated to be sufficient to induce measurable changes in the spin-isomer population of water in argon (H_2O@Ar) samples, providing a framework for NSC measurements with NMR and also giving grounds for direct comparison.

For these reasons, water in argon was chosen as the initial test system for NMR MIS measurements of NSC, the focus of Chapter 2. There is also existent literature concerning the study of NSC in CH_4 and CH_4@Ar specifically though the complexity of the rotational partitioning of the CH_4 nuclear spin modifications (NSM’s) render it a poor candidate for initial studies. The benefits of CH_4 as a test molecule as well as the distribution of its three NSM’s is the subject of Section 3.2.

Section 1.4: Introduction to NMR: Net Magnetisation and how to Measure it:

NMR is a spectroscopic technique which observes changes in the populations of nuclear spin projection states within a magnetic field, via the emission and absorption of radio-frequency electromagnetic radiation. A complete understanding of the NMR behaviour of a molecule is dependent on quantum mechanics, the mathematics of which is a subject best left to the authoritative texts[14, 15] in the field. While the work presented here does rely on understanding basic NMR characteristics of the samples under study for the purposes of constructing suitable measurements, complete analysis of the underlying spin dynamics of the measured signals is considered out of scope. In both systems, only the overall NMR signal level and how it changes as a function of time is investigated.

For this reason, the description of NMR presented here is limited to the so called “vector model”, a classical model which accurately describes the macroscopic NMR behaviour of the system, neglecting the finer details. Further to this, while the molecules under study are inherently spin > 1/2, for the purposes of estimating average polarisation they are considered to behave as an ensemble of spin-half protons (an assumption which is largely found to hold true[14]). The sources of nuclear spin in both systems are hydrogen atoms, so it makes sense to frame the discussion in terms of proton spin.

Nuclear Spin Magnetic Moment

The nucleus of a ^{1}H atom is comprised of a single proton with total spin ½. This spin is the quantised analogue to classical rotational angular momentum. As the proton is a charged particle, from classical physics it is expected that the rotation of a charged particle will produce an electromagnetic field. This is also the case for the "spinning" proton, the magnetic moment arising from said proton being[14-16]:

$$\boldsymbol{\mu} = \gamma \hat{\boldsymbol{s}} \qquad \text{(Eq. 1.4.1)}$$

Where $\hat{\boldsymbol{s}}$ is the total nuclear spin operator and γ the gyromagnetic ratio. For nucleons γ itself may be further broken down to:

$$\gamma = g\frac{\mu_N}{\hbar} \qquad \text{(Eq. 1.4.2)}$$

Where μ_N is the nuclear magneton, $\hbar$ the reduced planck constant and g is the spin g-factor, a dimensionless quantity which directly relates the nucleons magnetic moment to its spin angular momentum. The sign of γ is important, as it determines whether the magnetic moment aligns parallel or anti-parallel to the protons spin angular momentum. In hydrogen γ is positive, so the two are aligned parallel.

Assigning the quantisation axis for the nuclear spin as parallel to the cartesian $\hat{\boldsymbol{z}}$ the magnetic moment of a given spinor along said axis may be given in terms of the magnetic quantum number m_i:

$$\boldsymbol{\mu_z} = \gamma m_i \hat{\boldsymbol{z}} \qquad \text{(Eq. 1.4.3)}$$

For a proton this may take one of two values ($\pm\frac{1}{2}\hbar\gamma$) corresponding to the two possible values of m_i ($\pm\frac{1}{2}\hbar$).

Spin in a magnetic field: Origins of net magnetisation:

From classical electrostatics[14-16], a magnetic moment at rest in a homogeneous magnetic field will have some magnetic potential energy:

$$E = -\boldsymbol{\mu}\cdot\boldsymbol{B} \qquad \text{(Eq. 1.4.4)}$$

Where $\boldsymbol{B}$ is a vector describing the orientation and strength of the magnetic field. If this field is defined as $\boldsymbol{B} = B_z\hat{\boldsymbol{z}}$ then in combination with (Eq. 1.4.3), for a proton we have two possible energy levels $E = \mp\frac{1}{2}\hbar\gamma B_z$. These energy levels again correspond to the two possible values of m_i, protons in the positive m_i quantum state have a negative energy which decreases linearly as the field strength increases, the inverse being true for protons in a the negative m_i quantum state.

When considering a group of protons (such as would be seen in a sample with many proton bearing molecules) the energy of each proton will vary due to the magnetic interaction of surrounding spins. Making the assumption that this perturbation of the energy is negligible (the energy arising from the static field being orders of magnitude larger than that arising from nearby spins) the probability of any single proton in the field having a specific energy and therefore a specific orientation is given by a Boltzmann distribution. Using ↑ to indicate protons with positive m_i, and ↓

those with negative, the probabilities of a proton being in either state may be defined as:

$$P(\uparrow) = \frac{\exp\left(\frac{\hbar\gamma B_z}{2k_bT}\right)}{\exp\left(\frac{\hbar\gamma B_z}{2k_bT}\right)+\exp\left(-\frac{\hbar\gamma B_z}{2k_bT}\right)} \quad \text{(Eq. 1.4.5)}$$

$$P(\downarrow) = \frac{\exp\left(-\frac{\hbar\gamma B_z}{2k_bT}\right)}{\exp\left(\frac{\hbar\gamma B_z}{2k_bT}\right)+\exp\left(-\frac{\hbar\gamma B_z}{2k_bT}\right)} \quad \text{(Eq. 1.4.6)}$$

Where k_b is Boltzmann's constant and T is the spin temperature. At thermal equilibrium T is the temperature of the sample. The denominator of both probabilities is equivalent, so understanding the differences between the two requires only consideration of the numerator. The difference in sign in the exponent implies that $P(\uparrow) > P(\downarrow)$, this is expected, as $\downarrow$ is the higher energy state and should be less populated. Further insight can be gained by considering the limits of T and B_z. As $T \longrightarrow \infty$ and $B_z \longrightarrow 0$ both numerators approach a value of 1. This indicates that at high temperature, or zero field, both states are equally populated. Conversely as $T \longrightarrow 0$ and $B_z \longrightarrow \infty$, $P(\uparrow)$ is maximised and $P(\downarrow)$ is minimised.

The overall conclusions are thus: in general, $P(\uparrow) > P(\downarrow)$, with the disparity being maximised at low temperature and high field. This disparity leads to there being slightly more proton magnetic moments aligning with the field than against it. The total magnetic moment of the sample must therefore be non-zero, as there are not enough antiparallel aligned moments to negate the effect of all of the parallel aligned ones. The overall polarisation of the sample is given by the relation:

$$Polarisation = \frac{P(\uparrow) - P(\downarrow)}{P(\uparrow) + P(\downarrow)} \quad \text{(Eq. 1.4.7)}$$

The net magnetisation $\boldsymbol{M}$ of the sample may then be defined as the product of the polarisation, the number of protons in the sample and $\boldsymbol{\mu_z}$. The small magnitude of $\boldsymbol{\mu_z}$ (approx. $2.793\mu_N$ for a single proton) is what leads to the low sensitivity of NMR measurements. The small magnetic moment implies very small energy differences between m_i states, and so small values of (Eq. 1.4.7), requiring either very low temperatures, very high fields or very large samples to achieve measurable values of $\boldsymbol{M}$. It is for this reason that the development of hyperpolarisation methods (i.e. methods of generating polarisation values greater than those achieved at thermal equilibrium) are a subject of active research (see Chapter 3).

Measuring $\boldsymbol{M}$:

Direct measurement of $\boldsymbol{M}$ while it lies parallel with the field responsible for creating it ($\boldsymbol{B}$) is possible but requires the use of exceptionally sensitive magnetometers referred to as Superconducting Quantum Interference Devices or SQUID's[17-19]. Historically, and in this work, measuring the net magnetisation of proton containing samples in a magnetic field has been achieved by first rotating $\boldsymbol{M}$ such that it is perpendicular to $\boldsymbol{B}$, the method by which this is achieved also providing a method by which to measure $\boldsymbol{M}$ directly.

Again, from classical electrostatics[14-16], it can be shown that a magnetic moment within a magnetic field will experience a torque $\boldsymbol{\Gamma}$:

$$\boldsymbol{\Gamma} = \boldsymbol{\mu} \times \mathbf{B} \qquad \text{(Eq. 1.4.8)}$$

Provided the external magnetic field is constant in time, the solution to (Eq. 1.4.8) is precession of the moment $\boldsymbol{\mu}$ about an axis parallel to said field. The frequency of this precession is the Larmor frequency ω_L defined as:

$$\omega_L = \gamma |\boldsymbol{B}| \qquad \text{(Eq. 1.4.9)}$$

$\boldsymbol{M}$ is simply a vector sum of all $\boldsymbol{\mu}$ for all protons in the system, provided any changes to the orientation of $\boldsymbol{\mu}$ are applied evenly across all protons then the overall effect will be an equivalent change in orientation of $\mathbf{M}$.

In the initial thermal equilibrium $\mathbf{M}$ is aligned with $\mathbf{B}$. The angle between each is 0 and the torque on $\mathbf{M}$ is zero. The precession of $\mathbf{M}$ about **B** presents an opportunity for measurement, as, in the case that $\mathbf{M}$ may be induced to precess such that its orientation changes as a function of time, it would create an oscillating magnetic field. Such a field would inherently induce an electric field in any nearby conductor, this induced field is the observable in an NMR measurement. To achieve this $\mathbf{M}$ must be rotated to some angle from $\boldsymbol{B}$**,** ideally 90° as this is where the oscillation would be greatest.

One method to achieve this is the introduction of a pulsed rotating magnetic field termed $\boldsymbol{B_{rot}}$, which is perpendicular to the static field $\boldsymbol{B}$ and which rotates at the Larmor frequency ω_L. The impact of the pulsed field is most conveniently understood within a rotating frame of reference. If said frame rotates in the same plane as $\boldsymbol{B_{rot}}$ and at the same frequency ω_L, then $\boldsymbol{B_{rot}}$ will appear as if it were a static field for the duration of the pulse. Similarly, the precession of $\mathbf{M}$ about the static field $\boldsymbol{B}$ is imperceptible as it also occurs at a frequency of ω_L, removing the effect of $\boldsymbol{B}$ from the analysis. The problem then reduces to the behaviour of a magnetic moment within a static field, $\mathbf{M}$ precesses about the axis parallel to $\boldsymbol{B_{rot}}$ for the duration the field is switched on, once the field is switched off the accumulated precession angle θ is:

$$\theta = \gamma B_{rot} t \qquad \text{(Eq. 1.4.10)}$$

Where B_{rot} is the magnitude of B_{rot} and t the duration of the pulse. While NMR setups capable of generating rotating fields do exist[20] in practice linearly oscillating fields are sufficient to induce precession. This being because a linearly oscillating field can be shown[14, 15] to be a product of two counterrotating fields, one of which is $\boldsymbol{B_{rot}}$, while the other has the same absolute magnitude but rotates at -ω_L. In the rotating frame this field appears to rotate at $-2\omega_L$, for NMR experiments in the MHz range, this averages out to have almost zero impact on the orientation of $\mathbf{M}$. The field can therefore be supplied by a simple tuned coil (at its simplest, a single loop of wire) placed at an angle to the fixed field **B** (ideally 90°) and supplied with alternating current at frequency ω_L. The strength of the field is dictated by the coil voltage, with the final angle being dictated by this and the pulse duration in line with (Eq. 1.4.10).

The same coil which is used to rotate **M** may then (with sufficient amplification and noise cancellation) be used to measure the voltage induced as **M** precesses about **B**, after the pulse is turned off. For the remainder of this work, the component of the linear field rotating at ω_L will be referred to as $\mathbf{B_1}$, while the static field will be $\mathbf{B_0}$ in line with standard notation in NMR textbooks[14, 15].

Equipment requirements for an NMR experiment:
In its simplest form an NMR experiment requires three things: A sample to be studied, a magnet to produce $\mathbf{B_0}$ and a coil capable of transmitting and receiving electromagnetic radiation at a frequency corresponding to the nuclei under study and the strength of the magnetic field.

The samples used in this work are discussed in their relevant chapters. The magnet used is a superconducting solenoidal magnet operated in the region of 5-6 Tesla. The coils used to produce $\mathbf{B_1}$ varied throughout experimentation as various challenges with the measurements were addressed. In all cases the coils were simple two or three turn wire loops, hand assembled from vacuum compatible 1mm diameter oxygen free copper wire. For H_2O@Ar measurements these were attached directly to the end of the cold finger (custom designed by ColdEdge for use with their Stinger™ cooling system) used to mount the deposition surface for the vacuum deposited H_2O@Ar samples. For CH_4@Ar the coil was mounted separately to a support within the bore of the magnet, brought into proximity with the deposition surface. Brief overviews of both setups may be found in Section 2.3 and Section 3.7 respectively.

NMR measurements schemes, pulse programming, delivery and recording of resultant signals were performed using a Redstone Tecmag commercial pulse programmer and RF amplifier, in concert with the Tecmag TNMR software. An overview of basic measurement structures is provided in the next section.

Section 1.5: NMR Signals, time constants and measurement types:

In the ideal case, an ensemble of spins which do not interact with each other or their environment, positioned in a homogeneous static magnetic field ($\mathbf{B_0}$) and briefly exposed to a rotating field perpendicular to the static field ($\mathbf{B_1}$) would precess about the static field with some fixed angle, forever. The resultant signal observed in the form of an induced voltage would be a sine wave with a frequency equal to ω_L, persisting into eternity.

In reality, interactions between the spins and their environment are not completely negligible and $\mathbf{B_0}$ not completely homogeneous, as a result the sine wave is observed to decay with time. After sufficient time, the spins in a sample eventually return to their thermal equilibrium alignments with the static magnetic field. The decaying oscillating signal observed following a $\mathbf{B_1}$ pulse is referred to as a free induction decay (FID), the generation and study of which is the simplest form of pulsed NMR experiment.

90° Pulses, tip angle tests and FID's:
The maximum possible observable signal in an NMR experiment is achieved when **M** lies at 90 degrees to the static field. A pulse of sufficient strength and length to

achieve this rotation is referred to as a 90° or $\frac{\pi}{2}$ pulse. In an ideal system where all variables were known the setting for this pulse could be deduced analytically. In reality it is typically identified through a tip angle measurement. In such a test either the pulse duration or amplitude (voltage) is fixed, and the other variable varied. The resultant signals are observed, and the settings which produce an FID with the greatest initial magnitude are chosen as the 90° settings. The programming of a single pulse measurement would look something like:

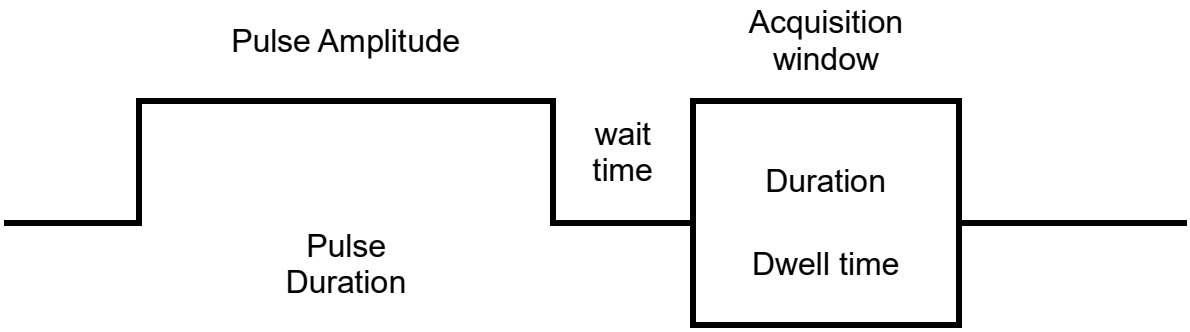

Figure 1.5.1: Simple schematic of a one-pulse NMR experiment structure.

Flat regions in the program indicate no transmission or reception. Raised bumps indicate transmission of pulses, while closed boxes indicate regions where the induced voltage in the coil is measured. Pulse duration and amplitude have been previously discussed. The “wait time” is a period before opening the receiver, this is introduced to avoid exposing the receiver to the electrical noise which follows the high-voltage transmission of the pulse. The dwell time is how long the analogue to digital converter averages per data point, while the duration is the total time the receiver listens for signal.

This signal is analogue and continuous, observed directly on an analogue oscilloscope it would appear as a decaying high frequency sine wave with amplitude representing the induced voltage in the coil. To allow for more detailed analysis the signal is put through a mixer, and the central frequency (nominally the Larmor frequency) is subtracted. The signal is then amplified and converted from analogue-to-digital within the Redstone box. The previously mentioned mixing of the signal is performed twice, creating two central frequency oscillations which are phase shifted with respect to each other by 90 degrees. One of these components is designated are real, the other imaginary, overall being equivalent to a signal captured in quadrature with receiver coils aligned to detect along the x and y axis in the plane of the real coil. The software allows for the phase of both transmission and reception to be programmed. The phase of the sing in an NMR experiment depends on both the details of the pulse sequence as well as the specifics of the physical circuitry, in general the experimental signal will be split between both the real and imaginary components. To assess the overall intensity of the signal it is necessary to consider the complex magnitude of the two components, or to subject the results to 0^{th} order phase correction (multiplying through by $e^{i\theta}$ where θ is the phase mismatch) which forces the signal to appear completely real (or imaginary).

As a final note, the TNMR software performs some initial post processing of the digitised NMR signal, subtracting the resonant frequency (ω_L) so that the final signal

is a smooth decay rather than a decaying sine wave. A typical fid is shown in Figure 1.5.2. (overleaf).

The 90° excitation pulse provided by the spectrometer has a programmable phase, being equivalent to providing a rotating field about x, y, -x or -y. The resultant FID is therefore expected to have the entirety of its signal in the corresponding receiver phase (only showing up in one component). The fact that both the real and imaginary components in Figure 1.5.2 shows that the phase of the receiver and the excitation pulse do not always perfectly align, despite being programmed to. The magnitude of the FID can be seen to decay as acquisition time increases, with the exception of the first point. The low signal in the initial datapoint is attributed to interference from or saturation of the receiver due to the excitation pulse. This highlights an issue with FID's, the maximum signal is observed immediately following the excitation pulse, but the high voltages such pulses require often lead to residual coil noise (called ringing) and result in artifact in the final signal. The wait time introduced in Figure 1.5.1 is introduced to address this, but optimising this to both minimise exposure to ringing while not also losing the start of the measurement (which due to the decay contains the highest signal) is difficult.

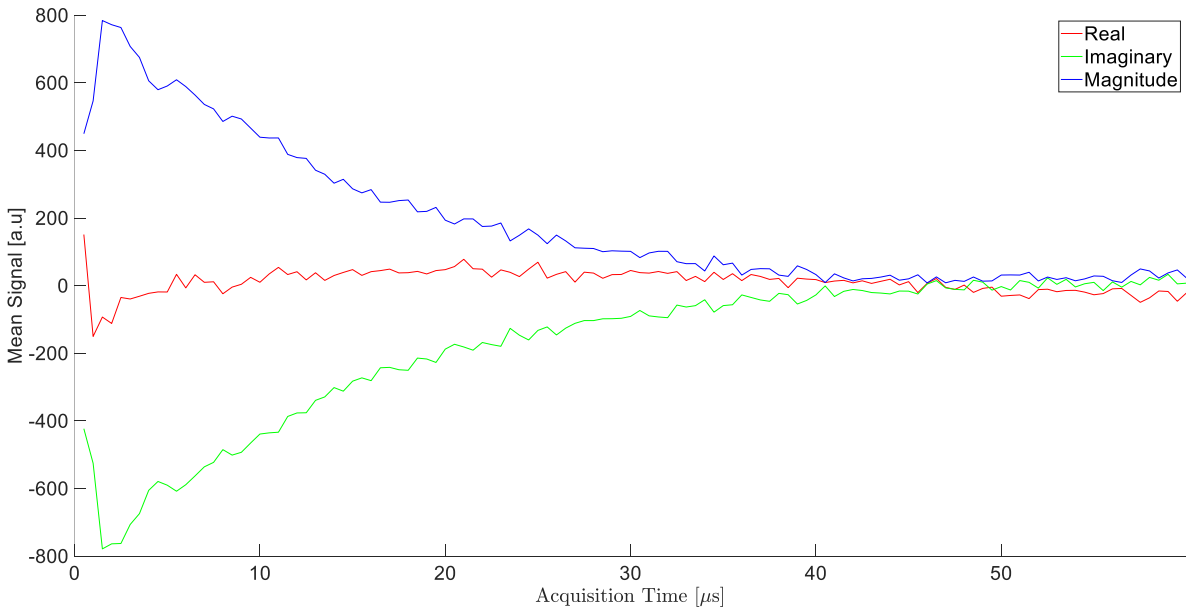

Figure 1.5.2: An example experimental FID, captured from a 6%CH_4@Ar sample. The majority of the signal is seen to be in the imaginary components; the total acquisition window was 100μs but has been trimmed as the signal fell to ~0 well before that. The dwell time for this measurement was 500ns. Some distortion owing to residual interference or saturation from the excitation pulse is noted in the first data point.

The decay of the FID is indicative of a loss of magnetisation in the transverse (xy) plane and is customarily modelled using an exponential decay with a time constant termed $T2^*$.

<u>Types of relaxation:</u>

In real systems, regardless of the degree of perturbation, the spins in a system will eventually return to their thermal equilibrium distribution of orientations. Complete relaxation to this state is referred to as longitudinal relaxation, the time constant describing this process is the longitudinal relaxation time constant T_1. T_1 is often

referred to as the spin-lattice time constant, as it is assumed the energy imparted to perturb the spins is eventually lost to the surroundings or "lattice". However, most samples will typically exhibit FID decay which is faster than T1. This is because there are other ways the magnitude of the net magnetisation in the xy plane can be reduced without the returning to thermal equilibrium. Relaxation of this form is referred to as transverse relaxation, representing any process which reduces the net magnetisation in the xy plane.

Two time constants are used to describe transverse relaxation T_2 which accounts only for processes that are irreversible in time, and T_2^* which accounts for T_2 processes as well as reversible (discussed later in this section) decay owing to inhomogeneities in the magnetic field. As a general rule $T_1 \geq T_2 \geq T_2^*$.

<u>T_2*:</u>
T_2* contains contributions from all possible decay processes and therefore is the shortest time constant. To a first approximation it may be measured by fitting the free induction decay to a simple exponential of the form:

$$S(t) = Aexp\left(-\frac{t}{T_2^*}\right) \quad \text{(Eq. 1.5.1)}$$

Where S is the signal magnitude and A the maximum observed signal at $t = 0$. In the quantum mechanical description[14] both transverse relaxation constants are related to the decoherence of the ensemble of spins. The reversible effects attributed to T_2^* are usually associated with inhomogeneities in the static magnetic field. The protons in the sample are dispersed across a region in space, the local differences in the field strength perceived by said protons lead to each experiencing differing values of ω_L. While immediately following the pulse the spins are all aligned, the difference in ω_L leads the spins to dephase over time, reducing the magnitude of the net magnetisation.

While this is initially concerning it does provide an interesting proposition, what if it were possible to cause the spins to come back into phase with each other.

<u>Spin echoes and measuring T_2:</u>
If $T_2^* < T_2$ it is possible to construct a measurement that causes the transverse magnetisation to re-emerge after it would normally have been lost. The dephasing of spins due to field inhomogeneity arises from spins in weaker local fields "lagging behind" in their rate of precession, while those in stronger fields "pull ahead". If their relative positions in the xy plane could be swapped, the faster spins would be put behind, while the slower spins are put ahead. Eventually the two would meet in the middle and the transverse magnetisation would be regenerated.

By providing a pulse sufficient to rotate the spins 180° it is possible to achieve such a regeneration. The signals generated from these measurements are termed spin echoes, first described by Hahn in 1950[21]. While the original Hahn echo was a so called "solid echo" using two 90 degree pulses, modern Hahn echo sequences typically use a 90-180 pulse pairing[22]. An example measurement structure used to measure a single spin echo is given in Figure 1.5.3. From (Eq. 1.4.10) it can be seen that a 180° pulse can be attained by doubling either the field strength or

duration of a 90° pulse. The time between pulses (τ_1 in Figure 1.5.3) dictates where the echo will appear, the maximum in the echo lying τ_1 seconds from the end of the 180° pulse.

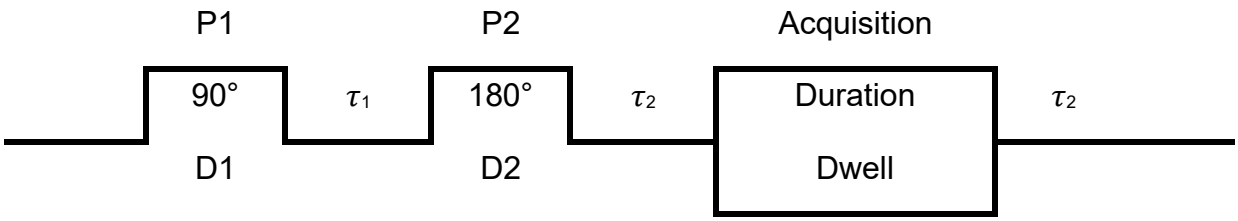

Figure 1.5.3: Schematic of a basic echo measurement. P1 and P2 are pulse powers, D1 and D2 are pulse durations. These are chosen such that the first pulse is a 90° pulse, and second a 180°. In practice, echoes can be generated using less ideal tip angles, but the 90-180 pulse combo produces the sharpest echo. τ_1 is the interpulse, while τ_2 is chosen such that the maximum of the echo is (ideally) centred within the acquisition window.

An example experimental echo, again from a CH_4@Ar is shown in Figure 1.5.4.

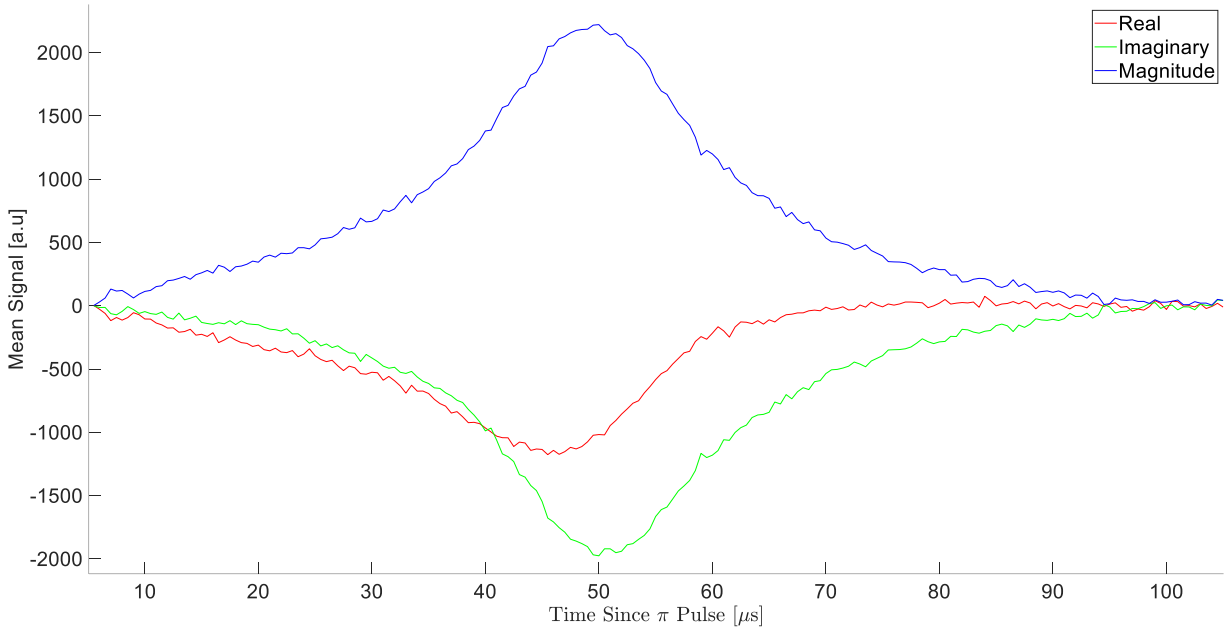

Figure 1.5.4: Example single echo measurement from a CH_4@Ar sample. The interpulse spacing for this measurement was 50μs, leading to a maximum in the echo 50μs after the end of the 180° pulse. The signal is again seen to be slightly out of phase.

An ideal spin echo signal would be a back to back FID, growing then decaying at a rate described by T_2^*. This implies that T_2^* may also be extracted from and echo signal and indeed can be by taking the full width half maximum of the echo Fourier transform and converting to time. Because the echo must inherently have its maximum displaced from the end of refocussing 180° pulse, rather than immediately following excitation (as in the case of an FID) it is often preferable to measure T_2^* by this method, as it is less sensitive to artifacts caused by coil ringing. Where possible this is the chosen method for measuring T_2^* in this work.

The echo measurement is only able to refocus transverse magnetisation lost to reversible processes. The maximum amplitude of the echo is expected to be less than the maximum amplitude of an FID measured immediately after a 90° pulse, and to decay more as τ_1 increases. This decay is governed by T_2, allowing T_2 to be

measured (again to a first approximation) by taking echo measurements at varying τ_1 and fitting the decay in echo height to:

$$S(t) = Aexp\left(-\frac{t}{T_2}\right) \quad \text{(Eq. 1.5.2)}$$

Where t is the time between the first perturbation of the spins (the 90 degree pulse) and the peak of the echo. In the case that T_2 is sufficiently larger than T_2^* it is possible to generate further echoes by providing further 180 pulses. Measurements of this type are called echo-train measurements, with a wide variety of pulse structures being developed. Echo-train measurements used in this work are of the Carr-Peurcell-Meighboom-Gill (CPMG) type, an example pulse sequence structure for this is given in Figure 1.5.5.

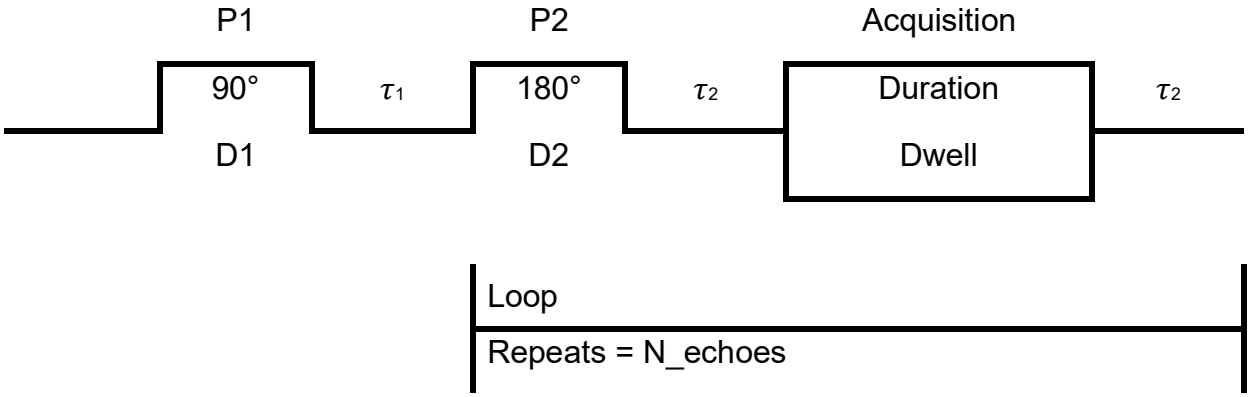

Figure 1.5.5: Schematic of an echo train measurement. The measurement can be seen to be identical to the single echo measurement presented in Figure 1.5.4 with the addition of a loop over the 180° pulse, τ_2 waits and acquisition window. The number of loops determines the number of times an echo is generated, provided T_2 is sufficiently long.

A common application of the CPMG train is in direct measurement of T_2, as the resultant signal is expected to be a series of echoes exhibiting T_2 decay. The samples studied in this work were unusual, in that (for values of τ_1 on the order of 50μs) the produced echo trains did not exhibit T_2 like decay, examples and brief discussion are left to the relevant sections (Section 2.5 & Section 3.8).

<u>T_1: Spoiler pulses and inversion recovery:</u>
The longitudinal relaxation time constant or T_1 describes the rate at which the spins within the sample return to thermal equilibrium. There are multiple ways to measure T_1, the method used in this work is reliant on what is referred to as a spoiler pulse train or sometimes a “saturation comb”.

A spoiler pulse train is a series of very short, rapidly interspersed pulses designed to randomise the spin-orientation of the protons in the sample. The overall result is a reduction of the net magnetisation to zero. As is the case for inversion recovery, the system is allowed to relax for some time (T_{rec}) before being subjected to a measurement sequence. The sequence typically used for T1 measurements in this work took the form:

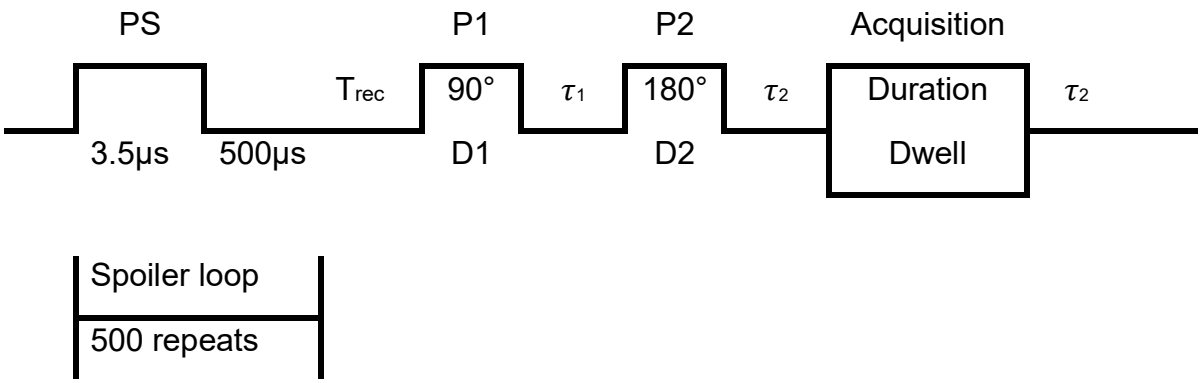

Figure 1.5.6: Schematic of a T1 measurement sequence. PS is the intensity of the spoiler pulse train. The wait time of 500µs within the loop was to reduce the duty cycle of the coil, avoiding overheating when subjecting the sample to the rapid pulses of the spoiler train.

T_{rec} would be varied and the resultant signals fit to:

$$S(t) = A\left(1 - exp\left(-\frac{T_{rec}}{T_1}\right)\right) \quad \text{(Eq. 1.5.3)}$$

Allowing T_1 to be extracted. Spoiler pulse trains found additional use throughout experimentation. In repeated measurements over time periods of comparable duration to T_1 the introduction of a spoiler pulse train between sequential measurements ensured that residual effects from the previous measurement sequence were not carried over into the current measurement.

Chapter 2: Measurements of Nuclear Spin Conversion in Water Isolated in an Argon Cryomatrix:

Section 2.1 Introduction:

This chapter provides a brief overview of the structure and nuclear spin isomers of water before moving on to discuss the experimental methods used to obtain macroscopic water-in-argon (H_2O@Ar) samples for NMR measurements. Steps are taken to verify the water concentration in the obtained samples and measurements of the characteristic NMR decay constants (T_1, T_2 and T_2^*) are taken. These are used to inform the construction of a measurement protocol for NMR measurement of NSC in the obtained samples. Challenges in the data collection process are addressed, before presentation of the experimental data, analysis and comparison to existing literature regarding the NSC of water in similar systems. The extracted rate constants for the observed NSC are presented at the end of the chapter.

Section 2.2: Spin Isomerism in Water:

Water is a three-atom polyatomic molecule comprising two hydrogen atoms covalently bonded to a singular oxygen atom. In ordinary water ($^1H_2{}^{16}O$) only the hydrogen atoms possess non-zero nuclear spin, being spin-half. Its nuclear spin isomers may therefore take total spin values of either I=0 or I=1, and the values its nuclear spin wave function may take are identical to those presented for ordinary dihydrogen in Table 1.2.1.

As for hydrogen the Pauli exclusion principle requires that the total molecular wavefunction for water under proton exchange be antisymmetric. Further, in the vibrational and electronic ground state the relevant component to consider is $\varphi_{rot}\varphi_{spin}$. The φ_{spin} component has already been identified as identical to hydrogen, leaving only φ_{rot} to address.

It is at this point that the differences between water and hydrogen become more readily apparent. Hydrogen is a simple diatomic molecule which may be modelled as a linear rigid rotor, Water meanwhile is an asymmetric top[23], having three differing moments of inertia about its principle molecular fixed axes. A schematic of the water molecule and how it aligns with these axes is presented in Figure 2.2.1 (overleaf). While the rotational energy levels of a rigid rotor may be indexed using simple J notation, the energy levels of the asymmetric top are typically indexed $J_{k_a k_c}$ where J is the total rotational angular momentum quantum number, and k_a and k_c represent the components of J projecting onto the a and c axes (see Figure 2.2.1) respectively. The symmetry of the rotational wavefunction of a particular $J_{k_a k_c}$ state may be inferred from the value of the sum $k_a + k_c$, even values indicate a symmetric state, odd antisymmetric. To preserve the antisymmetry of $\varphi_{rot}\varphi_{spin}$ overall, the $I = 0$ para-water isomer occupies $J_{k_a k_c}$ states with even $k_a + k_c$, while the $I = 1$ ortho water spin isomer occupies $J_{k_a k_c}$ with odd $k_a + k_c$.

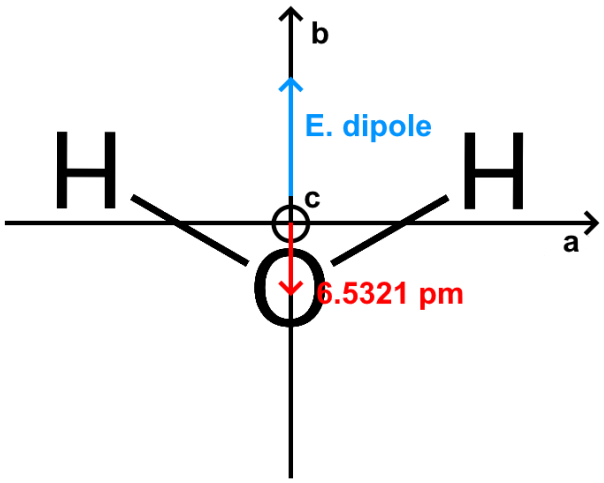

Figure 2.2.1: Simple schematic of Water presented on a molecular fixed axis as according to convention. The oxygen atom is represented as an O, the two hydrogen atoms as H's. The axes system uses [a,b,c] labels with the origin at the molecular centre of mass, roughly 6.5pm (red arrow) from the centre of mass of the oxygen nucleus. The axes form a right hand set, with the c axis projecting out of the page and the water molecule lying in the ab plane. The orientation of the permanent dipole in the water molecule owing to the strong electronegativity of oxygen is provided for reference in blue.

The ground $J_{k_a k_c}$ state is $0_{0\,0}$ and 0 is the only value of J which exhibits only one of the two spin isomers (para water). For $J > 0$ both isomers are present. At room temperatures and above the density of states where $k_a + k_c$ is odd is roughly 3 times that of those which are even. In the case that NSC in water is exceedingly slow (as predicted by theory) rapid cooling to cryogenic temperatures should result in all ortho-water molecules cooling to the lowest available ortho-state $1_{0\,1}$ and all para-water molecules cooling to the ground state $0_{0\,0}$. In accordance with their observed density of states at warmer temperatures the final ortho to para ration (OPR) in this case would be 3:1, this ratio being preserved indefinitely if NSC in water is strictly "forbidden".

For the purposes of an NMR experiment, Ortho $I = 1$ states are NMR active, while para $I = 0$ states are not. If signal from a water sample were to be measured during rapid cooling or heating then, following an initial change in signal owing to the shift in thermal equilibrium polarisation (Eq. 1.4.7), any further change in signal level would be attributable to a change in the amount of Ortho water present in the sample. Assuming nothing catastrophic has happened to the sample itself (i.e. it becoming detached from the substrate) this change may be attributed to nuclear spin conversion.

Section 2.3 Sample Preparation:

It has been previously shown that NSC rates can be directly influenced by the presence of paramagnetic contaminants, particularly O_2. Care must be taken during sample preparation to ensure such contamination is minimised. Further to this, the structure of any deposited Cryomatrix is dependent on its deposition conditions, any deposition method used must therefore be consistent between samples. The deposition procedures laid out in this section provide a method for reproducibly achieving mm-thick samples of H_2O@Ar suitable for NMR measurements. Samples were prepared by vapour deposition onto a cold (20K) sapphire surface via a 50μm

nozzle. A schematic of the assembly at the end of the cold finger is provided in Figure 2.3.1.

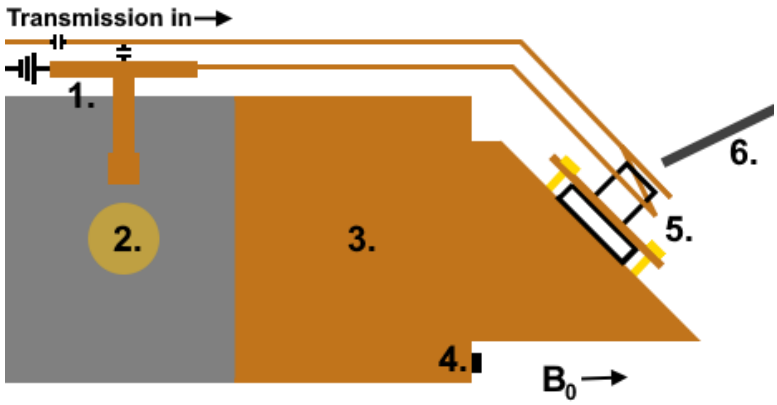

Figure 2.3.1: Diagrammatic representation of the end of the cold finger as set up for a H_2O@Ar experiment. The labelled components are 1. The coil mounting plate with accompanying tuning/matching capacitors, transmission and ground lines. 2. The (maximum 50W) cartridge heater used to heat the surface. 3. The oxygen free copper mounting block for the surface. 4. Mounting point for the Cernox CX-1050-SD temperature sensor. 5.The surface-coil assembly, consisting of a custom ground (Impex-Hightech) piece of optical grade III sapphire (5.5mm diameter polished deposition-side surface, black lines) compression mounted to the block using brass screws (gold). The transmission line forms a simple 2-loop (6mm inner diameter, 1mm diameter oxygen free copper wire) coil around the top of the block. The coil and deposition surface are mounted at 45° to the static field $\mathbf{B_0}$ rather than the ideal 90° to allow access to the surface by 6. The macro deposition nozzle (50μm diameter aperture).

The assembly depicted is housed within the bore of a superconducting magnet (5-6 T) under vacuum (average base pressure $<5\times10^{-7}$ mbar).

The system for preparing gas mixtures for deposition is displayed in Figure 2.3.2. (overleaf). The cylinder displayed in Figure 2.3.2 is an assembly of vacuum components, as such it may only be filled to atmospheric pressure without risk of leaking. All pressures in this section should be taken as absolute pressures. To fill the cylinder, deionised water was placed in an ampule and freeze-pump-thaw cycled until no gas bubbles were observed. When not in use the gas handling system was kept under rough vacuum ($\sim3\times10^{-2}$ mbar), except for the water ampule, argon line and region beyond the “Nozzle Isolation Valve” (Figure 2.3.2). The water ampule and argon line were kept isolated to maintain purity of their contents, the line beyond the isolation valve had its own dedicated turbo-pump. In preparation for cylinder filling the system was purged three times by filling the mixing cylinder to 800mbar with pure research grade Ar then allowing the gas to flow to the roughing pump. Once the pressure had returned to its baseline the line between cylinder and ampule was isolated from the rest of the system and the ampule was exposed to the cylinder. The system was left to equilibrate at room temperature (~21 ºC) until the pressure gauge at the ampule ceased fluctuating.

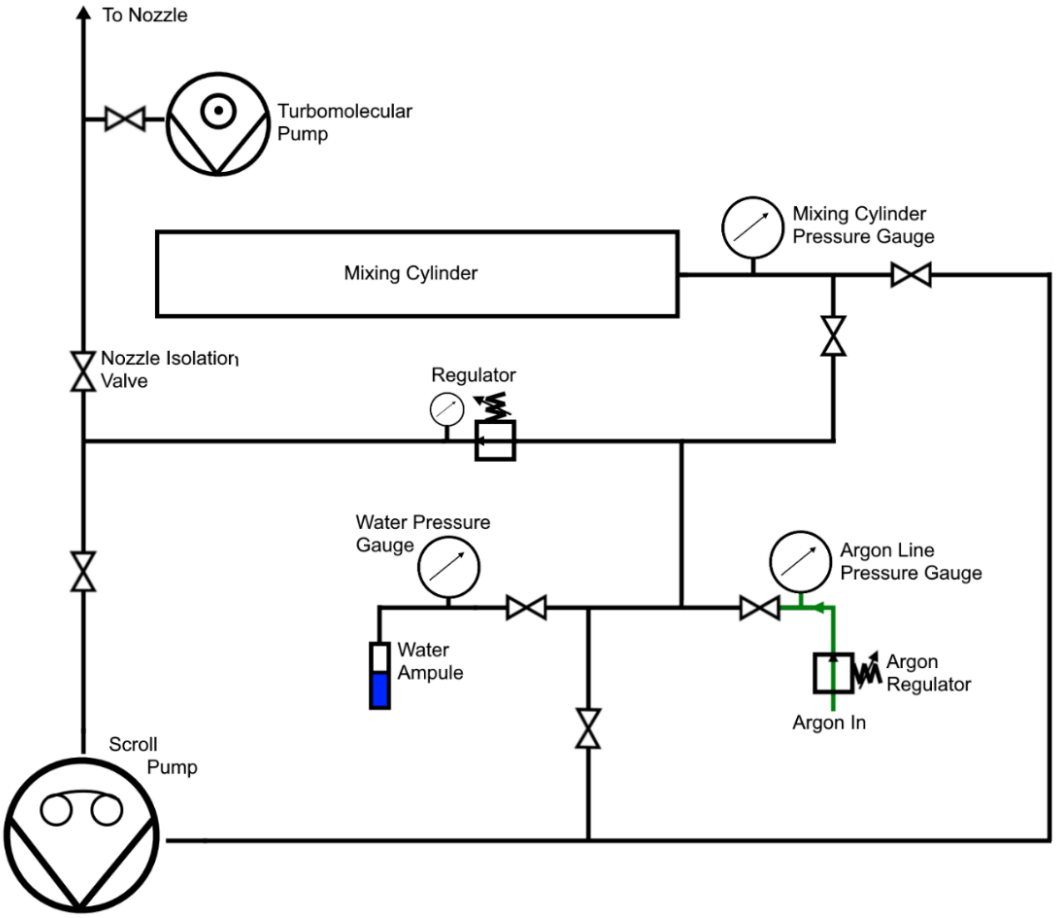

Figure 2.3.2: Diagram of the gas handling system for preparing and depositing gas mixtures. When not in use all valves except for the “Nozzle Isolation Valve” and the valves before the Water and Argon-line pressure gauges are left open to the scroll pump

After closing the ampule pure argon was introduced to the cylinder to achieve the desired dilution. For water NSC experiments the desired concentration was 10% H_2O@Ar requiring only a single filling of Argon, in cases where lower concentrations were desired the cylinder would be partially filled, pump and filled again to allow greater dilution without taking the cylinder above atmospheric pressure. Once the desired concentration was achieved the total pressure in the cylinder would then be pumped down to an absolute pressure of 100mbar total, suitable for direct unregulated introduction to the deposition nozzle.

To ensure the substrate was clean of any previously deposited material the heater (2. Figure 2.3.1) attached to the cold finger would be engaged and the substrate temperature increased to 200 K. On reaching 200 K the heater would be powered off and the substrate left to fall to its base temperature (~6.6 K). While this heater cycling was sufficient to clean the substrate of previous depositions, the expansion / contraction of the cold finger during the process would lead to tip of the cold finger, and therefore the substrate, settling in a different position each time. Precise / quantifiable positioning of the sapphire and nozzle is not possible with the current setup. To provide consistent conditions between depositions a photographic record (via an externally mounted camera) of the pre and post deposition conditions within the bore was kept. The nozzle would be positioned such that the live feed from the

camera best matched the pre-deposition photograph for the previous experiment. The nozzle would then be fixed in place and a new pre-deposition photo taken. An example pre-deposition photograph is provided in Figure 2.3.3 A.

With the nozzle positioned, the turbopump servicing the nozzle line was isolated via its dedicated valve. Samples used for NSC measurements were produced by introducing the 100 mbar of 10%H_2O@Ar previously prepared in the mixing cylinder directly (without regulation) to the nozzle via the nozzle isolation valve. Total deposition time was fixed at 10 minutes, the observed pressure drop at the mixing cylinder over this timeframe being negligible. At the end of the deposition period the mixing cylinder was isolated and the remainder of the gas handling system rough pumped until the nozzle could be re-introduced to the turbomolecular pump. The nozzle isolation valve was then closed and the turbopump reintroduced to the nozzle line. A post deposition photograph of the sample would then be taken, an example of which is provided in Figure 2.3.3 B.

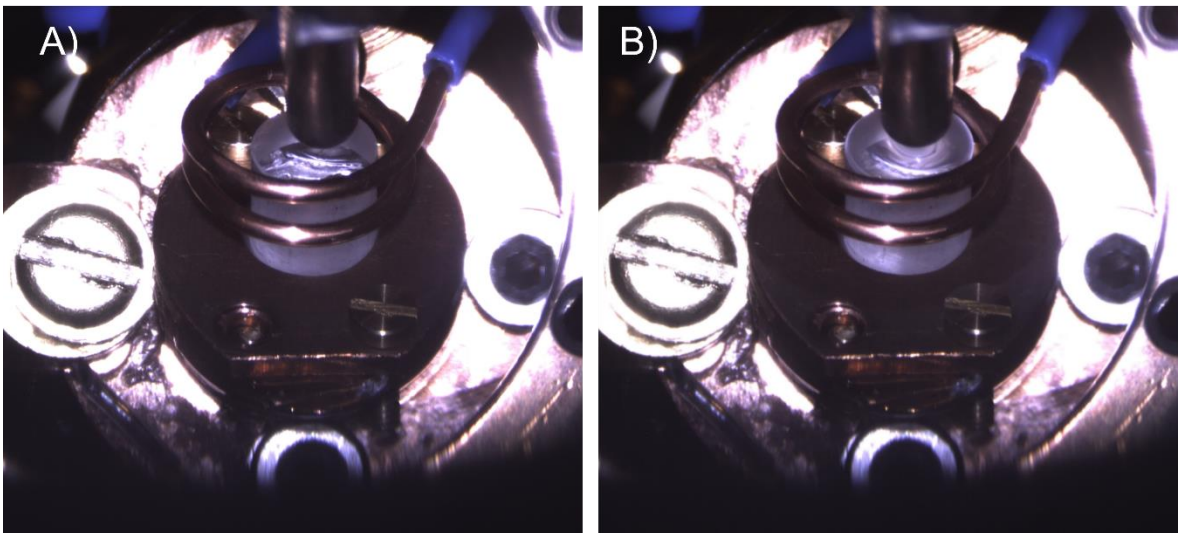

Figure 2.3.3: **A)** Pre-deposition photo of the sapphire substrate and surrounding NMR coil. **B)** Substrate as displayed in **A** post deposition. Evidence of deposition can be seen in the distortion in the image at the sapphire surface in **B** as well as in the whitening at the edges of the sapphire face and on the face of the copper support structure.

The transparent nature of the deposited sample makes identifying its presence difficult. Comparing Figure 2.3.3 A & B we see there is some circular distortion in the image at the sapphire surface in B, while in A there is a clear silver band corresponding to the indium beneath the sapphire. Additionally, there is whitening at the edges of the sapphire and on the face of the copper support structure in B. Very close observation of B reveals a darker band on the mounting plate below the coil, indicating a region where the coil shadowed the mounting plate from the gas leaving the nozzle. The sample is more easily identified in Figure 2.3.4, where (following experimentation involving changing sample temperature), the sample is seen to have cracked. The nozzle in this image is retracted, allowing a clearer view of the sample beneath. Notably we see there is a peak-like structure in the nozzle corresponding roughly to where the nozzle was positioned during the deposition. The overall thickness of the sample is difficult to ascertain. The nozzle was measured to be within 3-3.5mm of the surface. No significant decrease in pressure over the duration

of the deposition was noticed, indicating that the sample did not reach and block the nozzle itself.

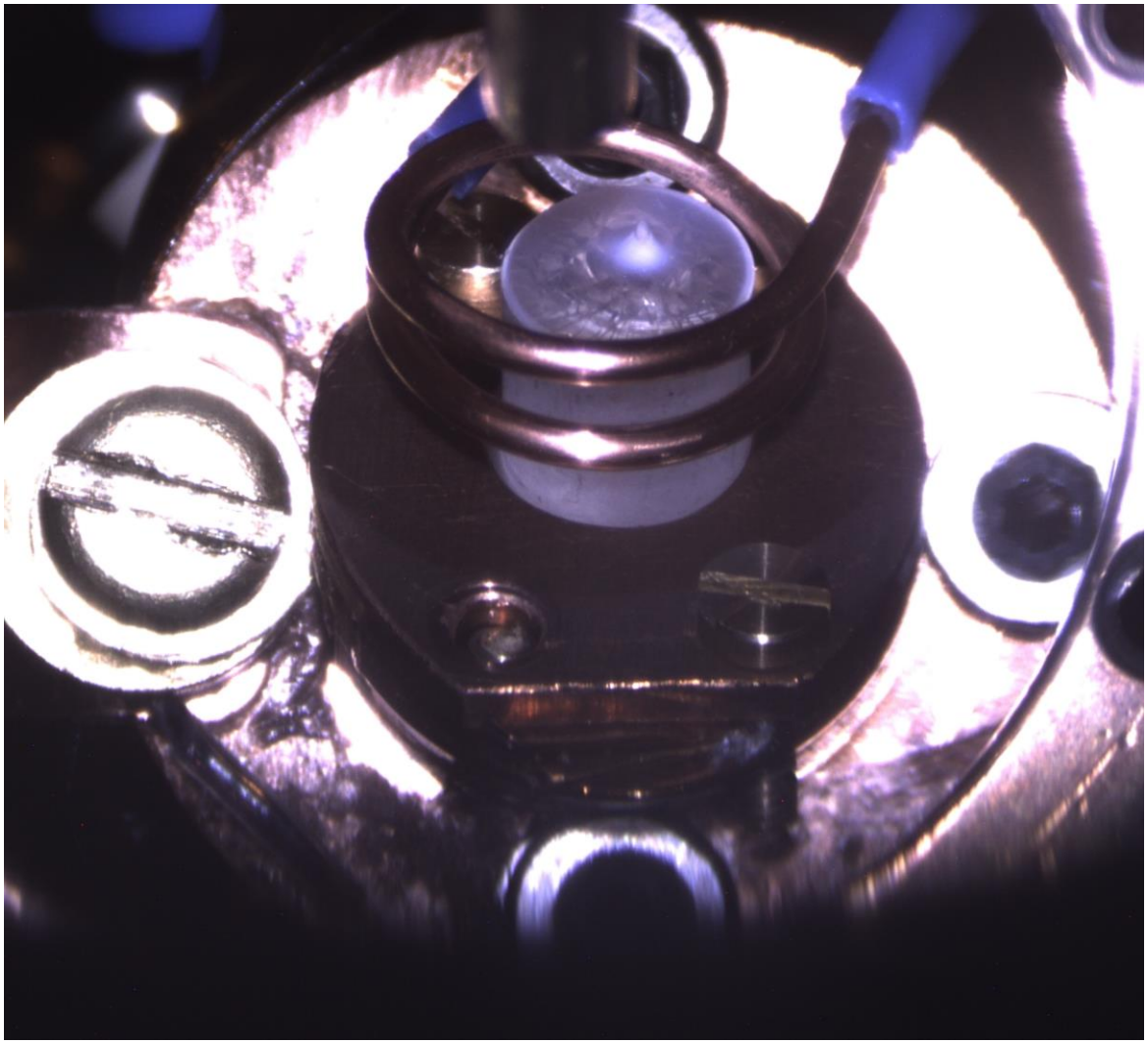

Figure 2.3.4: Image of the same sample presented in Figure 2.3.3 B, with nozzle retracted and sample displaying cracking following a temperature jump (See Section 2.6). A clear “peak” in the sample is observed, corresponding to the previous position of the nozzle. This peak appears of similar size to the diameter of the wire in the coil (1.0 mm).

Comparing features within the image, the peak in the sample appears to be of similar scale to the diameter of the wire (1.0 mm). The peak is estimated to be between 1 and 3 mm tall dependent on the depth of the remainder of the sample serving as its foundation.

Section 2.4 Verification of Sample Concentration:

Previous work using infrared spectroscopy[5] has identified both water concentration and sample temperature to be important factors impacting NSC rate. It was initially assumed that the concentration of water within the sample would be equal to the concentration of water prepared at the mixing cylinder. Initial testing showed this not to be the case as no correlation was observed between the concentration of water in the initial gas mixture and signal strength, signal to noise ratio (SNR) or observed NSC rate. It was suspected that the nozzle, being in poor thermal contact with the outside of the bore and emitting thermal radiation within the cryocooled shroud of the cold finger, may be colder than the rest of the gas handling pipework. A cold nozzle could lead to condensation of water on the nozzle walls and a reduction of the water vapour pressure. Provided the temperatures were not low enough to lead to condensation of argon, the overall result would be a reduction in water concentration at the sample. It was decided that the nozzle temperature and concentration at the sample would need to be investigated.

Impact of Nozzle Temperature:

To investigate nozzle temperature a T-type thermocouple (copper-constantan) was spot welded to the nozzle barrel. A photograph and accompanying schematic of the result is given below.

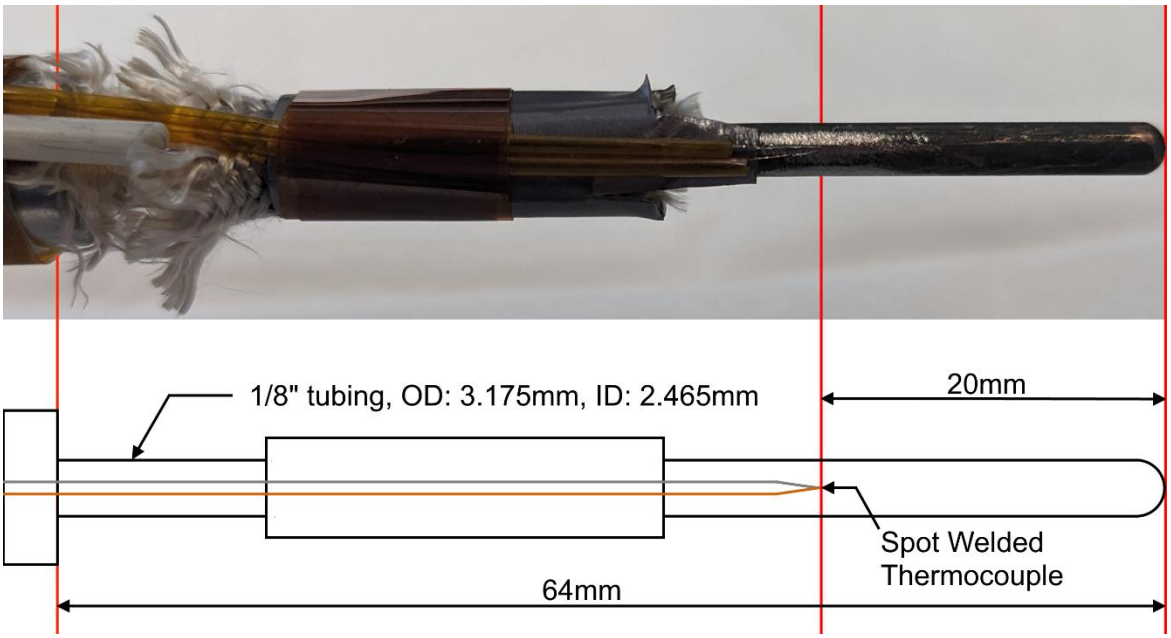

Figure 2.4.1: Photograph and schematic of the 50µm nozzle and spot-welded thermocouple. The stainless steel of the nozzle appears black due to oxidation which occurred during annealing of the part to any remnant magnetism. OD and ID represent outer and inner diameter respectively.

As can be seen in Figure 2.4.1 there is a displacement of 20mm between the point at which the thermocouple was spot welded and the end of the nozzle. It is expected that the coldest point on the nozzle would be the nozzle tip, as it protrudes furthest into the cold surroundings of the IR shroud. Ideally the thermocouple would have been spot-welded at this point. This was not done for two reasons, firstly, the surface of the nozzle required filing to expose clean steel to spot weld to. Debris from filing and distortion from the applied force posed a risk of either blocking or distorting the

50μm hole at the nozzle tip. Secondly, as can be seen from the copper-coloured discolouration in the image (right hand side, Figure 2.4.1), the nozzle would sometimes contact the NMR coil. Attaching the thermocouple in this region would risk breaking the spot weld or bringing the thermocouple wires in contact with high voltage NMR pulses. The thermocouple was therefore affixed further up the nozzle barrel.

The thermocouple leads were connected to a vacuum feedthrough outside of the bore. The temperature at this feedthrough was monitored via a platinum resistance temperature detector with a nominal resistance of 100 Ω (Pt100-RTD). The sensing element was secured to the stainless-steel body of the feedthrough with aluminium tape. The reading of the Pt100-RTD was used as the temperature for the reference junction of the thermocouple, the thermocouple itself being read by a multimeter connected across the feedthrough pins.

The nozzle was positioned as it would be for a deposition. To ensure the coldest possible nozzle surroundings the surface heating was initially left off. A thermocouple reading was taken after the surface temperature had stabilised at 6.1 K. The measured nozzle temperature was 266K, well below the average 293 K (room temperature) reported by the Pt100-RTD. The surface heating was engaged and the surface stabilised at 200K (the highest temperature the substrate would foreseeably be taken to under normal working conditions). At 200K surface temperature the nozzle thermocouple reading was 264K, paradoxically lower than was observed for the colder surface. A repeat of this measurement taken later when desorbing a sample, the measured nozzle temperature in this case being 268K. There are two major takeaways from these results. Firstly, the nozzle temperature is indeed lower than room temperature at the point measured, implying the temperature at the tip of the nozzle is colder still. Secondly, the temperature of the nozzle is not directly related to the temperature of the surface. Given the localised nature of the surface heating and the poor thermal conductance from the surface to the other cold surfaces in the bore, we believe the nozzle temperature is related to the temperature of these other cold surfaces. The best candidate surface in this case is the IR shroud of the cold finger, as it is in close proximity to the nozzle and unlikely to change temperature during surface heating.

The nozzle is observably colder than room temperature, with the exact temperature at the tip being unknown and the temperature at the thermocouple having been observed to vary between 264 and 268 K (average 266 K). The 100 mbar of 10% H_2O@Ar gas mixture used during deposition has a partial pressure for water at 1 mbar. This is well above the partial pressure expected at 266 K of ~3mbar. It is likely then that water is condensing on the walls of the nozzle. Estimating the concentration of water leaving the nozzle based on temperature is not possible as the relevant temperature is unknown, and it is unclear if the gas is at thermal equilibrium with the nozzle before leaving. To get an accurate read of the sample concentration the concentration of water must be measured directly from the gas in the magnet bore during deposition.

Concentration testing with H_2O:

It is not possible to directly measure sample concentration at the substrate with the current setup, however, with the introduction of a pulse counting quadrupole mass spectrometer (Hidden analytical, HAL PIC 301) at the front opening of the magnet bore it is possible to measure molecules scattering from the sapphire substrate back towards the mass spectrometer. By introducing different concentrations of H_2O@Ar to the nozzle and looking at the readout from the mass spectrometer it is possible to see changes in water counts proportional to the concentration in the prepared gas mixture.

It has been determined that the nozzle temperature is more dependent on the temperature of the IR shroud than the temperature at the deposition substrate. Ideally the substrate would be kept hot to reduce the amount of material sticking to it and providing more gas to sample with the mass spec. Conversely, the cooling cannot be disengaged entirely, as it also cools the IR shroud believed to be responsible for cooling the nozzle. Disengaging the cooling would mean measuring in a situation which does not match normal NSC measurement conditions. Measurements are therefore confined to surface temperatures within the 6-200 K temperature range previously tested with both the heater and cooling on. With the cooling on, the rest of the cold finger / shroud is therefore expected to act as a cold trap for water (and to a lesser extent argon) which could impact measurement at the detector. This can be overcome by ensuring that the length of gas exposure from the nozzle is sufficient to achieve a steady state of adsorption/desorption with these cold traps. The point at which the water counts for a given concentration plateau will be taken as the steady-state count and compared to counts at the same condition for other concentrations.

The process to prepare gas mixtures of varied concentration was in-line with the procedure described in Section 2.3. The water was freeze-pump-thaw cycled in the ampule (see Figure 2.3.2) until no bubbling was observed. The mixing cylinder and gas lines up to the nozzle shut-off valve were purged 3 times with pure argon, and the ampule was opened to the mixing cylinder to equilibrate. With the expectation that we would need to work at low concentrations the ampule was kept in an ice bath at ~1°C for the duration of equilibration, resulting in a lower vapour pressure of water and reduced need for dilution (and resultant wastage of research grade argon). Gas mixtures of 0.1, 0.5 1 and 2% H_2O@Ar were tested, being prepared in ascending order of concentration to reduce the impact of any water remaining in the system post-purging on observed counts. The first test coincided with the cold-surface nozzle temperature test, the substrate temperature being at 6.1K with the nozzle in its deposition position as outlined in the previous section. 100mbar of the desired concentration of H_2O@Ar was introduced to the nozzle and the counts at the mass spectrometer observed. The results are displayed in Figure 2.4.2 below.

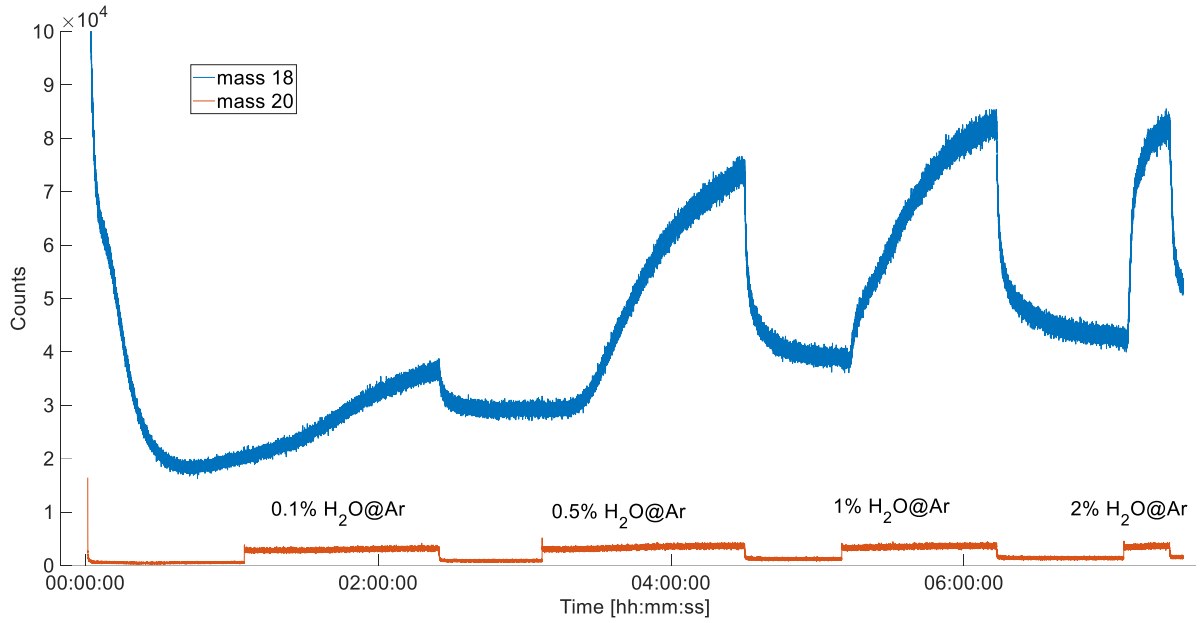

Figure 2.4.2: Mass spectrometer counts for masses 18 (blue, normal water) and 20 (orange, second ionisation peak of argon) at the mouth of the NMR magnet bore during exposure to varied concentrations of H_2O@Ar at the nozzle at a surface temperature of 6.1K. Exposures and corresponding concentrations aligning with the labelled peaks in the mass 20 data.

Figure 2.4.2 follows two masses, 18 and 20. Mass 18 is assigned to H_2O, mass 20 the second ionisation peak of argon. While mass 40 would be preferable for tracking argon counts, the overwhelming concentration of argon in the bore during these measurements would not allow the multiplier to be set at a sufficient level to also see changes in mass 18. According to the manufacturer of the mass spectrometer[ref] mass 20 should give roughly 10% the counts of mass 40. The relative sensitivities for different species are not accounted for in Figure 2.4.2, unmodified counts for differing masses should not be compared quantitatively without accounting for said differences in sensitivity.

00:00:00 in Figure 2.4.2 represents the point the multiplier for the detector was turned on. Counts for both mass 18 and 20 seen to initially start high before rapidly falling. Mass 20 is seen to stabilise on the order of a few minutes while mass 18 does not reach a minimum for at least an hour. During this initial stabilisation time the setup was left alone and the first concentration to be tested (0.1%H_2O@Ar) was prepared in the mixing cylinder. The introduction of this gas mixture corresponds with the rapid (on the order of one minute) rise in mass 20 just past the one-hour mark. When the nozzle was closed (02:30:00) the decrease in counts at mass 20 was equivalently quick, the intervening time seeing only a very gentle increase. The rapid increase / decrease in counts and lack of significant change over the time the nozzle is open suggests rapid establishment of steady-state argon coverage of the cold surfaces in the bore. This aligns with expectations, even at low temperatures we expect argon to have a much higher vapour pressure than water and the concentration of argon being introduced is high, resulting in a rapid approach to equilibrium.

In the same timeframe (1:00:00-02:30:00) the increase in mass 18 counts was much more gradual. In the interest of having sufficient time to measure all concentrations

the nozzle was closed at the point the counts appeared to just have begun plateauing (approaching 02:30:00). The initial decrease in mass 18 counts at this point is observed to be on a similar order to that for mass 20 (on the order of a minute) however, the decrease tails off plateauing at a baseline level that is well above the initial level pre-introduction of gas. This drift in the baseline water counts is seen throughout the experiment. The most likely origin for the increase in baseline is the formation of layers of water molecules on different surfaces within the bore of the magnet. The rate at which these layers form / deplete will be some function of the amount of water introduced, the surface temperature, surface material and microscopic structure of the surface the layer is forming on. Before the introduction of any water these surfaces can be thought of as a pump, with their pumping speed being reduced as layers of water form on them. The lower the pumping speed (the more water coverage) the higher the pressure (and therefore counts) will rise.

Varying baselines aside, once an equilibrium is established between the water leaving the nozzle and the water stuck to the various surfaces in the bore, it is expected that (to a first approximation) the counts will scale linearly with concentration of water at the nozzle. This does not seem to be the case. Looking back to Figure 2.4.2, despite having comparable baselines the mass 18 counts for both 1% and 2% H_2O@Ar seem to plateau at a similar level. Further to this, even with its lower starting baseline the counts for 0.5% H_2O@Ar plateau at a level only slightly below that for 1%. The most immediate conclusion we can draw is that the concentration coming out of the nozzle is not the same as concentration initially introduced to it. The fact that the 1% and 2% counts are seemingly equivalent suggests the sample concentration is at most 1%. The fact the 0.5% counts are slightly lower than the 1% counts suggests that the sample concentration is at least 0.5%. Overall, this places the sample concentration at between 0.5 and 1% H_2O@Ar. A backing pressure 100mbar implies a partial pressure of water of 0.5-1mbar in this case, equivalent to the vapour pressure of water between 246 and 253K. While the average measured nozzle temperature was 266K, this was not recorded at the coldest point of the nozzle, it is not unreasonable to expect that the tip of the nozzle could reach the 245-255K range. The conclusion taken from the above is that, if the partial pressure of water introduced to the nozzle is above the vapour pressure of water at the given nozzle temperature, the partial pressure of water leaving the nozzle will be lower than the partial pressure of water entering it. For the 10%H_2O@Ar gas mixture used in NSC measurements, the expected reduction in water partial pressure is on the order of 90-95%, corresponding to a sample concentration of 0.5-1%H_2O@Ar.

<u>Concentration testing with D_2O:</u>
To further explore this while avoiding some of the background related issues seen in Figure 2.4.2 the experiment was repeated with D_2O@Ar for a wider range of concentrations. Concentrations of 0,1,2,4 and 8% D_2O@Ar were conducted at a surface temperature of 200K and are presented in Figure 2.4.3 A. while concentrations of 0.1, 0.5, and 1% D_2O@Ar were conducted with a 6.1K surface and are displayed in Figure 2.4.3 B. Gas mixtures were prepared as for the H_2O@Ar test

with the H_2O in the ampule being substituted for D_2O. A backing pressure of 100mbar at the nozzle was used for all concentrations.

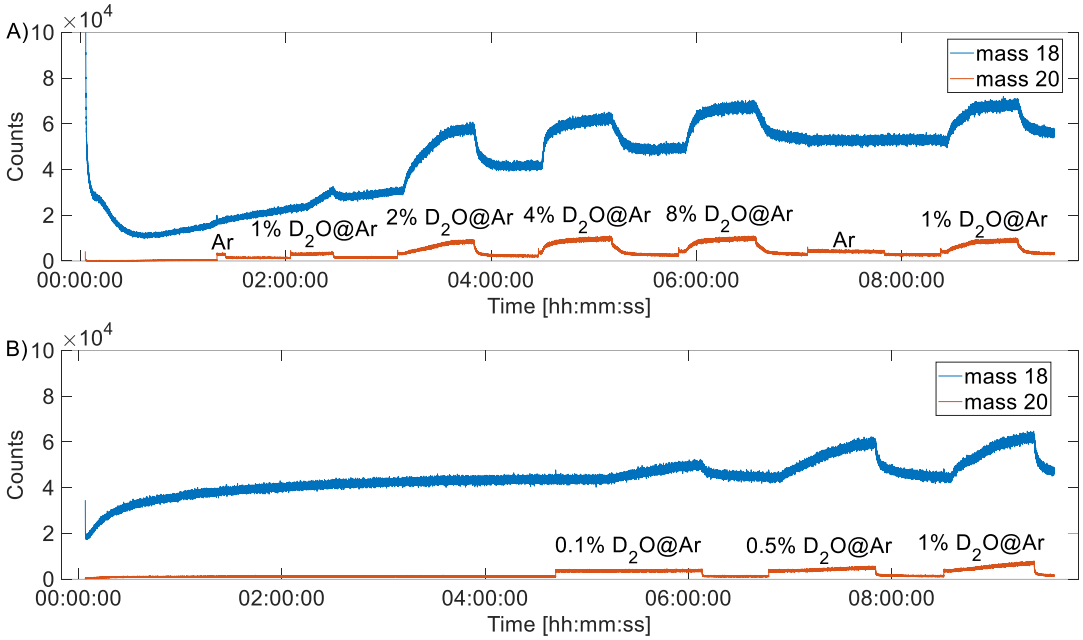

Figure 2.4.3: Mass spectrometer counts for masses 18 and 20 before during and after introduction of varied concentrations of D_2O@Ar as labelled. **A)** 0 (pure Ar), 1,2,4 and 8%, 200K surface temperature. **B)** 0.1, 0.5 and 1%, 6.1K surface temperature. It should be noted that mass 20 in both figures accounts for both the first ionisation of D_2O and the second ionisation of Ar.

It was hoped the choice of D_2O (mass 20) would lead to all exposure-related count changes in Figure 2.4.3 being confined to mass 20. Given the same relative sensitivity was used for data collection in both Figure 2.4.2 and Figure 2.4.3, the relatively stable argon mass 20 background could be negated by comparing the two measurements with and without D_2O. As will be seen, this was not the case.

The initial sections of Figure 2.4.3 A and B are very similar to the initial section of Figure 2.4.2. The initial values for masses 18 and 20 start high coinciding with energisation of the multiplier before falling towards some baseline value. As was the case for mass 18 in Figure 2.4.2, the mass 18 counts for Figure 2.4.3 A and B initially reach a minimum before beginning a steady climb despite the absence of any introduction of gas from the nozzle.

In Figure 2.4.3 A where nozzle D_2O concentrations above the previously observed “maximum” in H_2O sample concentration were to be tested this was ignored and experimentation began around 1:20:00 with a brief introduction of pure argon. The result of this was a sharp, rapidly plateauing increase in mass 20 counts, some deformation of the growth rate in mass 18 counts is also observed but was not sufficient to comment further on. The rapid fall off in mass 20 at ~1:25:00 coincides with the closure of the nozzle. The pure argon exposure was followed by exposures of sequentially increasing concentrations of D_2O@Ar [1,2,4 and 8%] as labelled, with exposure being ended once counts in mass 18 appeared to have begun plateauing.

Increased counts are seen in both mass 20 and mass 18 for all D_2O@Ar concentrations. Mass 20 displays both the initial rapidly plateauing component previously associated with pure Ar, alongside a component which grows slowly throughout the exposure. The slower growing component is attributed to D_2O. While the final plateau height for the slower growing component is comparable for 2, 4 and 8% D_2O the initial 1% D_2O exposure was given insufficient time to reach its plateau and cannot be directly compared. Mass 18 again displays a slow rise in counts, these are indirectly attributed to D_2O as well, having likely arisen from proton exchange between the nozzle-introduced D_2O molecules and H_2O molecules present in the bore. As was the case in Figure 2.4.2, despite the increasing baseline, the mass 18 plateau count level for the 2,4 and 8% D_2O exposures seem equivalent.

The 8% exposure was followed by a second pure Ar exposure and a final 1% D_2O@Ar exposure. In the pure Ar exposure only a fast-plateauing component in mass 20 is seen. Combined with the lack of observable change in mass 18 counts, this confirms that the pump/purging process used in gas mixture preparation is sufficient to clean the gas lines and mixing cylinder of any residual water. It also suggests that the cold nozzle is not acting as a significant reservoir of frozen water between depositions. The final 1% D_2O@Ar deposition again displays the combined fast / slow plateauing behaviour in mass 20 and a slow plateauing behaviour in mass 18. The plateau count level for both mass 18 and 20 in the final 1% exposure are comparable to the levels for the 2, 4 and 8% exposures, suggesting a maximum concentration of ~1% D_2O@Ar at the sample.

Considering Figure 2.4.3 B, significantly longer detector stabilisation time was allowed to try and minimise the impact of the mass 18 baseline drift. This limited the number of concentrations that could be tested in the available measuring period. D_2O@Ar concentrations of 0.1, 0.5 and 1% were introduced sequentially, 0.1% D_2O@Ar exposure beginning at ~04:40:00. The plateau in mass 18 counts observed for this measurement is the lowest of all three concentrations tested. The mass 20 counts for this concentration exhibit a rapidly plateauing flat peak akin to those previously assigned to pure argon. The mass 18 counts for 0.5 and 1% D_2O@Ar both exhibit slow plateauing behaviour, the final count levels for both are comparable. The mass 20 counts exhibit a combination of fast and slow plateauing behaviour, the ultimate count level for the 0.5% exposure is slightly lower than that for the 1% exposure. As was the case for the H_2O experiment this suggests a minimum concentration at the sample of 0.5%.

The combined conclusion taken from Figure 2.4.3 is an observed concentration range of 0.5-1% D_2O at the sample. This conclusion aligns with the previous conclusion for H_2O. Finally, the overall conclusion of Section 2.4 is that control over final water concentration in the depositions is heavily restricted with the current setup. NSC measurements will therefore have to be limited to a single concentration.

Section 2.5 Sample Characterisation:

While the deposition method has now been validated and the concentration of the sample verified the question remains regarding if the sample produces NMR signal. Further to this, measurement of NSC will require a repeatable NMR measurement structure that can be run over a period of hours. To achieve usable signal levels construction of this measurement sequence needs to be informed by the NMR characteristics (specifically the NMR time constants, T_1, T_2 and T_2*) of the sample.

It should be noted that the following work assumes that the majority if not all detected NMR signal arises from bulk water isolated as individual molecules within the argon lattice. Existing IR work[5] shows that multimers of water will be present in the matrix at a concentration of ~1% H_2O@Ar, there is no reason that these multimers should not produce ^1H NMR signal. However, the limits on molecular rotation as well as influence of additional neighbouring protons from multimer molecules should lead to said signal having significantly different NMR characteristics from the bulk monomer. Finally, due to the low sensitivity of NMR in general, it is assumed that any signal that is present from the multimer will be negligeable in comparison to the bulk.

Foreword: several of the figures in this section refer to “extracted signal”, for the purposes of discussion this may be taken as proportional to echo height. A full breakdown of how the signal is extracted and processed is provided later in Section 2.7.

Presentation of an echo / T2*:

For the purposes of measuring NSC we want to capture as much of the signal (in the time domain) as possible, in practical terms this means picking an acquisition window duration that captures the echo without capturing too much noise either side of it. Using an echo measurement, the point at which the maximum in signal will arise can be predicted from the spacing between the π/2 and π pulse. What cannot be predicted from the measurement structure is the duration of the echo itself.

The easiest way to assess the shape of an echo is to measure one. Figure 2.5.1 (overleaf) displays the averaged result of an echo measurement on a H_2O@Ar sample with 16 repeats and a window size of 100μs. The characteristic rising and falling shape of an echo can be seen, with a maximum at 57μs. In common practice the rate of this decay is described using a single-exponential decay model, the time constant of which being T_2*. The value of T_2* may therefore be roughly estimated from identifying the point in Figure 2.5.1 where the signal falls to ~1/e of its maximum value. The maxima is at 57μs and the signal falls to ~1/e of its maximum at 79μs, T_2* may therefore be taken as ~22μs. Realistically, the echo seen in Figure 2.5.1 is not an ideal back-to-back exponent, implying a single exponent T_2* model is a poor fit. More pragmatically, the signal level at the left-hand side of the window appears to be at the noise level for this measurement, there would be no advantage in terms of signal to noise in measuring beyond it. The right-hand side is not possible to assess due to the premature closing of the receiver. Overall, a window of 100μs appears suitable for our needs.

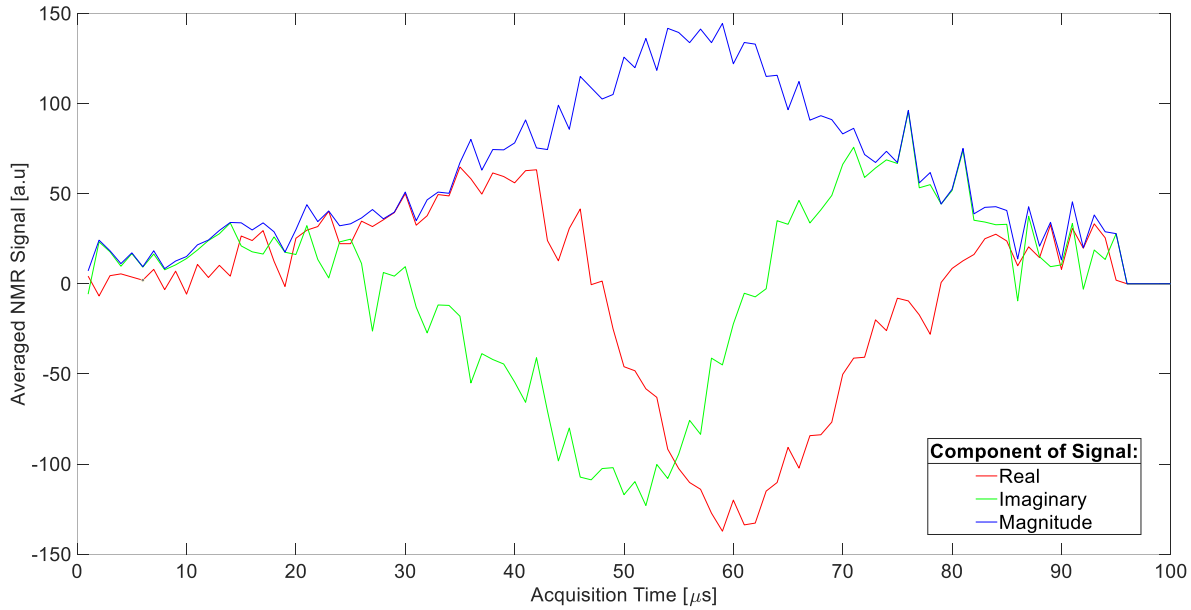

Figure 2.5.1: Average NMR signal for 16 repeats captured from a 1% (see previous section) H_2O@Ar deposited at 6K. Signal captured using an echo generating measurement sequence. Both components of the signal are shown alongside the combined magnitude (as labelled). The averaged signal is a clear echo with a centre at 57μs. The zero-signal level over the last few μs is attributed to the closing of the receiver. The recovery time between repeats for this measurement was 100s.

Measuring T_1:

According to existing literature[5] the NSC for H_2O@Ar systems can proceed on timescales of between several minutes to several hours dependent on both temperature and concentration of water. To capture rapid changes at the shorter end of the timescale the final measurement must be capable of capturing data at sub-minute intervals. Counter to this, the measurement spacing must also allow sufficient time for the net magnetisation to recover between pulse sequences. This recovery time is dictated by the T1 of the sample.

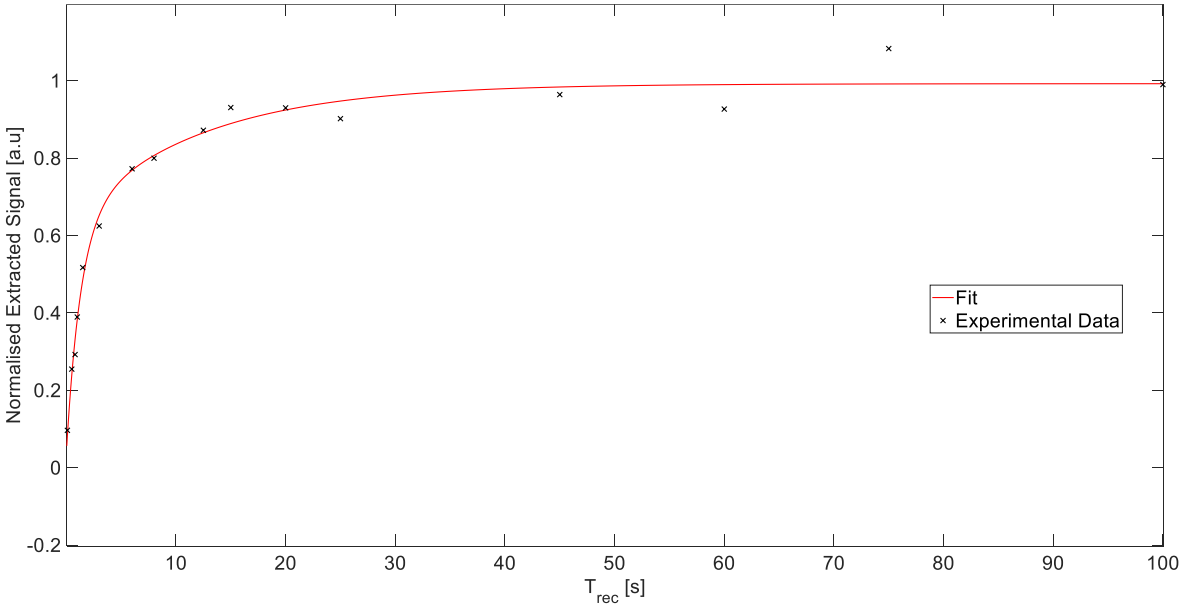

Figure 2.5.2: Resultant T1 curve for a T1 measurement on the same sample as shown in Figure 2.5.1. Black crosses represent experimental data while the red line represents the best fit to the data of the form of (Eq. 1.5.3). Roughly 75% of the signal has been recovered by the 5s mark.

Figure 2.5.2 presents a T_1 curve for the same sample which produced Figure 2.5.1. T_1 was measured by saturation recovery; the net magnetisation was destroyed using a saturation comb and then left to recover for a variable recovery time interval (T_{rec}). An echo measurement sequence was then sent. The resultant Signal v.s. T_{rec} curve allows for an assessment of the T1 of the sample.

The first thing to note regarding Figure 2.5.2 is that the best fit line (red) does not follow the typical single exponential form expected of a T1 measurement. A better fit was achieved using a bi-exponential recovery of the form:

$$Signal = A\left[1 - e^{\left(-\frac{Trec}{T_{1,1}}\right)}\right] + B\left[1 - e^{\left(-\frac{Trec}{T_{1,2}}\right)}\right] + C \qquad \text{(Eq. 2.5.1)}$$

This treats the sample as if it had two components with different T_1's. A and B represent the maximum in the signal arising from each component, C is a free parameter to account for the data not reaching zero, t is time, while $T_{1,1}$ and $T_{1,2}$ are the values of T_1 for each component. The origins of the two-component nature of the T_1 in this particular system are difficult to isolate. It may indicate the presence of water species with two different local environments or a mechanism for T_1 relaxation that involves more than just an individual water monomer and its immediate argon surroundings. Verifying the origin would require control over water concentration in the sample which is unfeasible with the current apparatus. Unknown origin aside, the results may still be used to identify a sensible repetition rate for the NSC measurement. The repetition rate used for the 16 repeats in Figure 2.5.1 was 100s. Looking at Figure 2.5.2 the signal level at 100s has long since plateaued, tracing the line back indicates a similar signal level could have been achieved at half the interval. Looking at the start of the figure, the greatest increase in signal is seen over the first 10s, 75% of the signal recovering by the 5s mark.

Another common NMR technique is the use of phase cycling to mitigate DC offset, slow drifts and pulse artifacts. A 4-phase cycle varying both the pulse transmission and receiver phases is sufficient for this purpose. At a repetition time of 5s per phase, each cycle would take ~20s total, allowing for 3 measurements a minute. Considering that averaging improves SNR by a factor of sqrt(number of averages), the loss of approximately 25% of the signal due to incomplete recovery of the longitudinal magnetisation would be outweighed by the 2x increase in SNR achieved by averaging over the four phases. As such a repetition rate of 5s per phase was identified as the best candidate for the NSC measurement.

Echo trains / T_2:

In a single echo measurement only one measurement is made per excitation pulse. The benefits of averaging on SNR were highlighted in the previous paragraph, leading to the following question: can more than one measurement be taken per excitation pulse? The answer to this question is yes. T_2* is the effective transverse magnetisation decay constant, it represents the combined effects of both reversible and irreversible decay processes affecting the transverse magnetisation. In an echo measurement it is the reversible processes, (decoherence of the spin projection due to differences in local field strength) that are reversed leading to a regrowth of signal

at the echo point. T_2 meanwhile is the constant governing the irreversible transverse relaxation processes alone. In cases where T_2 is sufficiently long (when compared to T_2*) it is common to measure an echo train, the initial π/2 , π pulse pair being followed by multiple sequential π pulses leading to multiple sequential echoes. One particularly useful echo train is the Car-Purcell-Meihboom-Gil (CPMG) sequence, where the phase of the π pulses are shifted π/2 radians from the initial π/2 pulse. The magnitude of the resultant echoes in these trains have been shown to decay exponentially following $\exp\left(-\frac{t}{T_2}\right)$.

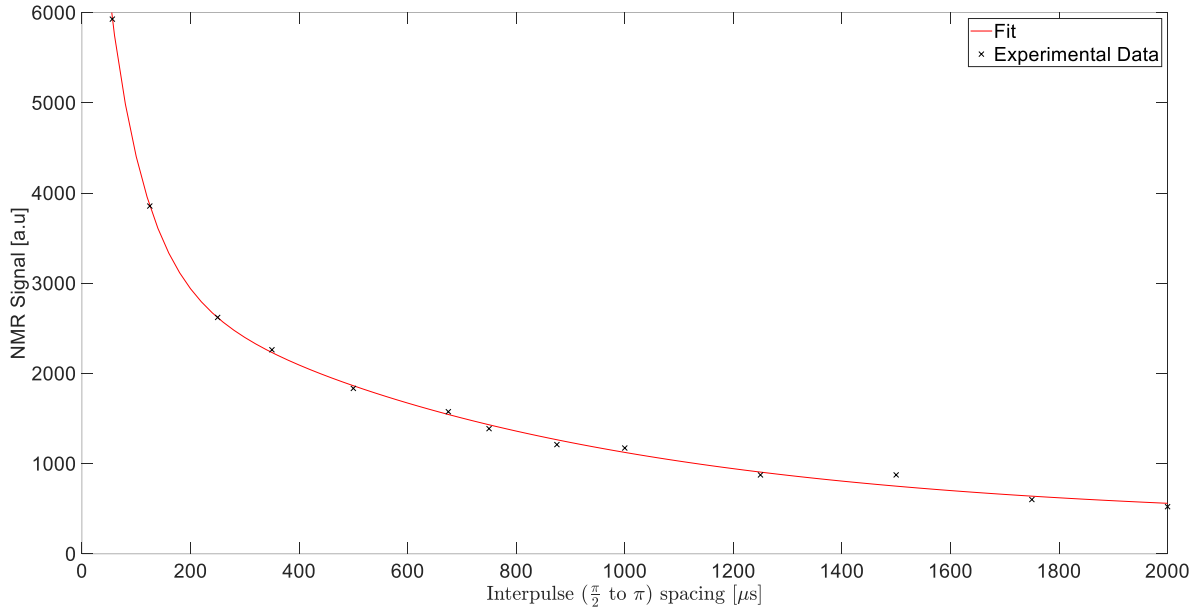

Figure 2.5.3: T2 measurement for the sample used to plot Figure 2.5.1. Experimental data is plotted as black X's, while a fit to the data is plotted as a red line. The fit used was of the form of (Eq. 2.5.2).

Figure 2.5.3 displays the results of a T_2 measurement on the sample. The measurement was achieved by varying the pulse spacing between the π/2 and π pulses in a standard Hahn echo measurement[21]. The resulting echoes were collected and their signal plotted against their pulse spacing. As was the case for T_1 measurements, the data were again best fit by a bi-exponential model which took the form:

$$Signal = Ae^{\left(-\frac{t}{T_{2,1}}\right)} + Be^{\left(-\frac{t}{T_{2,2}}\right)} + C \qquad \text{(Eq. 2.5.2)}$$

The variables in (Eq. 2.5.2) are akin to those in (Eq. 2.5.1). (Eq. 2.5.2), A and B are the maximum value of signal that each component can produce, C accounts for the signal not decaying to zero at infinite time, t is time, while $T_{2,1}$ and $T_{2,2}$ are the extracted values of T_2. Speculation regarding the origin of the two-component decay follows the same arguments as were presented for T_1, being sadly out of scope for investigation within this work. The measurement may still be used to determine whether employing echo trains will lead to an SNR improvement. The first echo in Figure 2.5.3 was captured at 120μs, this is the shortest echo time found to be measurable on H_2O@Ar samples with the current setup while preserving a 100μs

acquisition window. Accounting for the non-zero baseline, the signal in Figure 2.5.3 falls to around 1/3 of its initial value (~1850) at the 460μs mark. This implies that for an echo train measurement with 120μs spacing between its echoes the signal level can be expected to have fallen to below 1/3 of its initial value by the 4th echo. To confirm this an echo train with 120μs spacing may be run. Figure 2.5.4 A displays the result of such a measurement with 16 total echoes.

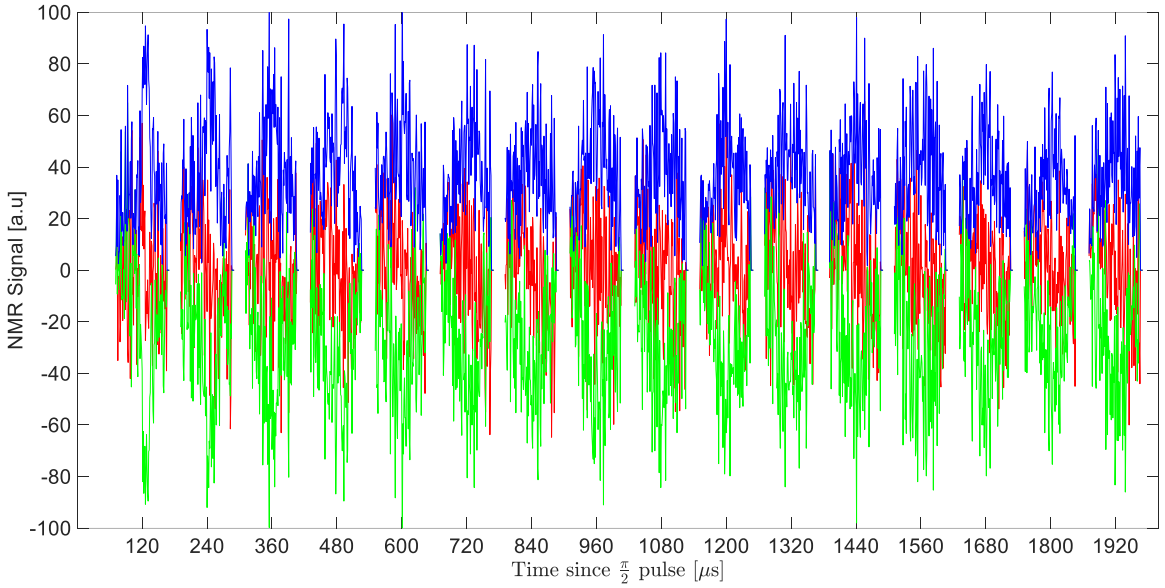

Figure 2.5.4: NMR signal produced by a CPMG echo train sequence with 16 echoes spaced 120μs apart. Averaged over 4 phases. The real (red) and imaginary (green) components are shown, alongside the overall magnitude (blue). Surprisingly, the average echo magnitude remains roughly constant across all 16 echoes shown.

It is immediately evident from Figure 2.5.4 that the echo train observed does not decay in a manner consistent with the decay seen in Figure 2.5.3. The expectation was a decay in echo magnitude leading to slightly less than 1/3 the initial signal level by echo 4 at 480μs, conversely Figure 2.5.4 displays echoes of consistent magnitude throughout its entire duration.

Figure 2.5.4 therefore displays evidence of some kind of extension effect which leads to longer-than-expected echo lifetimes. There is evidence in the literature[24] for this type of behaviour in solid systems with “dilute” spin density throughout the material. There are several candidate mechanisms proposed to explain such phenomena, the two prime candidates being “Stimulated Echoes”[24] and “Spin-locking”[14]. In the stimulated echoes explanation, the magnetisation is preserved due to the periodicity of an echo measurement. In brief some element of magnetisation which is not refocussed directly by the 180 pulse is instead stored at some off-axis angle, being brought back into the transverse plane and refocussed by a later pulse in the chain. The periodic nature of the sequence leads to repetition of this behaviour creating delayed echoes. The Spin-locking explanation relies on the suppression of T_2 effects in the presence of a strong RF field. Following a 90 degree pulse a rotating field is provided in the transverse plane at the resonant frequency and in phase with the magnetisation. In the rotating frame this field is stationary, the spin precesses with it and becomes “locked” into the transverse plane. This is most easily achieved

using a continuous RF wave but can be achieved using suitably frequent pulses. The transverse magnetisation will still eventually decay to zero (re-equilibrating with B_0) but the characteristic time (commonly denoted $T_{1\rho}$) will be different and usually longer than T_2. This seems to be the more likely explanation in our case, as rate of signal decay within the train was found to increase with increasing inter-pulse time. Confirmation beyond this simple observation would require deeper investigation.

Fortunately, lack of understanding of the mechanism for this phenomenon does not prevent its exploitation, and the fact that the train does not decay presents the opportunity to average many echoes after every excitation pulse.

Additional testing reveals that the extension effect leads to echoes of usable signal level all the way out to an echo number of 256 (the maximum possible with the current acquisition settings and limit of the receiver memory). Effectively, as many echoes as desired may be captured (coil arcing prohibiting, see Section 2.6). It may be concluded that any NSC measurement would benefit from employing echo trains rather than single echoes, the improvement in SNR gained by averaging over a given train being on the order of sqrt(number of echoes).

Section 2.6 Data Collection:

Measurement Method:

Only one of the two spin isomers present in water, the *I*=1 or “ortho” isomer, produces NMR signal. NSC of a water molecule from one total spin state to the other means a change in the number of water molecules which can produce signal, NSC can therefore be measured by monitoring the NMR signal before, during and after changing the sample conditions in a way which will alter equilibrium spin isomer populations in the sample . A technique commonly employed for this purpose in literature[5, 6] is a “Temperature Jump”, a rapid (here on the order <3 minutes) change from an initial temperature to a final temperature. All samples used in water NSC measurements were deposited at a substrate temperature of 20K. Initial testing revealed the signal level post deposition to be constant over a period of hours. This suggests the spin isomer populations of water within the sample rapidly reach thermal equilibrium after deposition at 20K. It could also be the case that NSC from room temperature at 20K is slow enough to be unobservable on a timescale of hours, but this is contradicted both by results in literature and experimental evidence shown later in this document.

Two different temperature jumps were conducted on each sample, first a “cooling” jump from 20-6K and then a “heating” jump from 6K-20K. The higher temperature of 20K was chosen to best match the deposition conditions seen in infrared-spectroscopy measurements of the same system[5]. The lower temperature of 6K was chosen as it was the lowest possible temperature we could reliably reach with the apparatus while still having active temperature control.

Before starting a measurement, the sample would be stabilised at its initial temperature. The stabilisation time required depended heavily on the history of the sample, measurements starting at 20 K for freshly deposited samples could be started immediately. Measurements starting at 6 K meanwhile required sufficient time for NSC to have completed following cooling. Typically, a cooling measurement would be conducted before a heating measurement, the cooling measurement terminating once the signal level (and therefore NSC) had observably plateaued. The measurement sequence (see below) was allowed to run for 16 complete cycles with the sample stable at its initial temperature to establish the initial signal level. With the initial signal established the temperature would be adjusted appropriately and the measurement left running to observe the change in signal. Each measurement was left running a long as was feasibly possible to enable detection of slow changes in the data.

Pulse Sequence for NSC Measurements:

Water NSC data was collected using a pulse sequence based on the Carr Purcell Meiboom Gill[22] (CPMG) echo train. The structure of the employed pulse sequence is outlined in Figure 2.6.1.

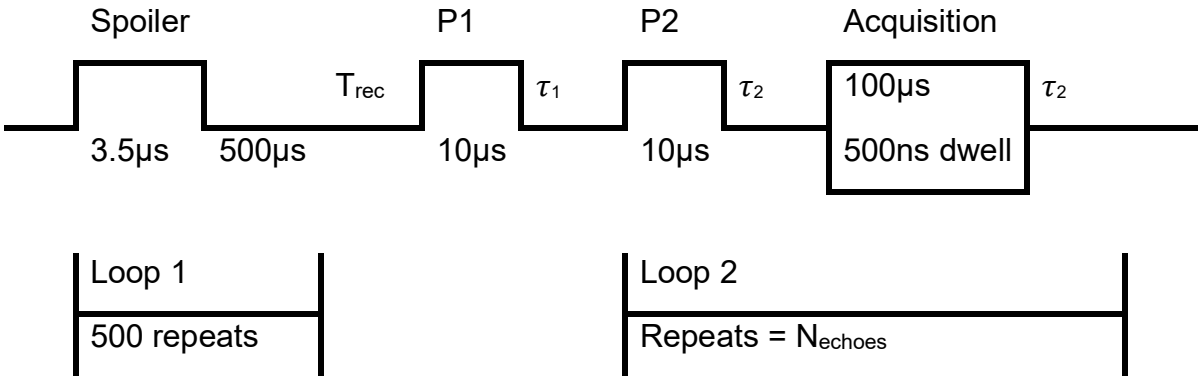

Figure 2.6.1: Schematic representation of pulse sequence used for water NSC data collection. This sequence is repeated 4 times per measurement point, using a different 4 phases in a cycling regime designed to eliminate DC background and minimise FID behaviour originating from P2.

The pulse sequence in Figure 2.6.1 contains three excitation pulses, represented as raised segments, the first and third of these are repeated (loops 1 and 2). The initial pulse labelled “Spoiler” is a saturation comb comprised of a large number (500) of closely spaced weak pulses, implemented to eliminate any net magnetisation in the sample at the start of measurement. The saturation comb is followed by the fixed recovery time “T_{rec}” where the sample is allowed to re-establish thermal equilibrium magnetisation. In combination with the saturation comb this recovery period ensures that each measurement starts with comparable net magnetisation, allowing for averaging over repeats of the whole sequence shown in Figure 2.6.1. In addition to providing improvement in signal to noise the repeated measurement structure also allows for the introduction of phase cycling to the measurement. The chosen phase cycling regime had four phases, being designed to eliminate DC noise in the data and to minimise lingering free-induction-decay (FID) like behaviour from P2.The value of T_{rec} was set at 5s, inline with the observations made in Section 2.5.

Pulses P1 and P2 in Figure 2.6.1 are the π/2 and π pulses of the CPMG measurement, with the π-pulse P2 being repeated a number of times equal to N_{echoes}. In an ideal experiment P1 and P2 would be short (1-5µs) intense pulses with magnitudes dictated by the results of a tip angle test to provide an exact π/2 and π pulse pair. It was not possible to implement such pulses here due to significant issues with coil arcing throughout the course of experimentation. Arcing was exacerbated at higher pulse magnitudes and larger numbers of echoes (N_{echoes}). The thresholds which resulted in arcing sufficient to render data unusable varied from sample to sample. As a countermeasure the pulse lengths of P1 and P2 were extended to 10µs allowing less intense pulses to be used. Sadly this was not sufficient to eliminate arcing at the optimum pulse intensities indicated by tip angle testing. The magnitudes of P1 and P2, as well as N_{echoes}, were chosen on a sample-to-sample basis. P1 and P2 intensities were kept as close to the ideal pulses as possible. Similarly, N_{echoes} was set as high as possible to provide the greatest number of echoes for averaging. The difference in pulse intensities between samples makes comparison of absolute signal levels between experiments impossible, but the results are still sufficient to allow the comparison of signal level vs time required for NSC measurement. The remaining timings present in Figure 2.6.1, τ_1 and τ_2

were chosen to accommodate the centring of the repeated echo within a 100us acquisition window (55μs and 5μs respectively).

The sequence was set up with enough repeats to cover up to a 16 hour runtime, which could be manually interrupted when external time constraints required.

Section 2.7 Raw Data and Definition of Signal:

Data from temperature jump experiments is initially exported as a complex vector containing the real and imaginary components of the signal. Initial formatting separates this vector into an [N_{echoes}, N_{phases}, $N_{repeats}$] matrix allowing every captured echo to be investigated individually. In the process of digital to analog conversion the receiver subtracts a reference frequency from the data; in the case of H_2O@Ar measurements the reference frequency is set to the resonant frequency for hydrogen at the current field strength. For a perfectly captured echo in a homogeneous field all of the signal would be contained in one component (real or imaginary) with the other component lying flat. Following application of the Fourier Transform, the ideal signal would be confined to a single peak at 0 Hz. As was mentioned in the previous section each "measurement" consists of 4 repeats, one per phase (N_{phases} = 4). Before further analysis we average over these 4 phases, resulting in a phase averaged echo train.

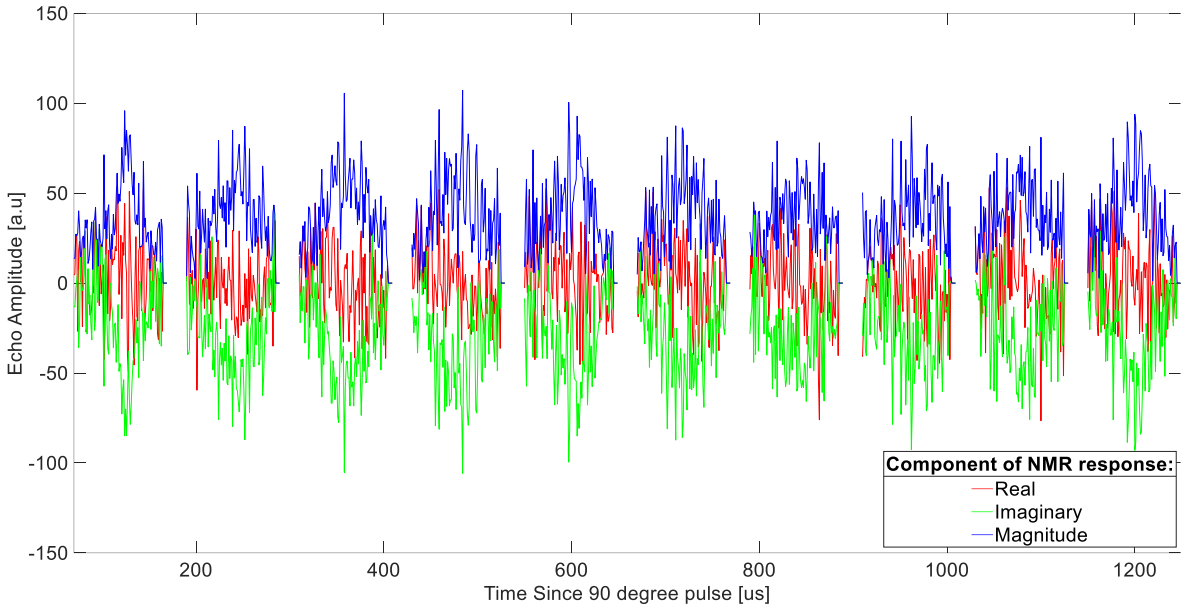

Figure 2.7.1: First 10 echoes of an echo train taken just after a temperature jump from 20 to 6.6K. Data is averaged over 4 phases. Real (red), imaginary (green) and magnitude (blue) components are displayed separately.

Figure 2.7.1 displays the first 10 echoes of a phase averaged echo train captured immediately following a temperature jump from 20 to 6.6K. A series of evenly spaced echoes are observed, as may be expected of CPMG measurement. The echo-lifetime extension effect is clearly visible, no obvious decay in echo magnitude is seen over all 16 echoes in Figure 2.7.1, despite measurement of T_2 (Figure 2.5.3) suggesting that 2/3 of the signal should have vanished by the 4th echo. Taking the decay in magnitude to be negligible an average can be taken across all echoes in the train.

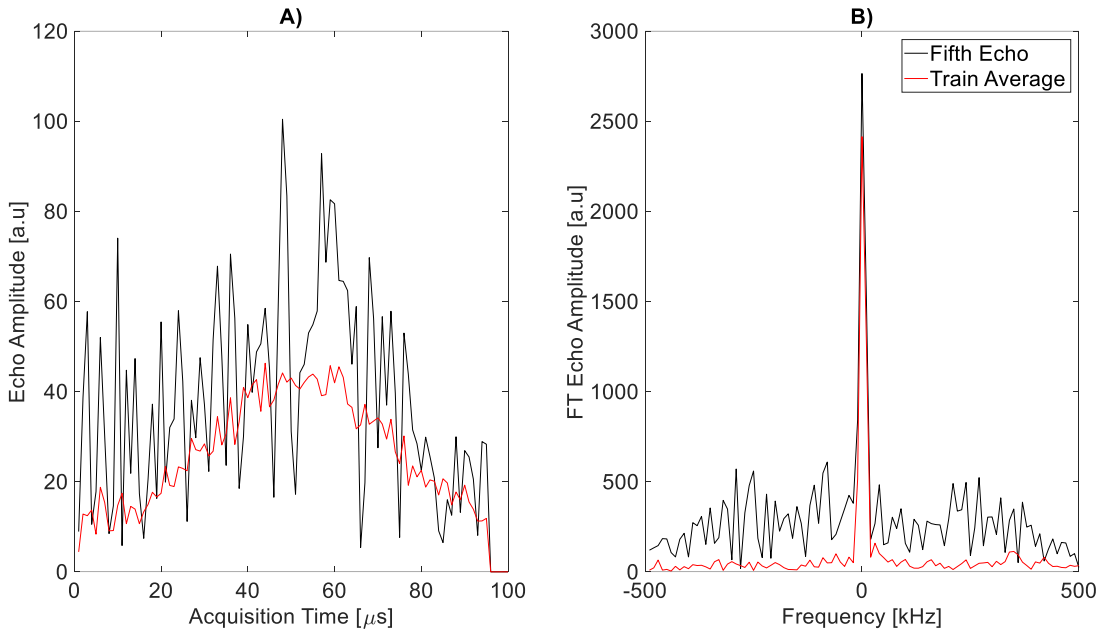

Figure 2.7.2: **A)** Magnitude of 5th echo in Figure 2.7.1 (black) plotted magnitude of average of all echoes in the train (red). **B)** Magnitude of Fourier transforms of the echoes plotted in A.

Figure 2.7.2 A displays the average over all echoes in a phase averaged echo train (red) plotted over a single echo from the same train (5th echo, red). The reduction in noise between the black and red lines is evidenced by the reduced point-to-point variation in height. Figure 2.7.2 B displays the FT of said averaged echo (red solid) and single echo (black solid). Comparing the red and black lines, the central peak for both remains in the same place, while the magnitude of the red line is slightly lower. The point-to-point variance in the red line is also lower than in the black, mirroring observations for Figure 2.7.2 A. The “noise level” in the data is reflected by the height of the regions outside of the central peak. It is worth noting that the noise level in the black line appears to be greater towards the centre of the frequency range. There are several possible reasons for this. One is that the noise in the system itself is not white, having varied intensity across multiple frequencies. Another alternative is that the receiver circuit, being tuned to a specific frequency, is most sensitive to noise close to the tuned frequency. Regardless of the noise profiles origin, the clear decrease in the height of the side regions (black to red) shows the noise-reducing benefits of averaging. The decrease in peak height is comparable to the decrease in the noise level suggesting the reduction in peak height can be attributed to reduction of some noise component at 0 Hz.

The final value defined as the signal, ‘*S*’ for the purposes of measuring NSC is obtained by taking the average magnitude of the peak and subtracting the average magnitude of the side regions. For all water NSC measurements the chosen frequency range for the side regions was 110 to 210KHz and -190 to -290KHz. Ideally the whole region outside the peak would be sampled, this was complicated by the presence of transient peaks at high and low frequencies in some experiments. These are attributed to external radiofrequency interference, the chosen frequency range is the largest span within which no such interference was observed.

Section 2.8 Pre-Processing / Factors Impacting Signal Extraction:

Plotting “S” at the midpoint in the time taken to measure each point allows observation of the trend in signal vs. time and therefore the progression of NSC. However, before jumping directly into analysis it is important to consider if there are any factors in the data which could impact our signal extraction method. After careful consideration three factors emerge relating to the T2* of the sample, the overall shape of individual echoes in the train and distortion of individual echoes due to electrical arcing in the probe. Each factor shall be considered separately and an overall pre-processing scheme that can be applied immediately before extraction of the signal will be identified.

Window Size, T_2* and Pulse artifacts:

The measured (Section 2.5) T_2* of the tested samples was ~10us, meanwhile the acquisition window used in measurements is 100us long. The order of magnitude difference between these two factors is a potential problem as while the large window makes it easier to spot the echo and helps account for any unknown delays in the pulse transmission which could shift the echo position, it also leads to the capturing of regions where the echo has either yet to emerge or has largely decayed. These regions primarily contain noise, including them in a signal calculation only makes the data more difficult to interpret. To remedy this a mask is introduced to the data which sets all values outside of the identified echo range to zero.

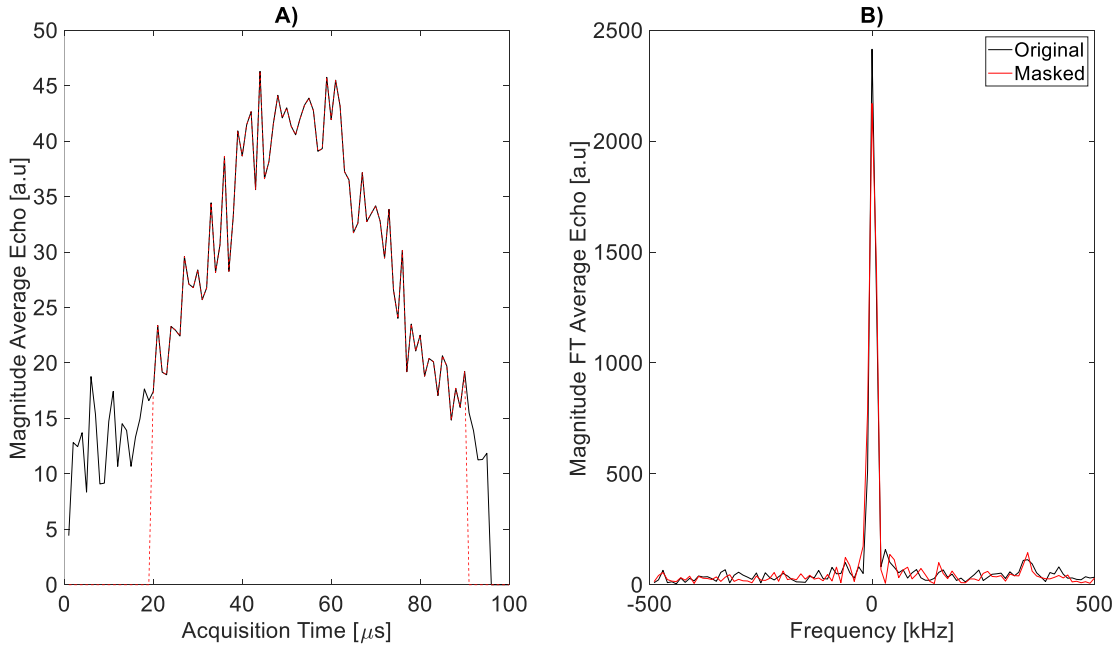

Figure 2.8.1: **A)** Average echo from a phase averaged train (black) plotted under the same echo post masking (red dashed). **B)** Fourier transform of the average echo (black) and masked echo (red solid) plotted in A.

Figure 2.8.1 A) shows both an unmasked average echo (black) and its masked counterpart (red dashed). Several features of note are present, firstly there is a clearly defined echo “hump” shape between 20 and 90μs. In the black line either side of this region there are sharp increases in signal. The right hand side appears to be what in this text shall be referred to as a spike (discussed later). The left hand side appears to start high, then decay towards some lower value. Two possible origins for

this decay-like behaviour at the start of the window are coil ringing or free induction decay (FID). The latter arises from the sample itself, the idea being that to some component of the sample our NMR pulse may appear closer to a π/2 pulse than a π pulse and as such will produce the expected FID curve. This is something we have attempted to mitigate using phase cycling. The alternative is that the decay is an artifact of "ringing" in the circuit, noise arising from lingering excitation of the electrons in the coil following the pulse.

Regardless of the origin of these artifacts, the application of the mask both removes them from the equation and ensures that the echo is sampled only while significant signal is present. As a third benefit it also excludes any "spikes" in the side regions of the window from being included in signal calculation, though it cannot account for any within the unmasked region (e.g. 40μs Figure 2.8.1 A), the process for addressing these is discussed later.

<u>Echo Shape:</u>

Section 2.7 noted that the amplitude of each sequential echo is largely constant over the whole echo train, allowing for averaging over all echoes to produce an improvement in signal to noise. What Section 2.7 did not consider was whether the overall shape of the echoes also changed as the echo train progressed.

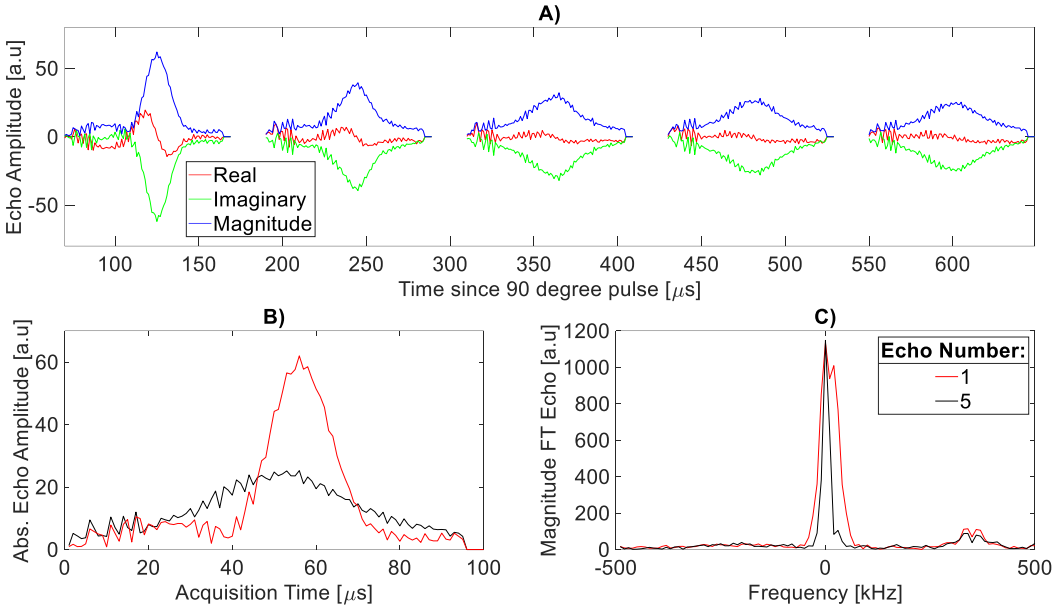

Figure 2.8.2: **A)** Average over first 5 echoes for one complete temperature jump measurement. **B)** 1st (red) and 5th (black) average echo magnitudes in A) plotted overtop one another. **C)** Magnitude of Fourier transform of average echoes 1 (red) and 5 (black) in A.

Figure 2.8.2 A displays the first 5 echoes in a train averaged over all trains in a temperature jump experiment. In this case averaging a slight decrease in echo amplitude over the first three trains is visible. More noteworthy than the change in amplitude though is what happens to the echo shape. All echoes plotted appear to have a distorted region at their beginning, this would be nullified if the masking procedure described earlier were applied to the data. Regardless, the largest difference is in the shape of the first echo compared to the last. Figure 2.8.2 B) displays the magnitudes of the first (red) and last (black) echo plotted overtop each

other. Even without normalisation it is clear to see that the first echo exhibits much more rapid decay, the echo peak itself being narrower. This narrowing is also present in the second and third echoes (not shown) although to a lesser extent.

A narrower echo indicates a more rapid decay of net transverse magnetisation and is matched by a wider bandwidth in the frequency domain. A speculative explanation could be that the repeated π pulse sequence does not have sufficient bandwidth to properly excite (and refocus) all spins in the sample. While not specifically related to just the first echoes in the train, in their paper discussing their initial observation of extended echoes under CPMG Ridge (see [24] figures 9 and 10) displays example echoes from the end of CPMG chains showing significant variation in shape with variation in the structure of the measurement itself. It is also noted that in the case of spin locking, said locking is reliant on the supplied RF field appearing static in the rotating frame[14], i.e. matching the resonant frequency at B_0, components out of phase with the resonant frequency (at the edge of the band) being less ideally locked. Speculation aside, properly understanding the origin of the narrowing of the first 3 echoes would require accurate modelling of the effects of the pulse train on the spins in the sample, a diversion not necessary to understand the simple signal vs. time measurements used in the study of NSC.

Figure 2.8.2 C) displays a much broader peak in the red line representing the magnitude of the Fourier transform of the first echo (red) compared to that of the fifth echo (black). Given the chosen definition of signal is reliant on the width of the peak this poses a problem as any change in the width of the peak represents a change in how signal is calculated. The remaining echoes in the train, for trains as long as up to 256 echoes, have been observed to have consistent shape alongside consistent magnitude and produce Fourier transforms with peaks of approximately equivalent width. Given the reason for the distortion in the first three echoes is not well understood it was decided to exclude the first three echoes from the averaging process when calculating the average echo for signal extraction.

<u>Spiking / Coil arcing:</u>
Perhaps the greatest experimental challenge faced in the process of experimentation was electrical arcing at the NMR coil. These arcs manifested as short (1 or 2 data points) high intensity spikes in the NMR measurement data. Often such spikes would be multiple orders of magnitude more intense than the signal level. The specific conditions leading to coil arcing were nebulous. Typically arcing was most severe during matrix deposition with the nozzle open to the gas supply, this would persist for a variable period after the nozzle valve was closed. Following cessation of arcing, arcing could begin again at any point during the transmission section of a measurement, occasionally no arcing would be observed during deposition only to begin again several hours later. No arcing was observed with a clean surface at the standard resting pressure of the bore [~1×10^{-7} mbar]. The location of arcs on the apparatus could also vary greatly, most commonly arcs were struck between the coil and grounded sample holder, but on occasion would occur away from the sample between the tank circuit capacitors and cold finger body. While arcs were occasionally observed in close proximity of the deposition, no appreciable change in the signal before and after prolonged periods of arcing were observed suggesting

that the sample itself largely unaffected. Some examples of the impact of arcing post averaging over a whole train were already shown in Figure 2.8.1 A, most concerningly at 40μs where there is a clear deviation from an echo residue of otherwise textbook form. The question arises then, what does the train that produced the average echo in Figure 2.8.1 A look like?

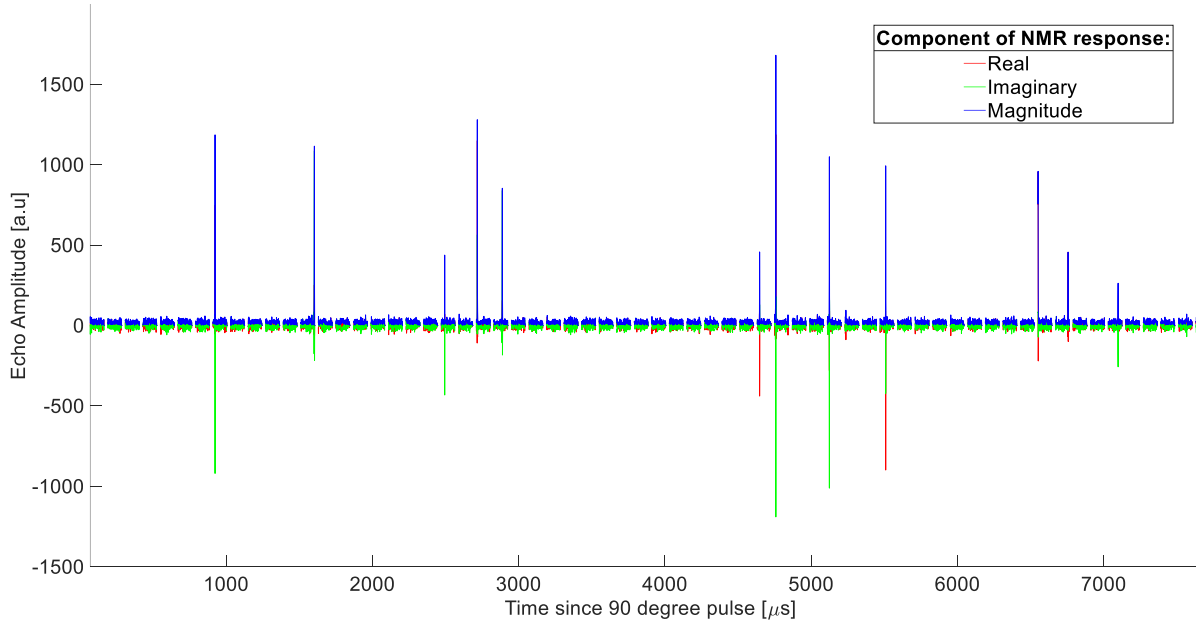

Figure 2.8.3: full echo train averaged to produce the black echo in Figure 2.8.1 A. All three NMR signal components, real (red), imaginary (green) and magnitude (blue).

Figure 2.8.3 shows the complete echo train in question. Of the 64 echoes present 13 have clearly identifiable spikes. In most cases these spikes are an order of magnitude larger than the signal level in the underlying echoes, plotting on a scale where their complete shape is visible renders the detail of each individual echo packet indistinguishable. Of the 13 spikes present only 2 are within what would be considered the “unmasked” region of the echo. One lies at the equivalent of 40μs acquisition time, the other at 60μs. The second of these appears to have averaged out in Figure 2.8.1 A, the first meanwhile tells us that the spike at 40μs arose from a single event.

The large difference in magnitude between echoes and spikes allows for construction of a simple filter which excludes echoes with spikes from averaging. A threshold which lies above the maximum echo magnitude is set and any echo which contains data points exceeding the threshold is culled from the data set. The ideal value for this threshold varies from measurement to measurement but with sufficient hand tuning it is possible to remove echoes with even comparatively small spikes without accidentally binning clean echoes. Figure 2.8.4 A) displays the same echo train as in Figure 2.8.3 following application of such a filter. Figure 2.8.4 B) and C) display the resultant average echo and Fourier transform of said echo (red) for Figure 2.8.4 A as compared to the unfiltered versions taken from Figure 2.8.3 A and B (black).

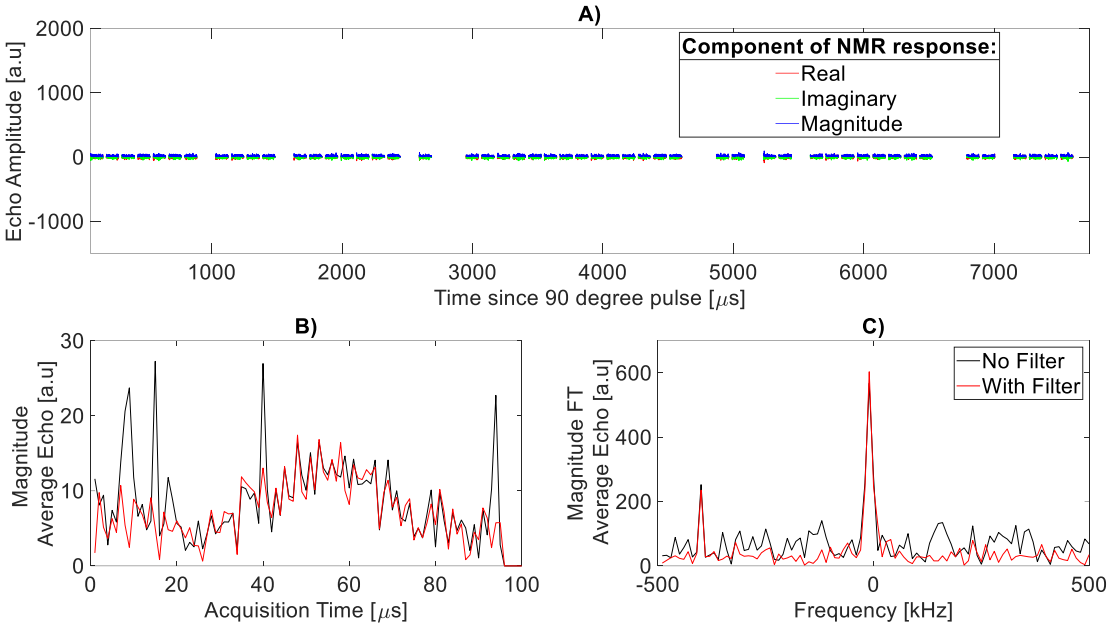

Figure 2.8.4: **A)** Equivalent phase averaged echo train to that shown in Figure 2.8.3 A, after removing echoes with spikes identified by the filter. **B)** Average echo magnitude arising from the unfiltered train (black) and its filtered counterpart (red). **C)** Magnitude of Fourier transform of echoes in B.

Comparing subfigure A in Figure 2.8.4 and Figure 2.8.3 we can see that the filter is working, all spike containing echoes in Figure 2.8.3 A are omitted in Figure 2.8.4 A. Comparing the black and red lines in Figure 2.8.4 B we see that the sharp spikes at the beginning and end of the echo, as well as that at 40us in the unfiltered data (black) are not present in the filtered data (red). The decaying signal at the beginning of the window is still present in both. Turning our attention to the Fourier transforms in Figure 2.8.4 C we note that the magnitude of the side regions in the red line (filtered) is markedly lower than in the black (unfiltered), with the exception of the peak at -400MHz which we again attribute to interference from some unknown transmitter source rather than thermal noise. These factors combined indicate that the filter provides a reduction in noise without any noticeable decrease in signal, despite the lower number of echoes used in averaging.

<u>Conclusions from pre-processing:</u>

In combination, the above methods form a pre-processing procedure that may be applied to the data before the signal is extracted, providing a reduction in noise and removal of influences which could bias the trends seen in the data. Up until this point we have largely discussed Fourier transforms of average echoes. In the code which runs the pre-processing, the initial averaging over phases is done in the time domain, while any further averaging (over the echoes in the train itself) is performed in the frequency domain after the data has been Fourier transformed. The order of these operations (taking the mean and applying the Fourier transform) does not impact the output in our case.

The full signal extraction process for a single data point, starting from a set of 4 phase cycled echo trains is therefore:

- Average over all 4 phases in the cycle, producing a phase averaged echo train.
- Apply the mask, setting any values outside of our region of interest in the time domain to zero.
- Identify any echoes which contain spikes by applying the filter.
- Fourier transform the data.
- Calculate the average over the Fourier transform of each echo, excluding the transforms corresponding to the first 3 echoes and any echoes identified as containing spikes.
- Calculate the magnitude of the average Fourier transform.
- Calculate the average of the central peak in the magnitude of the Fourier transform.
- Calculate the average of the magnitude of the side regions of the peak, avoiding any interference related peaks. This is our baseline.
- Subtract the baseline from the average magnitude of the peak taken in step 7, giving our final extracted signal.

The extracted signal may then be plotted against time, each data point lying at the midpoint in the time spanned by the 4 echo trains which make it up.

Section 2.9: Initial Analysis:

First Presentation of data: Cooling:

With pre-processing complete data from both types of experiment (heating / cooling) may now be presented.

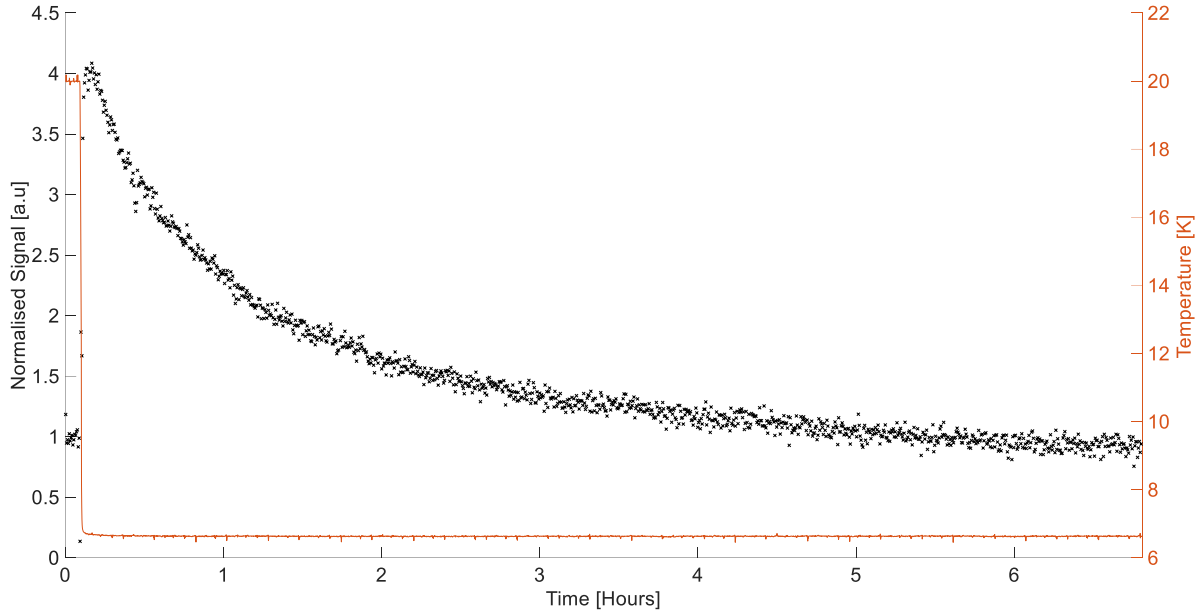

Figure 2.9.1: Example result of a “cooling” type temperature jump measurement on a ~1% H_2O@Ar sample. Signal from the NMR measurement is plotted as black x’s against the left-hand side y axis, one data point has been excluded due to overwhelming coil arcing. The data has been normalised to the average value of the initial plateau. The right-hand side y axis and line in orange show the surface temperature throughout the experiment.

Figure 2.9.1 displays normalised data from a cooling experiment (20 to 6K). 3 regions with qualitatively different behaviour are identifiable within the figure. The first is an initial plateau in signal between 0 and <0.1 hours, the surface is stable at 20K throughout this region. Immediately following this is a rapid change in the signal level, the signal first falls dramatically for a single data point before rapidly rising to a maximum. The steep gradient of the initial decrease results in it only being captured in a couple of data points in each experiment. These rapid changes align with decrease in temperature seen in the orange line, the maximum in signal aligns with the point the temperature stabilises at its minimum value. Finally, there is a slow decay in signal over the remaining time in the experiment, the temperature throughout this region (0.1-7 hours) is stable, reading 6.6K. The initial plateau in the signal level is attributed to thermal equilibrium at 20K. The data has been normalised to this level. The region containing rapid changes in signal level (during cooling) contains two competing effects acting on differing timescales. The initial decrease in signal level seen only for a single data point and the following rapid increase. The rapid increase is attributed to thermalisation within the Zeeman-energy levels of the system. As was discussed in the lower temperatures lead to a greater bias in Zeeman state population, corresponding to increased net magnetisation and NMR signal. The time taken for the increase in net magnetisation to develop is characterised by T_1. The temperature change we see in Figure 2.9.1 occurs over a period of a few (~3) minutes, much longer than the 5s taken for the majority of the

signal to recover seen in Section 2.5. With the temperature change being the slower of the two processes, the change in signal is expected to proceed in step with the temperature change, terminating once the temperature stabilises. This is reflected in Figure 2.9.1. The maximum signal level is attributed to the sample having its Zeeman-state populations at thermal equilibrium at 6.6K, while the Spin-Isomer populations of the sample remain at their 20K thermal equilibrium values (i.e. no NSC has yet occurred).

The initial decrease in signal seen at the onset of the temperature jump is more difficult to explain. The timescale of this process is clearly much shorter than T1 as it is only seen for a single data point and is sufficient to overwhelm any expected increase in signal arising from a change in Zeeman population. The current hypothesis is that this decrease is related to rotational effects, namely changes in the populations of energy levels within the rotational “ladders” associated with each of the two spin isomers present in water.

Finally, the decay in signal over the remainder of the experiment is attributed to nuclear spin conversion. Qualitatively the trend is as expected, the ground state of water is $I = 0$ $J = 0$, which produces no NMR signal. If ortho-para conversion is allowed to occur, then the signal is expected to decrease with temperature as the spin isomer population becomes biased towards the ground (non-signal producing) state. The decay constant for the process seen in Figure 2.9.1 appears to be on the order of hours, aligning with observations of NSC for water in literature[5, 12].

First presentation of data: Heating:

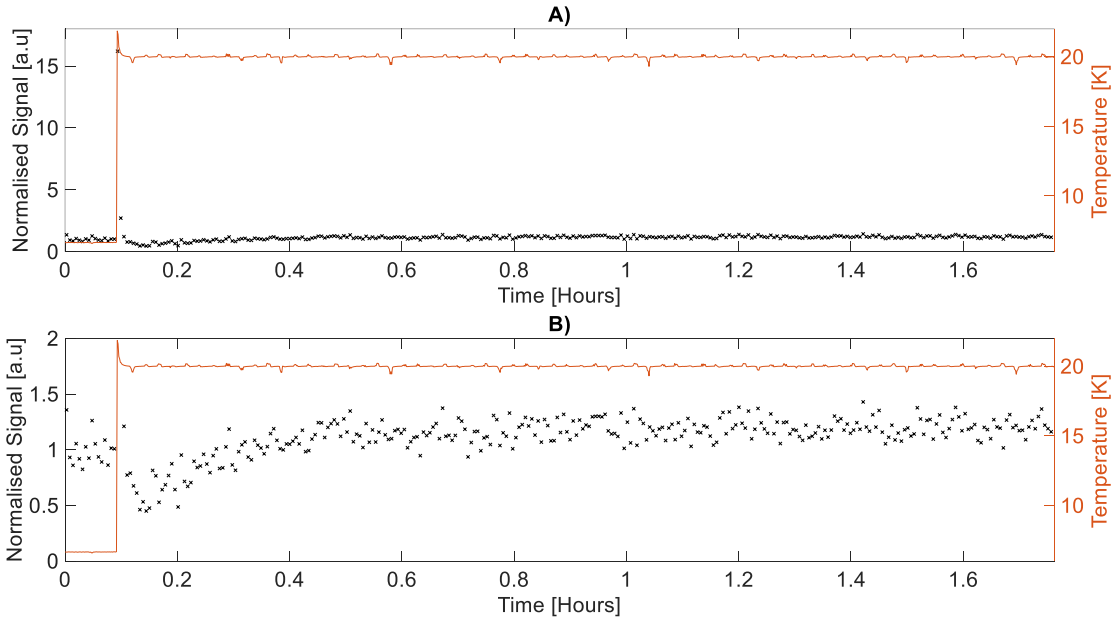

Figure 2.9.2: Example result of a “Heating” type temperature jump measurement on an ~1% H_2O@Ar sample. Signal from the NMR measurement is plotted as black x’s against the left hand side y axis. The right hand side and line in orange show the measured surface temperature throughout the experiment. Experimental data has been normalised to the average value of the initial plateau. **A)** All data. **B)** Data excluding high signal points immediately following temperature jump.

Figure 2.9.2 A and B display data from a “heating” type experiment. B displays a subset of A excluding data at the highest signal level for readability. As was the case

for Figure 2.9.1 the data can largely be divided into three sections. An initial plateau, a period with very rapid changes in signal and a slower change over a longer period.

The initial plateau is assigned as the thermal equilibrium signal level at 6K for this sample, the data are normalised to this value. The behaviour immediately following the temperature jump in Figure 2.9.2 is the opposite of that seen in Figure 2.9.1. In Figure 2.9.2 A we see an initial very rapid (1-2 data points) increase in signal, followed by a decrease. The decrease is more clearly identifiable Figure 2.9.2 B.

There is an observable minimum in Figure 2.9.2 B appearing at roughly 0.15 hours and taking a value of approximately 0.4, as will be discussed later this is likely not the “true minima” to be expected from theory. Beyond the observed minima the signal exhibits growth behaviour, reaching a clear plateau around the one-hour mark.

It is again difficult to assign an origin for the rapid change in signal at the point the temperature jump begins. In the case of heating (Figure 2.9.2) a rapid increase in signal is seen, while for cooling (Figure 2.9.1) a rapid decrease was seen instead. While the timescales of these rapid changes appear similar (<1s), the magnitude of the change is much larger for the heating experiment. Rotational population changes are again suggested as a potential source for this behaviour, the main evidence being the timescale of the process. In-depth study of these processes would require a greater time resolution and signal to noise ratio (SNR) than is achieveable with the current setup.

The decrease in signal level leading to the observed minima is attributed to thermal equilibration of the Zeeman populations in the sample. The growth in signal following the minima is attributed to nuclear spin conversion. The minimum in this case is difficult to assess, both due to the observably low signal-to-noise of the data and the fact that nuclear spin conversion on heating appears to occur on a faster timescale than for cooling. The difference in timescale is evidenced by the fact that the growth in Figure 2.9.2 plateaus at 1 hour while the decay in Figure 2.9.1 does not plateau until past the 7 hour mark. The observed minima in Figure 2.9.2 B is likely not the “true minima” associated with a sample at a “Zeeman temperature” of 20K that has yet to undergo any NSC. The rate of NSC appears to be fast enough that the two effects (NSC and thermalisation of the Zeeman energy) are overlapping at this point.

Signal Level Analysis: Introduction:

Before fitting and extracting NSC rates for the data presented in Figure 2.9.1 & Figure 2.9.2 the relative signal levels at different points within the measurements may be compared to assess whether they agree with existing theory. Two comparisons are of particular interest: the difference in signal level immediately before and after the temperature jump (reflecting the thermalisation of the Zeeman Energies) and the difference in signal level between the point immediately following the temperature jump and the end of the experimental run (reflecting the change in signal due to NSC). Both heating and cooling experiments will be considered, starting with the cooling data.

Signal Level Analysis: Cooling Data

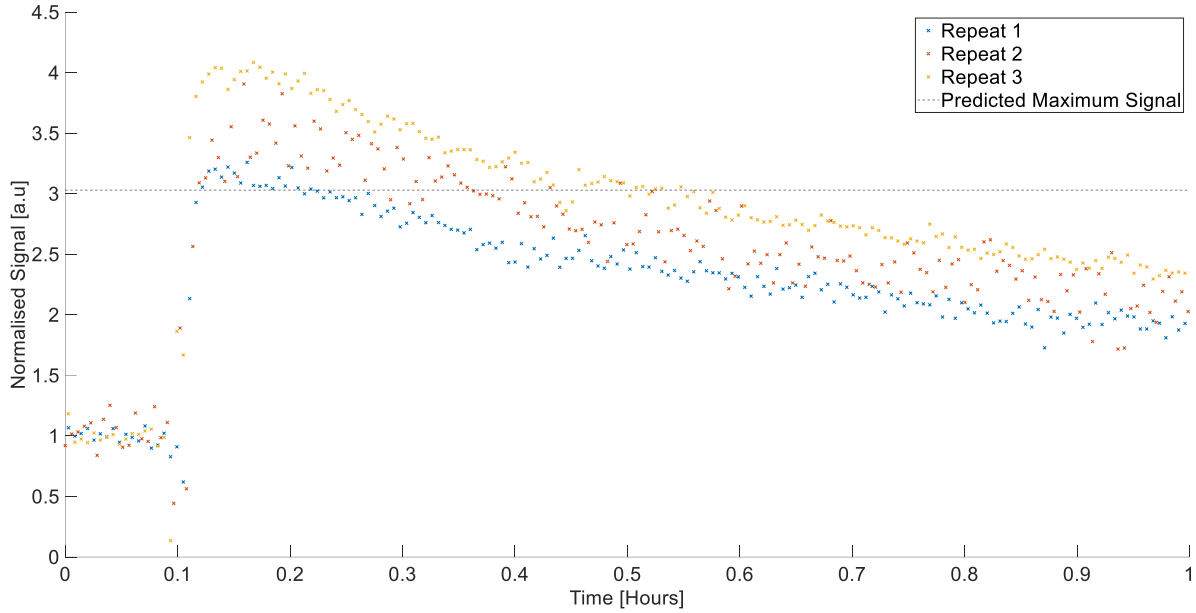

Figure 2.9.3: Normalised data from all three 20 to 6K temperature jump experiments, limited to just the first hour of measurement. The initial plateau lies at 20K, with the increase in signal indicating the change in sample temperature from 20 to 6.6K. The black dashed line indicates the signal level we would expect if the increase in signal could be attributed to changes in the Zeeman populations of proton spins in H_2O@Ar alone.

Starting with the difference in immediate pre/post-jump signal level, Figure 2.9.3 displays data from all three repeats of the cooling (20 to 6K) measurement. The data are normalised to their initial signal level, which corresponds to the sample being at thermal equilibrium at 20K. The black dashed line indicates the expected signal level immediately following the temperature jump provided the signal changes only due to thermalisation of the Zeeman energy of the sample. As can be seen, the factor change in signal is an increase of ~3x. This factor is calculated using the equations for the difference in spin population (up vs. down) for an ensemble of spin-half, as laid out in Section 1.4.

Looking closely at Figure 2.9.3, the first repeat (blue) gives the best fit to the prediction, only slightly exceeding the expected value of three. Repeats 2 and 3 fit more poorly, taking values of 3.5 and 4.0 at their maximum. Two potential explanations are presented for this discrepancy. Firstly, there may be a difference between the measured and actual temperatures of the sample. The temperature sensor is not directly attached to the sapphire surface and said surface is close to the nozzle, previously noted (Section 2.4) to be at a minimum temperature of 266K. With the nozzle easily being the warmest object in the bore it may represent a sufficient source of thermal radiation to create a temperature difference between the surface and the sensor. A second explanation may be that the choice of model is poor. While there is good reason to believe[14] that the simple ensemble of spin half model should accurately represent the sample, the fact remains that the hydrogen atoms in the sample are not an ensemble of non-interacting spin-half. The mismatch could simply be due to behaviour the model cannot account for. The variation in discrepancy between repeats does allow one conclusion to be drawn, whatever is causing it must also vary from measurement to measurement.

Further effort may be dedicated to identifying the source of the discrepancies following analysis of the second comparison point, the difference in signal level due to NSC. Figure 2.9.4 A through C display each repeat of the cooling data used in Figure 2.9.3 separately. The experimental data is presented as black X's, while the red dashed lines represent the predicted final signal level following complete NSC. These values are calculated from the signal level immediately following the temperature jump (the observed maxima of 3.2, 3.5 and 4 for Figure 2.9.4 A, B and C respectively) and the predicted change in spin-isomer population from rotational energy calculations. All three sub figures in Figure 2.9.4 display a final signal level above the prediction. What is more difficult to see in the figure is that the final signal level in all three experiments is consistent at ~0.925.

Temperature differences would again be a possible explanation for the difference between experiment and prediction, with the consistent final signal level despite differing initial (post-temperature jump) signal level requiring a different pair of temperatures for NSC to convert to and from for each repeat. Another potential explanation that was not presented when discussing the Zeeman-energies is that there is some source of hydrogen signal present that does not undergo nuclear spin conversion. This is a reasonable assumption to make, it is known[5] that even at concentrations lower than the 1% H_2O@Ar studied here there will be multimers of water present in the sample structure. These are unlikely to be rotating, said lack of rotation implying there can be no segregation of nuclear spin states between rotational energy levels and thus, no NSC.

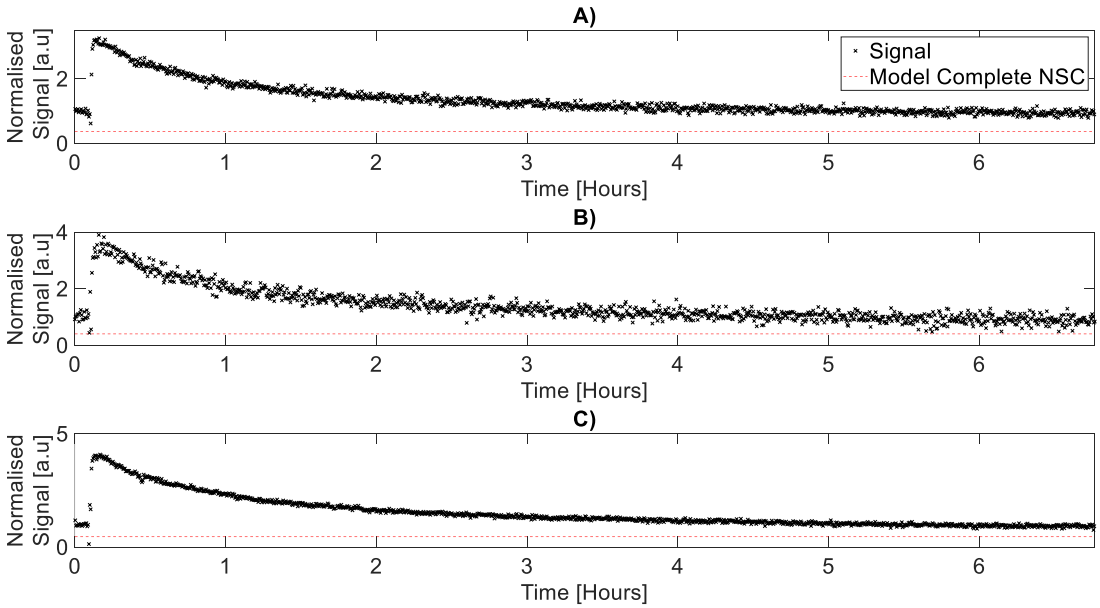

Figure 2.9.4: Plots of normalised signal versus time for all three cooling (20 to 6.6K) experiment repeats. Black x's represent signal. The red dashed line represents our best prediction for final signal level following complete nuclear spin conversion in each case.

Whatever the origin of the non-converting hydrogen species there is no reason that they would not produce a hydrogen signal. A higher resolution NMR measurement may have been able to separate out the signal from different hydrogen-containing species within the sample (via chemical shift), but this is not achievable with the current setup. In the event that non-converting species are present, they would

produce the expected increase in signal level following cooling as their Zeeman energies adjusted and would then remain at a constant signal level for the remainder of the experiment. The result being a final signal level higher than would be expected in their absence. The non-converting species would also serve as a further complication to the ensemble-of-spin-half assumption used in the Zeeman calculation.

In the case that the discrepancies are due to a temperature difference it should be possible to use the existing models to fit pairs of initial / final temperatures which give initial signal rises and final signal levels matching the experimental data. Figure 2.9.5 (overleaf) displays the result of such fitting, each repeat (1-3) of the cooling experiment occupying its own sub figure. The pairs of temperatures which best fit the experimental data are represented by the yellow cells in Figure 2.9.5, which agree with the experimental observations to within 1%. In all cases the best fitting initial and final temperatures are above the measured values of 20 and 6K. There is more agreement in the final temperatures between repeats than initial, with the maximum difference in final temperature between repeats being 0.65K while for initial temperatures the maximum difference is 4.2K.

While Figure 2.9.5 indicates that there are temperature pairs that could explain the experimental data using the existing models, it does not consider whether the temperatures it suggests are possible given the conditions within the bore.

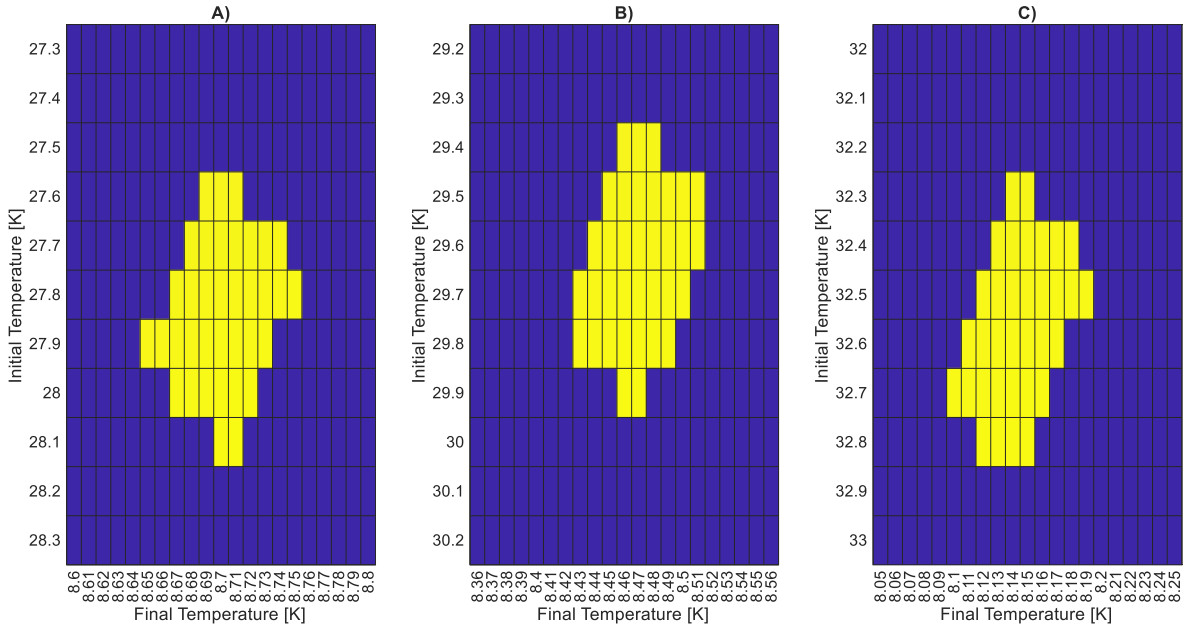

Figure 2.9.5: Maps of initial / final temperature space fit to the initial signal rise and final signal level of the data presented in Figure 2.9.3 and Figure 2.9.4, A,B and C corresponding to repeats 1, 2 and 3. Yellow cells indicate temperature pairs which reproduce the behaviour of the experimental data to within 1% of the experimental values.

With thermal radiation from the nozzle being highlighted as the most likely source of heating near the surface it makes sense to consider a worst case scenario for how large the difference between the measured and actual temperature of the surface could be. This assessment will be made assuming the heater is off, and the temperature sensor is reading 6K. The thermal sensor is in good thermal contact

with the copper sample holder which may be taken to be at 6K, any difference in temperature must therefore occur over the length of the sapphire. While having a profile akin to a top hat in reality, the sapphire may be modelled as a cylinder with cross sectional area equivalent to the average cross sectional area of the real sapphire. This gives a cylinder of cross sectional area 25mm^2, 7.1mm in length. While the nozzle is the hottest thing inside the bore it is not the warmest object in line of sight of the surface, this would be the vacuum flange of the magnet at ~300K, which occupies 17% of the field of view (F.O.V) from the deposition surface. The following worst case-scenario estimate for the temperature difference considers both the barrel and upper face of the sapphire to be exposed to thermal radiation from the flange (at 300K) and the infrared shroud. The infrared shroud is actively cooled and has been seen to harbour visible (mm thick) chunks of argon ice indefinitely. Within the vacuum conditions of the bore argon ice has not been observed to persist at the sensor indefinitely beyond 30K, the temperature of the shroud (and therefore the remaining 83% of the F.O.V of the sapphire) will be set at this point for the purpose of the model.

The Steffan-Boltzmann law[16] for thermal radiation states:

$$q_{in} = A\varepsilon\sigma\left(T_{Surr}^4 - T_{obj}^4\right) \quad \text{(Eq. 2.9.1)}$$

Where q_{in} is the thermal energy absorbed by the object in Watts, A is the absorbing surface area of the object, ε is the emissivity of the absorbing object, σ is the Steffan-Boltzmann constant, T_{Surr} is the temperature of the surroundings and T_{obj} is the temperature of the absorbing object.

For the purpose of a worst-case approximation the sapphire will be treated as a black body with an emissivity of 1. The temperature of the sapphire will be set at 6K, the temperature at the interface between the sapphire and the copper support. To account for the two different surrounding temperatures (Eq. 2.9.1) is further modified to:

$$q_{in} = A\varepsilon\sigma\left(0.17T_{flange}^4 + 0.83T_{shroud}^4 - T_{obj}^4\right) \quad \text{(Eq. 2.9.2)}$$

Where T_{flange} is the vacuum flange temperature (300K) and T_{shroud} is the temperature of the IR shroud (30K). Substituting the appropriate values into (Eq. 2.9.2) gives an absorbed wattage of 9mW. For the temperature of the surface to reach a steady state the value of q_{in} must be matched in magnitude by the heat flow away from the absorbing surface. Taking the temperature of the absorbing surface as T_{Hot} located at the top surface of the sapphire and the temperature at the interface between the sapphire and the copper support as T_{cold} then the heat conduction through the sapphire is given by:

$$q_{out} = kA_C\frac{(T_{Hot} - T_{Cold})}{L} \quad \text{(Eq. 2.9.3)}$$

Where k is the thermal conductivity of the sapphire, A_C is the cross-sectional area of the sapphire and L is the length of the sapphire. Setting $q_{in} = q_{out}$ and rearranging for T_{Hot} gives:

$$T_{Hot} = T_{cold} + \frac{Lq_{in}}{kA_C} \quad \text{(Eq. 2.9.4)}$$

Which, after substituting in the appropriate values gives a steady-state hot side temperature of 6.02K. This is markedly lower than the ~8K shown by Figure 2.9.5 to be the required final temperature for a difference in measured and actual temperature to explain the discrepancy between model and experiment in Figure 2.9.3 and Figure 2.9.4, let alone the ~10K increase that would be required to take the measured initial temperature from 20 to the required ~30K.

An additional potential source of heating could be the coil, which is expected to heat due to electrical resistance during transmission. However, even under the conservative estimate that the 50 Ohm resistance of the coil is purely real, the average power dissipation of the coil during measurement is a mere 5.5mW. Smaller than the 9mW absorbed by the sample due to hot surfaces before even accounting for inefficiencies in transmission of the coil heat to the surface. Overall, while a temperature difference could explain the discrepancies seen, the data does not support a temperature difference as the source of the discrepancy.

This leaves the possibility of a non-converting species being present to be investigated. Setting S_{max} as the maxima in signal (Figure 2.9.4) where no nuclear spin conversion has occurred, and S_{min} as the minimum in signal following complete nuclear spin conversion, both may be broken down into components:

$$S_{max} = s_1 + s_2 \quad \text{(Eq. 2.9.5)}$$

$$S_{min} = C_{20K}^{6K} s_1 + s_2 \quad \text{(Eq. 2.9.6)}$$

Where s_1 is the component of the signal arising from the converting species, s_2 is the component arising from the non-converting species and C_{6K}^{20K} is a coefficient accounting for nuclear spin conversion from 20K to 6K. s_2 may be further broken down as equivalent to some proportion of s_1:

$$s_2 = F s_1 \quad \text{(Eq. 2.9.7)}$$

Where F is the constant of proportionality. Substituting (Eq. 2.9.7) into (Eq. 2.9.5) & (Eq. 2.9.6), then dividing (Eq. 2.9.5) by (Eq. 2.9.6) gives:

$$\frac{S_{max}}{S_{min}} = \frac{1 + F}{C_{20K}^{6K} + F} \quad \text{(Eq. 2.9.8)}$$

Which after significant rearrangement provides:

$$F = \frac{\frac{S_i}{S_f} C_{20K}^{6K} - 1}{1 - \frac{S_i}{S_f}} \quad \text{(Eq. 2.9.9)}$$

Taking the appropriate points from Figure 2.9.4, and setting $C_{20K}^{6K} \cong 0.12$ in accordance with rotational energy calculations gives the three values for F presented in Table 2.9.1 below.

Table 2.9.1: Values of F for the three cooling experiments presented in Figure 2.9.4

	Rep 1	Rep 2	Rep 3
F (2 d.p.)	0.25	0.18	0.15

With the average value of F over all three repeats being 0.20 (2 d.p.). This implies that on average the signal from the non-converting species is 20% of the maximum signal from the converting species at a rotational temperature of 20K. Given each sample was used in both heating and cooling experiments, it stands to reason that the same values of F should emerge when comparing points at equivalent temperatures in the heating data.

Signal Level Analysis: Heating Data:

Said heating data, alongside the predicted minimum signal level due to thermalisation of the Zeeman energy is presented in Figure 2.9.6. Only a single data point drops below the predicted minimum, with low signal to noise in the data being readily apparent. As was discussed during first presentation, the minimum seen in the signal in Figure 2.9.6 is likely not to be the true minimum that would be expected if the Zeeman energies had equilibrated but no NSC had occurred, as NSC appears to occur on a similar timescale to T1 in this case. The samples used for repeats 1, 2 and 3 in Figure 2.9.6 are the same samples for repeats 1,2 and 3 in Figure 2.9.3. The temperature observations of the previous subsection therefore also apply here, the data does not support there being a significant difference in measured and observed temperatures. If the minima seen in Figure 2.9.6 is the true minima, the only remaining explanation for a difference in observed and predicted minimum signal would be a poor choice of model (the calculation again assuming an ensemble of non-interacting spin half).

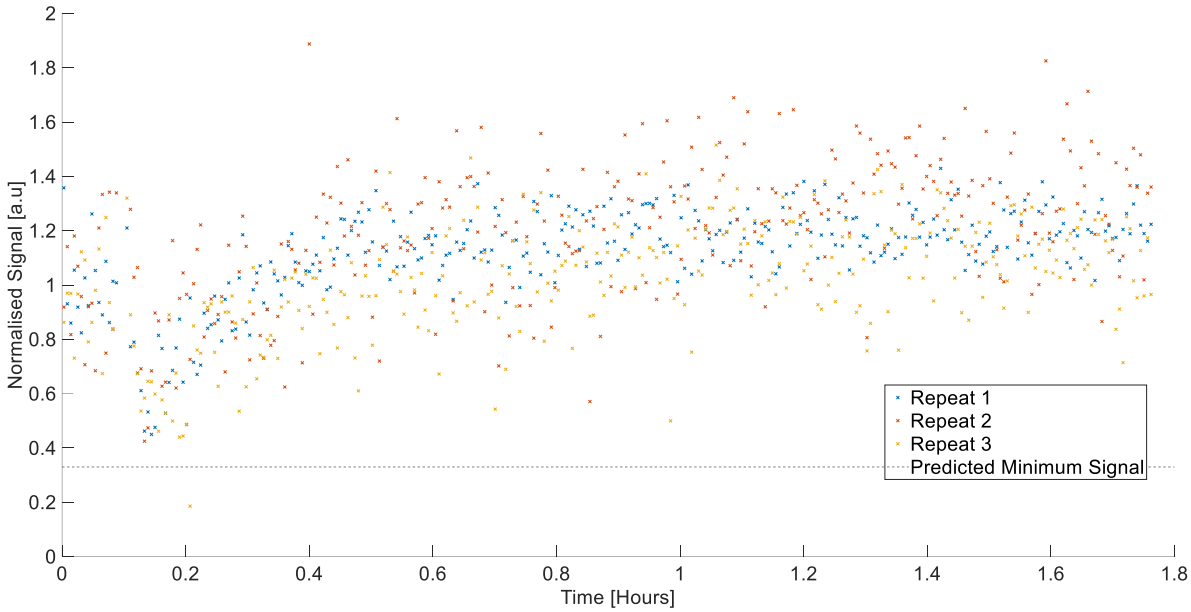

Figure 2.9.6: Plot of Normalised Signal versus time for the 3 6.6 to 20K experiments, high signal data points immediately following the temperature jump are excluded for readability. The black dashed line indicates the minimum signal level we expect following the jump based on calculations of the Zeeman populations in the sample.

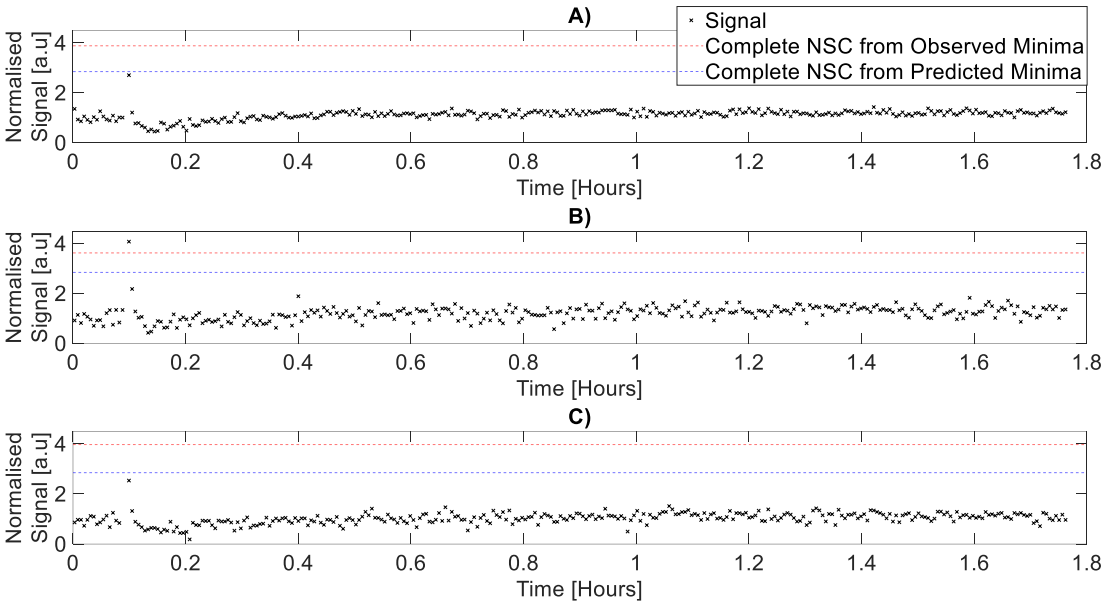

Figure 2.9.7: Normalised signal versus time plots for the three heating experiment repeats. Black X's represent signal. The red dashed line represents the predicted final signal level using the minimum in the data as the initial signal pre-NSC. The blue dashed line is the same calculation, but using the predicted minimum signal calculated for Figure 2.9.6 as the start point for NSC.

With regards to the final signal level, Figure 2.9.7 presents all three repeats of the heating data separately, with the highest signal level points excluded for readability. Two predicted signal levels are included in Figure 2.9.7, the first (dashed red lines) are calculated using the observed minima in the data, the second (blue dashed lines) are calculated using the predicted minima from Figure 2.9.6. In all three cases (A through C) the signal calculated from the predicted minima is a better match to the data, but neither model accurately matches the experimental data. The fact that the difference in this case is an overestimation as compared to the underestimation

present for the cooling data would align with a non-converting species. In the heating data the non-converting species would produce decreased signal following the signal, which would not increase as NSC progressed.

Assessing the proportion of non-converting species required to produce the results seen in Figure 2.9.6 employs the same mathematics presented in (Eq. 2.9.9) with C_{20K}^{6K} being replaced with $C_{6K}^{20K} \cong 8.3$. S_{max} in this case is the maximum signal at the end of the experiment at 20K, while S_{min} would be the minima. For purpose of discussion this will be set to the predicted minima calculated for Figure 2.9.6. Substituting in the appropriate values from Figure 2.9.7 gives the values of F presented in Table 2.9.2.

Table 2.9.2: Values of F for the three heating experiments shown in Figure 2.9.7

	Rep 1	Rep 2	Rep 3
F (2 d.p.)	0.21	0.17	0.25

The overall mean of the values presented Table 2.9.2: Values of F for the three heating experiments shown in Figure 2.9.7 is 0.21, comparable to the 0.20 seen for the cooling data.

Signal Level Analysis: Conclusions:

Comparison of the signal levels at important times in both heating and cooling measurements reveals that the experimental data does not conform to expectations from theory. Temperature differences have been excluded as a possible source of discrepancy, and the presence of a non-converting hydrogen species which does not undergo NSC is presented as a possible explanation for the difference between theoretical and observed final signal levels. The required signal from non-converting species as a proportion of the maximum signal from the converting species to explain the discrepancy in final signal level is ~20%. Calculation of the proportion of non-converting species assumes full Zeeman-energy thermalisation before NSC begins, and does not inherently explain discrepancies in the observed signal immediately before and after a temperature jump. The only explanation presented here is an as-yet unidentified problem in the choice of model.

Section 2.10 Fitting NSC Curves:

Overview:

To extract rate constants from our NSC data we first need to fit the decay/growth curves to appropriate rate equations. In this section we first introduce the chosen equations before presenting the fits and extracting the relevant rate constants.

Cooling Experiment Fitting:

To choose appropriate fitting equations for the data we must first relate our NMR signal to the ortho-content of our sample. Following the derivation laid out in by *Mamone et al*[11] we define the instantaneous ortho-fraction (the proportion of water molecules in the sample that have ortho character) at given time t as $\phi(t)$. The instantaneous para fraction may then be deduced as $1-\phi$. The relation of the NMR signal I_{NMR} to $\phi(t)$ is given by:

$$I_{NMR}(t,T) = C(T)T^{-1}\phi(t) \qquad \text{(Eq. 2.10.1)}$$

Where $C(T)$ describes the variance in instrument sensitivity with temperature and the T^{-1} factor arises from Curie's law of paramagnetism. With the assumption that the decay takes place at constant temperature, we may normalise (Eq. 2.10.1) to its value at the start of the decay $I_{NMR}(0,T)$, giving the normalised signal $S(t,T)$.

$$S(t,T) = \frac{I_{NMR}(t,T)}{I_{NMR}(0,T)} = \frac{C(T)T^{-1}\phi(t)}{C(T)T^{-1}\phi(0)} = \frac{\phi(t)}{\phi(0)} \qquad \text{(Eq. 2.10.2)}$$

We consider two distinct fit types to our experimental data. We first introduce the underlying mathematics for these fits before moving on to apply them.

First order fits:

In their work observing NSC in H_2O@Ar using infrared spectroscopy Pardanaud[5] identified two competing phenomena contributing to NSC. While they suggested that one of these processes may be due to intermolecular interactions, they found a single exponential fit based on first order reaction kinetics to be sufficient for the extraction of decay constants. The differential form of the rate equation which gives rise to this type of fit is[7]:

$$\frac{dx(t)}{dt} = -k_1 t \qquad \text{(Eq. 2.10.3)}$$

Where $x(t)$ is the concentration / quantity of interest and k_1 the first order rate constant for the reaction. Solutions to (Eq. 2.10.3) between $t=0$ and t take the form:

$$x(t) = x(0)e^{(-k_1 t)} \qquad \text{(Eq. 2.10.4)}$$

Where $x(0)$ is the maximum in $x(t)$ at $t=0$. We assign $x(t) = \Delta\phi(t)$ where $\Delta\phi(t) = \phi(t) - \phi_{eq}$ and ϕ_{eq} is the fraction of the population in the ortho state at the thermal equilibrium temperature T. (Eq. 2.10.4) then becomes:

$$\Delta\phi(t) = \left(\phi(0) - \phi_{eq}\right)e^{(-k_1 t)} \qquad \text{(Eq. 2.10.5)}$$

Expanding the left-hand side, recasting and finally normalising to $\phi(0)$ gives (Eq. 2.10.6), our first order equation to fit the signal $S(t,T)$.

$$\frac{\phi(t)}{\phi(0)} = \left(1 - \frac{\phi_{eq}}{\phi(0)}\right) e^{(-k_1 t)} + \frac{\phi_{eq}}{\phi(0)} = S(t,T) \quad \text{(Eq. 2.10.6)}$$

The first order rate equation describes a process that depends only on the concentration of ortho-water present. Each water molecule is independent of its peers, converting through some interaction with its environment at a rate which is insensitive to the presence of other ortho water molecules.

Second order fits:

The idea of an intermolecular interaction between H_2O molecules is also presented by Mamone *et al*[11] when discussing endohedral water in C_{60} ($H2O@C_{60}$). While Pardanaud[5] fits his NSC curves with a single exponential, Mamone *et al* opt to fit a rate equation that is second order in $\Delta\phi(t)$, citing observations of similar second order behaviour for hydrogen NSC in solid H_2. The proposed differential form of the equation is:

$$\frac{d\Delta\phi(t)}{dt} = -k_2 \Delta\phi(t)^2 \quad \text{(Eq. 2.10.7)}$$

Solutions to (Eq. 2.10.7) take the form:

$$\frac{1}{\Delta\phi(t)} = \frac{1}{\Delta\phi(0)} + k_2 t \quad \text{(Eq. 2.10.8)}$$

This may be related to $S(t,T)$ through the following steps:

$$\Delta\phi(0) = \Delta\phi(t) + \Delta\phi(t)\Delta\phi(0)k_2 t \quad \text{(Eq. 2.10.9)}$$

$$\Delta\phi(0) = \Delta\phi(t)(1 + \Delta\phi(0)k_2 t) \quad \text{(Eq. 2.10.10)}$$

$$\Delta\phi(t) = \frac{\Delta\phi(0)}{(1+\Delta\phi(0)k_2 t)} \quad \text{(Eq. 2.10.11)}$$

$$\frac{1}{\phi(0)}\left(\phi(t) - \phi_{eq}\right) = \frac{1}{\phi(0)}\left(\frac{\Delta\phi(0)}{(1+\Delta\phi(0)k_2 t)}\right) \quad \text{(Eq. 2.10.12)}$$

$$S(T,t) - \frac{\phi_{eq}}{\phi(0)} = \frac{\Delta\phi(0)}{\phi(0)(1+\Delta\phi(0)k_2 t)} \quad \text{(Eq. 2.10.13)}$$

$$S(T,t) = \frac{A}{1+\kappa t} + B \quad \text{(Eq. 2.10.14)}$$

$$with: A = \frac{\Delta\phi(0)}{\phi(0)}, B = \frac{\phi_{eq}}{\phi(0)},\ \kappa = \Delta\phi(0)k_2 \ and\ A + B = 1$$

An advantage of (Eq. 2.10.14) is that it may be recast into the form of a straight line intercepting the vertical axis at 1:

$$\frac{A}{S(T,t)-B} = \kappa t + 1 \quad \text{(Eq. 2.10.15)}$$

The rate constant k_2 being extractable from the gradient κ as $k_2 = \frac{\kappa}{A\phi(0)}$. As was initially mentioned, the proposed mechanism linked to this rate equation is an interaction between water molecules in neighbouring C_{60} cages, assisted by a spin diffusion process allowing neighbouring water molecules to exchange identities. The microscopic mechanism for the NSC is less clear, while the presence of a magnetic dipole on ortho-water allows for dipole-dipole coupling between molecules, the size of the cages and therefore separation between said molecules would render this coupling weak.

Fits to Experimental Data:

Figure 2.10.1 displays decay curves, fits and residuals for all three 20 to 6.6K experiments. Considering the decay curve plots (A1/B1/C1), to the eye, the green fit line corresponding to second order fitting appears to be a better match to the data in all three cases. The red lines corresponding to first order fitting appear to alternate between under and overestimating the experimental data. This is more apparent in the residual plots for the first order fits (A2/B2/C2), in all three experiments we see the same pattern of initial underestimation by the model, overestimation around the one-hour mark, underestimation again between the 2 and 4 hour marks and overestimation again from the 4 hour mark to the end of the experiment. In contrast, the residuals from the second order fits (A3/B3/C3) only exhibit underestimation at the beginning of the experiment, the residuals being dispersed randomly about zero from the 1 hour mark onwards.

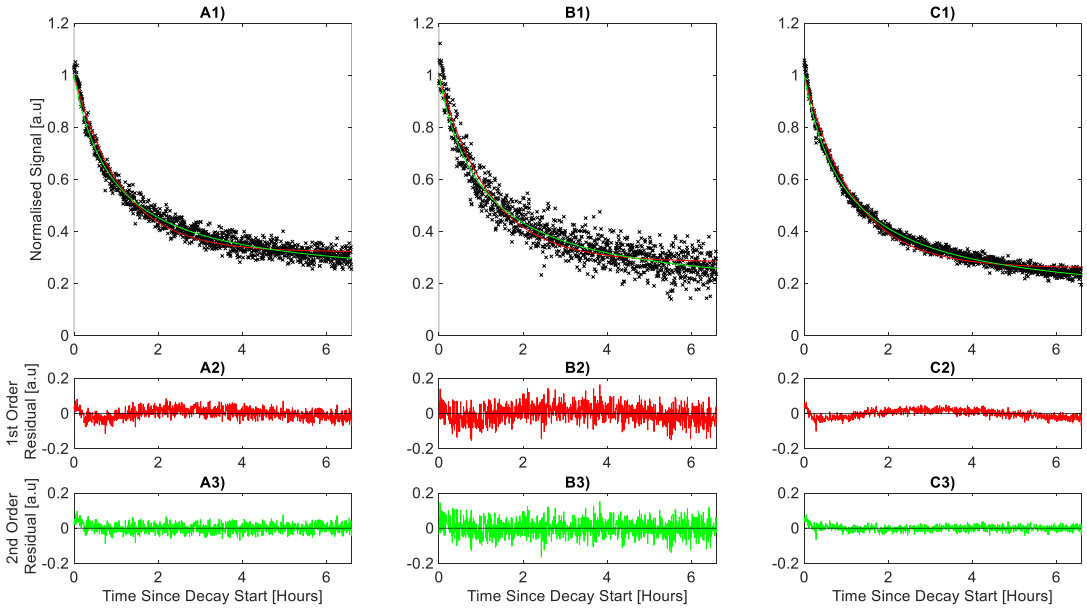

Figure 2.10.1: **A1/B1/C1)** Fitted decay curves for all three (**A/B/C**) 20 to 6.6K experiments. Black x's represent experimental data, red lines are first order fits to the data, green lines are second order fits to the data. **A2/B2/C2)** Residuals (data-fit) for first order fits to the data. **A3/B3/C3)** Residuals (data-fit) for second order fits to the data.

One point of note is that the pattern of mismatch observed Figure 2.10.1-A2/B2/C2 is a qualitative match to those observed by Pardanaud[5] (for example figure 5, chapter 4 of their thesis), albeit on a longer timescale. With the data appearing to behave

similarly, it is not unreasonable to question whether a second order fit would have performed better when applied to Pardanaud's data.

Additional insights may be gained by considering linearised plots of the data presented in Figure 2.10.1. Linearisation to the first order fit requires subtraction of the predicted asymptotic level and taking the natural logarithm. This presents an issue in the case of overestimation, as the result will be complex (natural log of a negative number). Fits to the first order in the following figure omit these values. Second order linearisation is achieved via (Eq. 2.10.15).

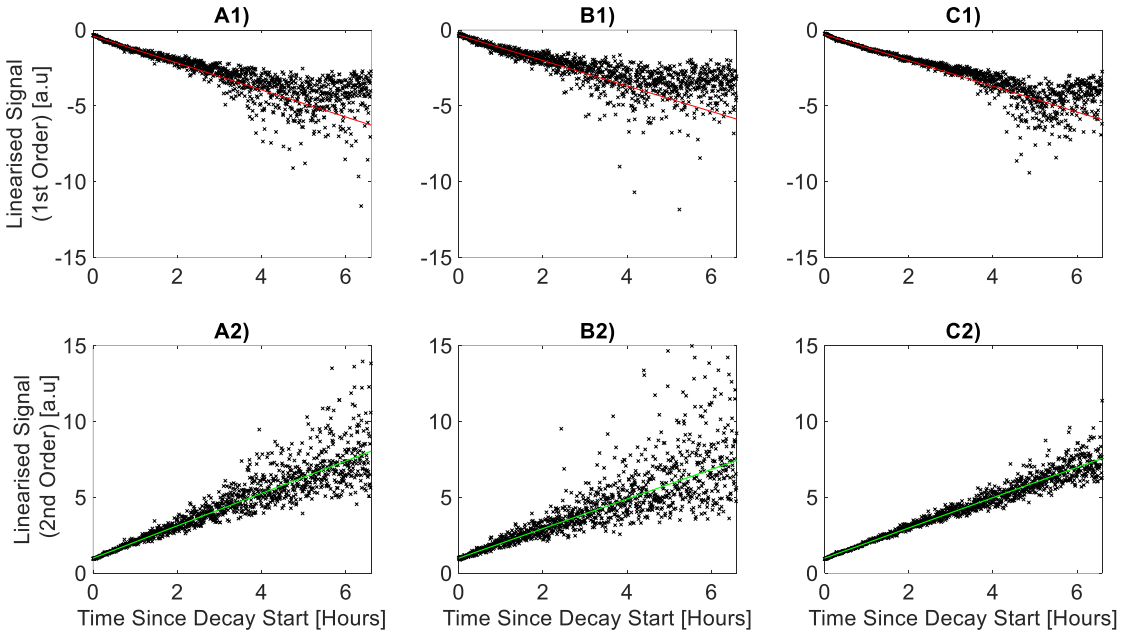

Figure 2.10.2: Linearised plots of the experimental decays plotted in Figure 2.10.1. Plot label letter (A, B, C) corresponds to experiment inline with the parent figure. Plots labelled 1 are linearised to first order fits. Plots labelled 2 are linearised to second order fits. Data points are represented by black x's. Coloured lines are the linearised fits to the data, red for first order, green for second.

Considering first order fits (Figure 2.10.2 A1, B1 and C1) there is clear deviation from a straight line the experimental data past the 3 hour mark in all 3 cases. This is correspondent with the observed overestimation of the asymptotic level in the natural form of the fits seen in Figure 2.10.1 A1 B1 and C1. The initial misfit seen in the residuals in Figure 2.10.1 A2, B2 and C2 is not distinguishable in the linearised fit. Agreement between linearised fit and data is clearly better for second order fits (Figure 2.10.2 A2, B2 and C2) where points appear evenly spaced either side of the fit line for its full duration, with the exception that spread increases at long times when signal is at its lowest.

For first order fits, the average rate constant k_1 over all three experiments was 2.388×10^{-4} s^{-1}. This corresponds to "conversion time" at 6.6K of ~69 minutes. How well this value aligns with the existing literature depends on which end of our 0.5-1% H_2O@Ar concentration range we believe our sample lie. If we believe we are closer to 1% the conversion time with conditions most closely matching our own reported by Pardanaud was 260 minutes (averaging over times reported for all spectral peaks, for a concentration of 1% H_2O@Ar at 4.2K. This is notably longer than our

observed time. If we believe our concentration is closer to 0.5% then we may expect our time to fall between 429±40 and 293±30 minutes, Pardanaud's measured times for 0.5% H_2O@Ar at 4.2 and 8K respectively, both of these being longer than our reported value. If our concentration is indeed closer to 1%, the difference may solely be due to temperature, as the temperature dependence of the conversion rate may increase with increased concentration. If the concentration is close to 0.5% temperature differences between our measurement and Pardanaud's cannot explain the difference in conversion rate, the trend in conversion rate between 4.2 and 8K should be monotonic and our value at 6.6K should therefore lie between them. In all likelihood we are at some concentration between 0.5 and 1% which varies between samples due to varied nozzle temperature, whether this concentration difference alone is enough to explain the difference between our observed first order NSC rate and Pardanaud's is unclear.

Extraction of the second order rate constant requires accurate identification of $\phi(0)$, our normalisation method makes this difficult to extract from the experimental data. As such we estimate the value of $\phi(0)$ by calculation of the thermal-equilibrium rotational energy distribution for H_2O at 20K, this gives us a value of 0.66. The extracted rate constant k_2 averaged over all three experiments is 505×10^{-6} s^{-1}. While the two systems are quite different in terms of the local environment the water molecule perceives, this value is on the same order of magnitude as the rate constants observed by Mamone *et al*[11] for H_2O@C60 at 5K.

It is difficult to comment on the underlying mechanism for conversion from this data alone. The second order fits are undeniably a closer match to the data than the first order fits, supporting a bimolecular mechanism involving two neighbouring H_2O molecules in the argon lattice. Concentration dependent studies are required to verify whether this assignment holds.

Heating Experiment Fitting:

As was the case for the cooling experiments we must first normalise our data in a manner that directly relates the ortho content of the sample to the observed signal. As was noted in the initial analysis section, the minimum observed in the data for heating experiments is unlikely to be a "true minimum" making $I_{NMR}(0,T)$ a poor choice of normalisation factor. Instead, we choose to normalise to the plateau in the data at the end of the conversion, which should be equivalent to $I_{NMR}(\infty,T)$ or simply the equilibrium signal level. Our observed signal is therefore:

$$G(t,T) = \frac{I_{NMR}(t,T)}{I_{NMR}(\infty,T)} = \frac{C(T)T^{-1}\phi(t)}{C(T)T^{-1}\phi_{eq}} = \frac{\phi(t)}{\phi_{eq}} \qquad \text{(Eq. 2.10.16)}$$

Again, as was noted in initial analysis (Section 2.9) the rate of conversion in experiments is much faster than in cooling experiments, with the signal plateauing by the one hour mark. Qualitatively, the shape of the growth curve is very similar to those for measurements of the longitudinal spin relaxation time (T1). Following this we will try fitting a first order rate equation of a similar form. Introducing the difference between the current and initial signal level as $\Delta\phi_0(t) = \phi(t) - \phi(0)$, we may write the differential form of the rate equation:

$$\frac{d\Delta\phi_0(t)}{dt} = -g_1[\Delta\phi_0(t) - \Delta\phi_0(\infty)] \quad \text{(Eq. 2.10.17)}$$

Solutions to this may be obtained through the following steps:

$$\int \frac{1}{[\Delta\phi_0(t) - \Delta\phi_0(\infty)]} d\Delta\phi_0(t) = -\int g_1 dt \quad \text{(Eq. 2.10.18)}$$

$$\ln\big(\Delta\phi_0(t) - \Delta\phi_0(\infty)\big) = -g_1 t + C \quad \text{(Eq. 2.10.19)}$$

$$\text{For t} = 0: \qquad \Delta\phi_0(t) = 0,\ \ln\big(-\Delta\phi_0(\infty)\big) = C \quad \text{(Eq. 2.10.20)}$$

$$\ln\big(\Delta\phi_0(t) - \Delta\phi_0(\infty)\big) = -g_1 t + \ln\big(-\Delta\phi_0(\infty)\big) \quad \text{(Eq. 2.10.21)}$$

$$\frac{\Delta\phi_0(\infty) - \Delta\phi_0(t)}{\Delta\phi_0(\infty)} = \exp(-g_1 t) \quad \text{(Eq. 2.10.22)}$$

$$\Delta\phi_0(\infty)[1 - \exp(-g_1 t)] = \Delta\phi_0(t) \quad \text{(Eq. 2.10.23)}$$

$$\phi(t) = \Big(\phi_{eq} - \phi(0)\Big)[1 - \exp(-g_1 t)] + \phi(0) \quad \text{(Eq. 2.10.24)}$$

$$\frac{\phi(t)}{\phi_{eq}} = \left(1 - \frac{\phi(0)}{\phi_{eq}}\right)[1 - \exp(-g_1 t)] + \frac{\phi(0)}{\phi_{eq}} \quad \text{(Eq. 2.10.25)}$$

$$G(t,T) = D[1 - \exp(-g_1 t)] + (1 - D),\ with: D = \left(1 - \frac{\phi(0)}{\phi_{eq}}\right) \quad \text{(Eq. 2.10.26)}$$

Figure 2.10.3 A1/B1/C1 (overleaf) displays experimental data for all three heating experiments, along with fits to the data of the form given by equation (Eq. 2.10.26). The residuals for each experiment are shown in Figure 2.10.3 A2/B2/C2 (overleaf).

The red lines in Figure 2.10.3 A1/B1/C1 appear to provide a good fit to the data, further to this the residuals (A2/B2/C2) for all three experiments appear to oscillate randomly about zero. However, the signal to noise of the signal in the experiments represented by B1 and C1 is observable worse than that in A1, with A1 being the only figure presenting a clearly identifiable initial growth region. The linearised form of (Eq. 2.10.26) is:

$$\ln\left(\frac{1 - G(t,T)}{D}\right) = -g_1 t \quad \text{(Eq. 2.10.27)}$$

This is inherently complex for values $G(t,T) > 1$, which the plateau in the data is normalised to. As a result, only the data plotted in Figure 2.10.3 A1 may provide any useful insight in linearised form, as divergence from linear behaviour is expected outside of the growth region. The corresponding plot is given as Figure 2.10.4 overleaf.

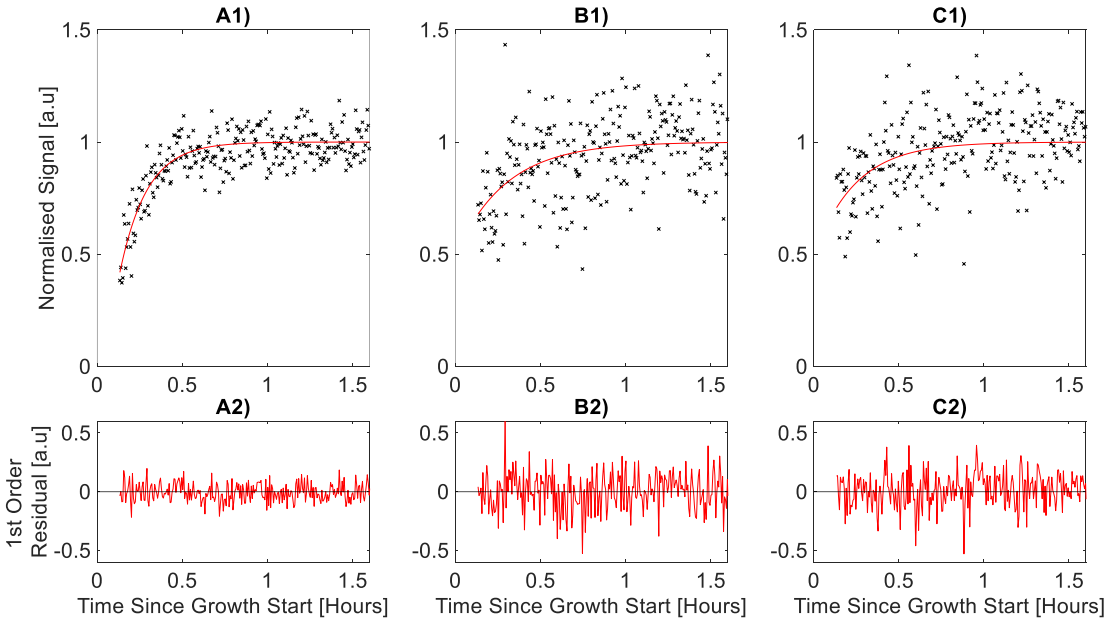

Figure 2.10.3: **A1/B1/C1**: Plots of normalised signal versus time for all three heating experiments. Black x's represent signal, red lines are fits to the data of the form of equation (Eq. 2.10.26). The start of growth is determined as the point the temperature of the sample stabilised at 20K. The initial part of the growth was not capturable. **A2/B2/C2**: Residuals data-fit for all heating experiments.

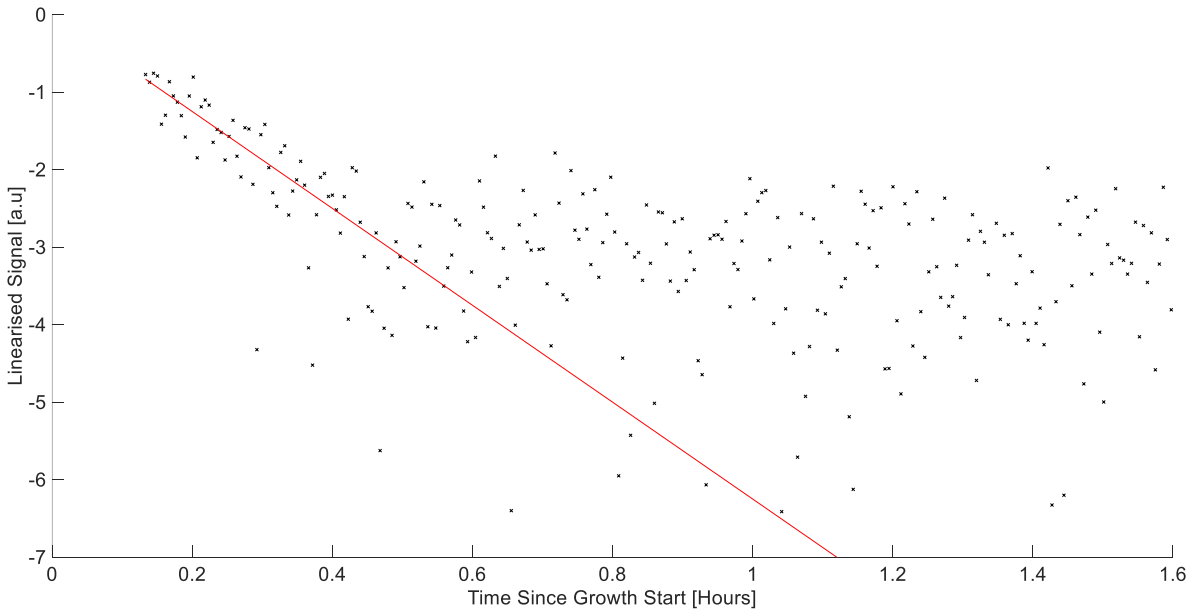

Figure 2.10.4: Linearised form of fit and data plotted in Figure 2.10.3 A1. Experimental data is represented by black x's, while the fit is shown as a red line.

There is clear agreement between the linearised fit and experimental data in Figure 2.10.4 up until a time of roughly 0.5 hours, which is where the plateau begins in Figure 2.10.3 A1. Beyond this point there is the expected divergence from the straight line. The plotted points represent only those where the experimental value was less than the asymptote of the fit, as larger values (which would result in complex results) are not shown.

Table 2.10.1: Extracted first order rate constants for NSC curves captured at 20K

	Rep 1	Rep 2	Rep 3	Mean
Rate constant [$1x10^{-6}$ s^{-1}]	1700	900	1200	1266

Table 2.10.1 displays the resulting rate constants. Taking the average over all three experiments gives a rate constant of: $1266x10^{-6}$ s^{-1}, equivalent to a conversion time of 13 minutes (nearest minute). This is much more rapid than the 69 minute conversion time observed for the first order fit to the cooling experiment data. The fact that a single order mechanism is sufficient to fit the data would suggest that NSC at 20K occurs via a monomolecular process but, it is important to note that the data itself is quite noisy making assignment of any fit to the data difficult, only one of the reported rate constants (Rep 3) is within close proximity to the mean. Furthermore, a second order fit has not been attempted, both due to the lack of evidence for such fits in literature and the fact that the poor definition of the signal at t=0 would make such fitting difficult at best. It is not possible to make detailed comment on the microscopic mechanism for this conversion from the available data, though it is not unreasonable to suggest that the higher temperature may open additional pathways to conversion via greater availability of rotational states.

Conclusions:

Cooling experiment data was fit to models following both first and second order reaction kinetics. Second order kinetics were found to be a better fit to the experimental data, suggesting that NSC at 6.6K proceeds via a bimolecular mechanism involving two ortho water molecules. In the case of first order fits the NMR method produced rate constants on a similar order of magnitude to those observed in a comparable H_2O@Ar study using the more establish infrared spectroscopy method. Rate constants for second order fits were of comparable order to those presented in an NMR study on the related $H_2O@C_{60}$ system for similar temperatures.

Heating experiment data was fit to a single model following first order kinetics. The first order model was found to provide a suitable fit to the data suggesting that NSC at 20K proceeds following a monomolecular mechanism. It is hypothesised that the higher temperature allows individual ortho water molecules to convert independently due to greater availability of rotational states.

Extracted rate constants for both experiment types are summarised in Table 2.10.2.

Table 2.10.2: Average first and second order rate constants from fits to NSC curves captured at 6.6 and 20K.

Conversion Temperature [K]	First Order Rate Constant [10^{-6} s^{-1}]	Second Order Rate Constant [10^{-6} s^{-1}]
6.6	239	505
20	1300	N/A

Section 2.11: Next Steps:

Two of the greatest obstacles faced in trying to obtain experimental time constants for NSC in H_2O@Ar were coil arcing and low signal to noise. Solving the first issue is a matter of further iteration and development of the NMR probe and matrix deposition technique. Improvements to the reproducibility of the matrix deposition as well as control over the concentration of water in the final sample would also open the doors to concentration studies with H_2O@Ar making determination of which (first or second order) mechanism is primarily responsible for NSC easier. Potential ways of achieving this are discussed in Chapter 4.

With regards to improving signal to noise there are multiple avenues to explore. The most straightforward methods are an increase in sample size or field strength, both providing a greater difference in the number of spins in their up vs down configuration at thermal equilibrium and therefore more signal. The benefits of these techniques are limited by size constraints within the bore, the maximum field possible with the current magnet and the ability of the probe to be matched to higher frequencies. Without significant modification to the apparatus any increase in signal gained from these methods is likely to be minimal. An alternative option is the deployment of so called “Hyperpolarisation” methods, in the next chapter the concept of hyperpolarised deposition is introduced and discussed, leading in to the development and testing of an apparatus for cryo-deposition and NMR measurement of a hyperpolarised molecular beam of methane.

Chapter 3: Towards Hyperpolarised Deposition with Methane:

Section 3.1: Hyperpolarisation:

Overview of hyperpolarisation methods:

The issue of low sensitivity in NMR experiments is ubiquitous, the two potential solutions to the issue being increasing detector sensitivity or increasing the amount of signal present to be detected. The development of hyperpolarisation methods occupies a major part of this second pathway. The NMR signal is directly proportional to the spin-polarisation in the sample, in a typical NMR experiment this polarisation is the thermal equilibrium spin-polarisation for the given temperature and magnetic field strength. Hyperpolarisation then, refers to measurement of a sample with spin-polarisation greater than would be expected at thermal equilibrium for the given temperature and detecting magnetic field strength. Multiple methods for enhancing the polarisation of a given NMR sample have been developed (for recent reviews see [25, 26]). Perhaps the simplest hyperpolarisation technique is so called "Brute-Force" hyperpolarisation[25, 26]. This refers to increasing polarisation by first pre-polarising the sample at lower temperature, or higher field than at the time of detection. Field based methods may involve physically moving the sample from a stronger pre-polarising field to the field where detection is to be undertaken, while temperature based methods may involve pre-cooling the sample then rapidly dissolving it in a solvent at the desired measurement temperature (a method that has been employed[12] to measure nuclear spin conversion in $H_2O@C_{60}$ at room temperature).

More complex methods involve transfer of polarisation from an external source. In Para-Hydrogen Induced Polarisation (PHIP) and Signal Amplification by Reversible Exchange (SABRE) the source molecule is para-hydrogen. Both of these are reactive methods, PHIP employing spin-conserved hydrogenation of an un-hydrogenated target[27] while SABRE employs a catalyst to achieve polarisation transfer without target hydrogenation[28]. Dynamic Nuclear Polarisation (DNP) methods use the (comparatively) high thermal equilibrium polarisation of electron spins as their polarisation source. Various DNP methods exist and can be separated by the phase of matter over which they operate, the most well explored solid state method being magic-angle-spinning (MAS) DNP. The source of electron spin in these experiments is a "stable paramagnetic polarising agent"[29] typically a radical, applied as a dopant to the sample.

Applicability to MIS NSC Measurements:

The issue with spin-transfer methods for the study of NSC in cryo-matrix trapped H_2O is that they inherently require the presence of other molecules. Among the benefits of the inert cryo-matrix based method is the ability to isolate individual water molecules in their (close to[13]) freely rotating state, absent of any spin-containing contaminants that could influence NSC (e.g. O_2). The introduction of an external source of spin to the matrix flies directly in the face of this. The thermal brute force method is also not applicable in this case, temperature is already the independent variable of the experiment, while the experimental evidence presented in Section 2.9 shows that the enhancement in Zeeman polarisation achieved at colder

temperatures can be directly counteracted by the decrease in overall polarisation due to NSC. The remaining brute-force option of increasing the field strength has been discussed earlier in this document. While there is no theoretical reason it would not be a benefit, increasing the field strength (and therefore resonant frequency) would require significant probe redesign. Further to this, increasing the field strength to a degree that would provide significant signal enhancement would likely require a completely new magnet and is beyond the scope of this work.

A potential solution lies in what [25] refers to as “Spin Sorting Phenomena” which allow for filtering of molecules by spin state. Among the viable methods, the one which the Swansea Surface Dynamics (SUDY) research group specialises is Stern-Gerlach (named for the scientists who first deployed the method[30, 31]) magnetic separation.

Magnetically focused polarised molecular beams:

The physics underpinning the magnetic separation and focussing of molecular beams of neutral, spin containing molecules is covered in detail in the latter part of Section 3.4. In brief, the technique employs a gradient magnetic field to separate molecules with differing internal magnetic moments. For neutral molecules these moments may arise from nuclear spin, electron spin (as is the case for O_2) or molecular rotation. A molecular beam is allowed to propagate through a magnetic field gradient, the trajectory of molecules with an internal magnetic moment is altered by interaction with the magnetic field, and the components with differing moments end up travelling in different directions. The group employs a hexapole gradient field, the hexapole magnetic lenses (henceforth “hexapoles”) which produce the field being based on designs originally intended for working with ^3He[32]. To a first approximation the field gradient within the hexapoles is purely radial, with zero field at the centre and high field at the edges. This causes the change in trajectory a molecule with nonzero magnetic moment experiences to always be either towards or away from the centre of the hexapole, allowing the whole assembly to behave like a magnetic lens.

For a molecular beam, emitted from a negligibly small source with well-defined velocity and magnetic moment, it would be possible to construct a hexapole system that could focus the beam to a point along the beam axis. The deflections of the trajectories of particles passing through the hexapole are increased by field gradient strength and the time spent in the hexapole. In a molecular beam with components with differing magnetic moments those of the desired moment may be collected by designing a hexapole which sends that specific moment in a desirable direction and collecting the molecules sufficiently far from the exit of the hexapole that molecules of differing moment have diverged away.

In the absence of electron spin, the behaviour of a molecule within the hexapole can be predicted from the quantum numbers m_i and m_j which describe the projection of the components of the magnetic moment arising from the nuclear spin (I) and molecular rotation (J). The hexapole acts as a filter, preferentially passing some $m_i m_j$ along favourable trajectories while others are sent in unfavourable directions that will lead them to being pumped out of the surrounding vacuum. The non-thermal-

equilibrium $m_i m_j$ populated beams this produces have multiple fascinating applications. The majority of the groups recent work has focussed on the interaction of hydrogen (and deuterium) beams with single-crystal surfaces, exploiting the control over $m_i m_j$ to investigate the impact of molecular rotation on elastic[33, 34] & inelastic[35] scattering as well as in surface phonon generation[36]. More recently the technique has even been applied to molecular microscopy[37]. Most relevant to NSC measurements on water though is the simple fact that the technique has already been used to produce ***a magnetically focused molecular beam of ortho-water***[38].

To say the idea of a having a "pure" source of the spin-isomer of water that is both NMR detectable and by definition *not in its ground state* is attractive for the purposes of NMR measurement of NSC is an understatement. If a way could be found to hyperpolarise the molecules in a Cryomatrix in sufficient quantities to be observed (quantities that would be orders of magnitude smaller than required at thermal equilibrium due to the net polarisation approaching ~1), then NMR could be used to study NSC at any temperature wherein the matrix persists, the initial spin-isomer distribution being so astronomically far from equilibrium that significant NSC would occur at room temperature, let alone below 30K. Reality though is sadly less sunny. Hyperpolarised deposition and detection of water in the form of ice has already been attempted by a previous PHD student[39] and was sadly unsuccessful. While significant changes have been made to the apparatus (both mechanically and geographically) in the intermitting time and the interest in this case is in matrix-isolated water rather than ice, there is no guarantee the results would be different if attempted here.

There are two theoretical holes that make deciphering why a hyperpolarised deposition of water may fail difficult. Firstly, there is little understanding in current literature regarding what happens to the internal spin state of a molecule on adsorption to a substrate. It may be conserved, it may be altered, it may cease to be relatable to its previous state entirely (e.g if it can no longer rotate), the answer is simply unknown and a successful detection of signal from such an experiment would go someway to answering it. Secondly, the coherent control over m_i and m_j presented in [33-36] is only achievable due to the well understood Hamiltonian for hydrogen[40]. While at the instant it leaves the hexapole the overall wavefunction representing a given molecule of hydrogen can be said to be a "pure" eigenstate of the molecular Hamiltonian in the $m_i m_j$ basis the molecule will not remain in this pure state. The molecular Hamiltonian can be split into two sets of terms, those that are field dependent, and those that are not. Any change in $m_i m_j$ must be describable by a term within the molecular Hamiltonian. If only field dependent terms were present the molecule could be allowed to propagate freely in zero field and would remain in its hexapole-selected pure state. The presence of field free terms though renders this untrue. For hydrogen, provided the molecule is rotating $m_i m_j$ may change by spin-rotation coupling.

Except for those in the ground J=0 (para) state, all single molecules of water in the gas phase can be seen to be rotating. Without a clear understanding of the magnetic Hamiltonian of water it is not possible to say whether the enhanced polarisation provided by hexapole focussing would be preserved over the field free flight time

from hexapole to surface. This, the condensation related difficulties (Section 2.4) already observed in this work and the previously unsuccessful pure-ice depositions suggest that water is not the best candidate for a first attempt at hyperpolarised deposition and measurement.

While hydrogen would be an ideal choice molecule in terms of understanding its behaviour during beam propagation the current setup is not suitable for working with it, and there is little in-house experience working with hydrogen-containing cryomatrices. A molecule the group does have experience both with isolating and measuring the NMR signals of, that has also been demonstrated to be focusable (alongside acetylene) with a hexapole is Methane[41]. The next section will cover the properties of Methane, and why it has been chosen as a candidate for hyperpolarised deposition and measurement over water, which has been the focus of study up until this point.

Section 3.2: Methane, Characteristics and comparison to water:

Molecular Structure and Rotational States:

For an authoritative text on the rotational energies of methane, as well as polyatomic molecular rotors in general see [23], a brief description focussing on the properties which are relevant to the hyperpolarisation experiments is given below. Comprising four hydrogen atoms bound to a single carbon methane is the simplest alkane. The molecule has a tetrahedral structure, with a consistent bond angle of 109.5° between neighbouring hydrogens and a carbon-hydrogen bond length of 108.7pm. A rough schematic view of the molecule is given in Figure 3.2.1.

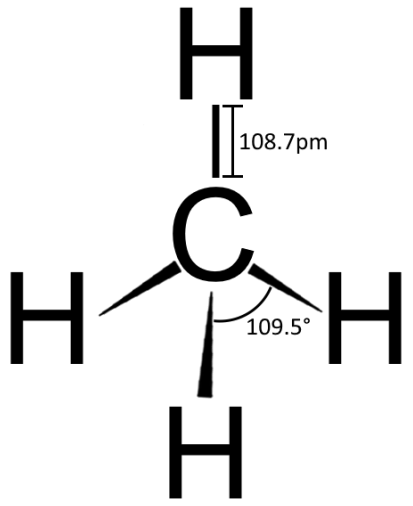

Figure 3.2.1: Schematic representation of Methane (CH_4) showing the single carbon (C) and four hydrogens (H), with lines/wedges indicating covalent bonds. Wedge tips point into the page. The bond angle and lengths shown are common to all 4 CH bonds. The molecule has tetrahedral structure, equivalent equilateral triangles may be drawn in the co-planar with any three hydrogens by placing said hydrogens as the vertices of the triangle.

In the rigid rotor approximation methane behaves as a spherical top. This implies that for any set of principle axis applied to the molecule, the moment of inertia about all three axes (and therefore rotational constants) will be equal. For methane the primary axis (A) is usually placed either co-axial with one of the C-H bonds, or coplanar with 2 hydrogens bisecting the bond angle, the conclusion is the same in both cases. Neglecting nuclear spin and centrifugal distortion, the energy (E_J) levels of a spherical top molecule take the form:

$$E_J = BhcJ(J+1) \qquad \text{(Eq. 3.2.1)}$$

Where B is the rotational constant of the rotor, h is Planck's constant, c is the speed of light in a vacuum and J is the rotational quantum number of the given energy level. The degeneracy of a given J state (g_j) in this model is given as:

$$g_j = (2J+1)^2 \qquad \text{(Eq. 3.2.2)}$$

Nuclear Spin Modifications, degeneracies and rotational populations:

Ordinary methane ($^{12}C\ ^{1}H_4$) possesses 4 spin half hydrogens, this allows for 3 total nuclear spin combinations *I*=0, 1 and 2. As was the case for water the requirement for the molecular wavefunction of methane to be antisymmetric under proton exchange places restrictions on which rotational energy levels may be occupied by molecules of a given total nuclear spin. Unlike in the case of water, the division between different *J* values is not a clean separation, with the exception of the lowest energy levels each *J* state contains degenerate states of all three "nuclear spin modifications"[23]. Which degenerate *J* state contains which nuclear spin modification is decided by the states symmetry . A member of the tetrahedral point group T_d methane' may take one of 5 symmetry types, A_1, A_2, E, F_1, and F_2. [Note: modern references / character tables[7] substitute the F_1, and F_2 labels for T_1, and T_2, while older works[23] and discussion of methane in literature[42-44] maintain the F_1, and F_2 notation preserved in this work]. In order of ascending total nuclear spin, states of *E* symmetry are occupied by *I=0*, *F* symmetry by *I=1* and *A* symmetry by *I=2*.

The introduction of these symmetry restrictions causes the degeneracy of states for a given *J* value to deviate from that expected from (Eq. 3.2.2). Individual degeneracies may be calculated from various formulas, Table 3.2.1 presents degeneracies for the first 15 J values, as presented in Herzberg[23].

Table 3.2.1: Total (g_J) and per-symmetry-type number of degenerate states for methane at varying *J*.

J	Symmetry of State			Total States (g_J)
	A (*I* = 2)	E (*I* = 0)	F (*I* = 1)	
0	5	0	0	5
1	0	0	9	9
2	0	10	15	25
3	35	0	42	77
4	45	18	54	117
5	0	22	99	121
6	130	26	117	273
7	75	30	180	285
8	85	68	204	357
9	190	38	285	513
10	210	84	315	609
11	115	92	414	621
12	375	100	450	925
13	270	108	567	945
14	290	174	609	1073
15	465	124	744	1333

The deviation from (Eq. 3.2.2) is easiest to see at low values of *J*, for example at *J*=0, where the (Eq. 3.2.2) value of g_j is 1, while the actual value is 5. In general, the value of g_j is seen to *approach* (Eq. 3.2.2) as *J* increases. Isolation of nuclear spin modifications between *J* states is only observed for *J*<2, with *J* states of *J*≤*2* all containing 2 or more of the three possible nuclear spin modifications.

Further to Table 3.2.1 there is an additional degeneracy g_i associated with the Zeeman splitting of each nuclear spin state, this takes values of 5,1 and 3 for the A, E and F modifications respectively. As was the case for water, the population of the rotational states for a given rotational temperature (T_{Rot}) may be calculated using a Boltzmann distribution. For a given value of J the number of states ($q(J)$) occupied at temperature T_{Rot} may be taken as:

$$q(J) = g_i g_j e^{-\frac{E(J)}{k_b T_{Rot}}} \quad \text{(Eq. 3.2.3)}$$

Where g_i and g_j are the degeneracies of the given J state owing to nuclear spin and rotation (Table 3.2.1) respectively, $E(J)$ is the energy of the state relative to $J = 0$ and k_b is Boltzmann's constant. The partition function may therefore be defined as:

$$Q(J) = \sum_J g_i g_j e^{-\frac{E(J)}{k_b T_{Rot}}} \quad \text{(Eq. 3.2.4)}$$

And the final population of a given state defined as:

$$P(J) = \frac{q(J)}{Q(J)} \quad \text{(Eq. 3.2.5)}$$

These equations will be employed in later sections to aid in beam modelling and estimation of the final polarisation.

Advantages of methane for hyperpolarised NMR measurements:

Section 2.4 discussed the apparent loss of water from the gas mixture, attributed to condensation at the nozzle. Condensation of the sample species is a concern both for larger scale "macro" depositions such as those previously discussed for water, and for molecular beam experiments where the molecular beam is produced by supersonic expansion from the nozzle. To avoid condensation the partial pressure of the sample gas within the gas lines must be below the vapour pressure of the sample gas at the temperature of the lines. The most important of these temperatures are those at the nozzle within the bore, and the nozzle that will be used for the molecular beam. Of the two, the colder is expected to be the nozzle within the bore, which in Section 2.4 was estimated to be ~265 K at the coldest. Interest in the vapour pressure of methane in literature[45-47] is primarily concerned with its behaviour between its triple (~90 K) and critical point (~190K) temperatures. The vapour pressure at the upper end of this range (well below the minimum measured here) boundary is reported[45] to be in the region of 2 MPa, or 20 bar. 20 bar is orders of magnitude higher than any pressure that would be employed in the NMR experiments described here. Condensation of the methane can be dismissed as a concern, with room for much higher concentrations of methane to be tested in macroscopic depositions, and relatively high nozzle pressures available for the generation of a molecular beam.

An additional benefit of methane is the increase in protons-per-molecule. Methane has twice the number of hydrogens. Employing the simple ensemble of spin-half molecules estimation for the thermal-equilibrium polarisation, this should give twice the polarisation per molecule. As was the case for water, methane is expected to occupy a single-substitution site in an argon matrix[6], a deposition of CH_4@Ar would

therefore be expected to produce twice the signal of a H_2O@Ar deposition of equivalent concentration.

Finally, there is the topic of the nuclear spin itself. There are two considerations here; the first relates to macroscopic experiments., to characterise the methane samples their NMR time constants (T_1, T_2, and T_2^*) must be measured with a sample at a range of temperatures. A difficulty in this encountered with the water samples at low temperatures (~6K) was loss of signal due to nuclear spin conversion. The ground rotational state of water is *I*=0, which is not NMR active. This is not the case for methane, looking to Table 3.2.1: Total (g_J) and per-symmetry-type number of degenerate states for methane at varying *J*. the ground *J* state is *I=2*, while the first and second excited rotational states (*J*=1,2) both have NMR active *I=1* components. The expected populations of different *J* states for both macro-deposited characterisation experiments and molecular-beam experiments are discussed in later sections, for now it is enough to conclude that nuclear spin conversion causing loss of useable signal at cold temperatures is less of a concern for methane than for water.

The second consideration pertains to molecular beam experiments. Field free mixing presents a route for loss of polarisation for rotating molecules within a magnetically polarized molecular beam. In the experiments using hydrogen presented in [33-36] this mixing is mitigated by the presence of the solenoids along the beam path. In the presence of a sufficiently strong magnetic field the field-dependent terms of the Hamiltonian dominate[40] and the evolution of the molecular wavefunction can be predicted from the molecular Hamiltonian and the field experienced by each molecule. To the authors knowledge, accurate molecular Hamiltonians for both water and methane are not known to exist. It is therefore not possible to predict whether field free mixing would result in complete loss of polarisation before the molecules in the beam reach the surface. The key difference between methane and water here is the NMR activity of their *J*=0 states. Water has *J*=0 *I*=1, Methane has *J*=0, *I*=2. While in the later experimental section “best-guess” magnetic fields have been introduced along the beam line to avoid field-free mixing, the presence of a "non-rotating” (*J*=0) NMR active state in methane ensures that even should said fields be ineffective some polarisation should still make it to the target.

Section 3.3: Apparatus Overview:

Figure 3.3.1 provides a simplified overview of the proposed assembly to be used in a hyperpolarised deposition experiment. The schematic has been divided into regions identified with titles in blue.

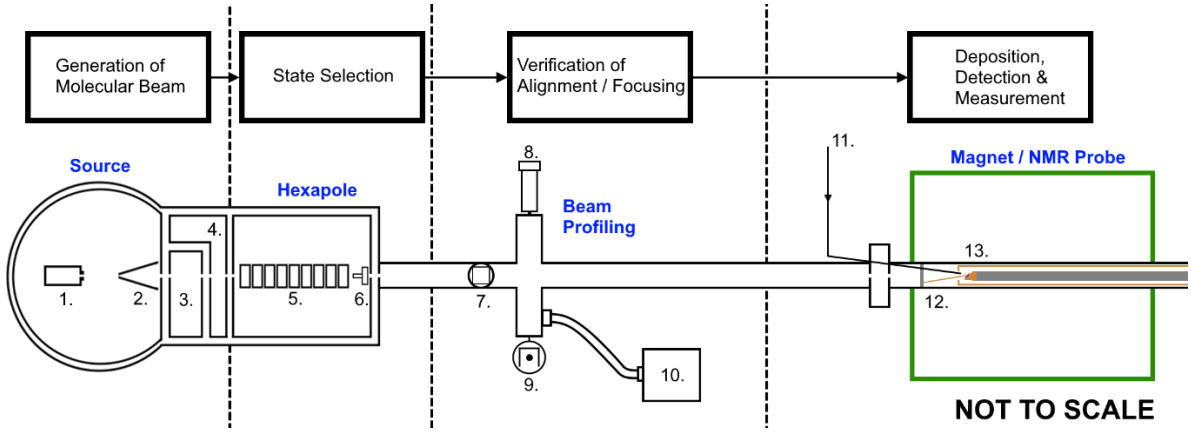

Figure 3.3.1: Schematic of the experimental apparatus. Sections are labelled in blue and separated by dashed black lines. The block diagram at the top of the figure references the responsibility of the given section as the beam propagates from left to right. Numbered labels indicate key components: 1. 150μm nozzle, 2. 300μm skimmer, 3. First differential pumping section, 4. Second differential pumping section, 5. Hexapole assembly, 6. Dipole element, 7. Vertical flag, 8. Horizontal flag, 9. Cold Cathode Gauge, 10. Hiden pulse counting mass spectrometer, 11. Matrix deposition line, 12. NMR coil assembly, 13. Deposition target.

The block diagram at the top of the schematic indicates the role performed by each part of the apparatus. The following sections will cover each region in additional detail, to give a brief overview:

- Source (Section 3.4): Responsible for generation of the methane molecular beam. The nozzle (1) is responsible for the initial supersonic expansion, the skimmer (2) selects the central region of the expansion with components of velocity primarily along the beam axis.
- Hexapole (Section 3.5): responsible for the spatial separation of beam components by magnetic moment. The hexapole magnets (5) create the magnetic field gradients required to deflect molecular trajectories and perform magnetic separation while the dipole elements (6) align the magnetic moments to a well-defined laboratory axis (chosen to be parallel to the beam axis).
- Beam Profiling (Section 3.6): Allows for profiling of the molecular beam. The flags (7&8) allow different regions of the beam to be selected / blocked, while the pressure gauge (9) and mass spectrometer (10) allow for detection of the blocked component.
- Magnet / NMR Probe (Section 3.7): Holds the cryocooled deposition target (13, ~6K) in line with the beam and under strong magnetic field (5-6T). The rare gas for the Cryomatrix is supplied from an external line (11) running to a 10μm nozzle in the magnet bore. The NMR coil assembly for these experiments was detached from the cold finger, supported by an aluminium slip-ring braced against the magnet bore walls.

Section 3.4: The Source:

Source Construction and Relevant Theory:

The source/hexapole assembly used in this work was originally designed to work with water beams[38, 48], having also been validated as a beam magnetically focused beam source for acetylene and methane[41]. Figure 3.4.1 (right) provides a photograph of the nozzle (labelled: 1.) and skimmer (labelled: 2.). The nominal separation (across the page) of the nozzle / skimmer is 15mm, with the horizontal (into/out of the page) and vertical (up and down the page) position of the nozzle being adjustable via external manipulators. For the methane experiments discussed in this work the nozzle was left with the heating disengaged, the measured temperature of the nozzle was ~293K.

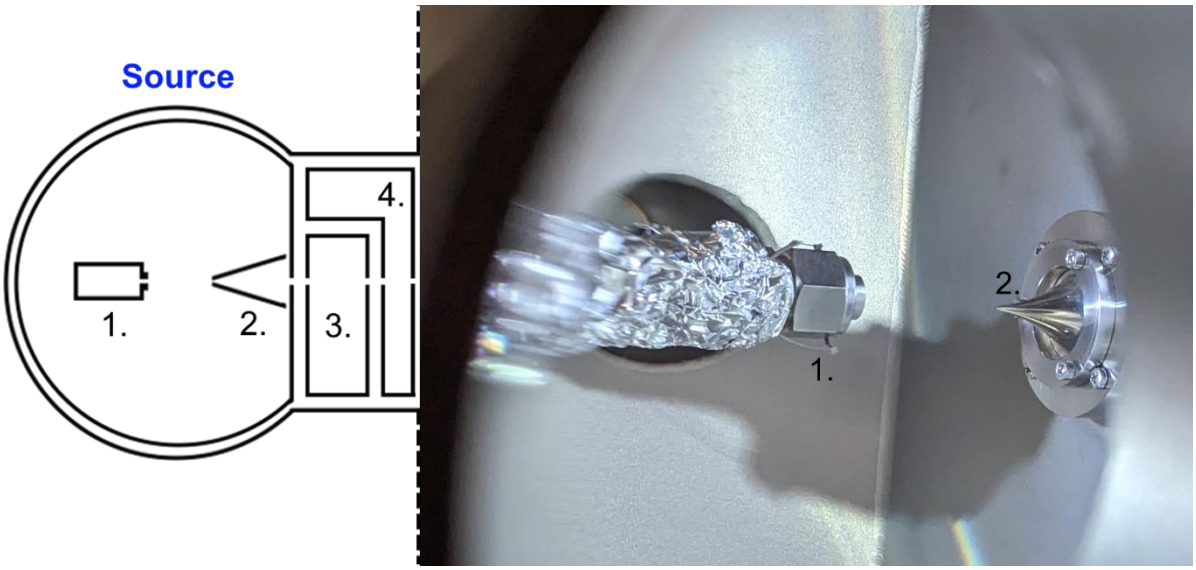

Figure 3.4.1: Subsection of Figure 3.3.1 displaying a schematic of the source region (left) and photograph (right) of the nozzle (1) and skimmer (2) used in the methane beam source. The pipework leading up to the nozzle can be seen to be wrapped in aluminium foil, providing insulation for the nozzle heating. The nozzle temperature may be monitored via a thermocouple, spot welded to the Swagelok connection close to the nozzle. Chambers 3 and 4 in the (left) schematic are differential pumping sections.

The source chamber itself is pumped via a *Sumimoto* H-20 cryopump (30000 L/s pumping speed for Ar). The baseline pressure in the source chamber with the pump engaged and nozzle closed was on the order of 5×10^{-7} mbar. The chambers labelled 3. and 4. (Figure 3.4.1) are differential pumping sections.

To produce a molecular beam gas is introduced to the nozzle, this gas is presumed to freely undergo supersonic expansion within the vacuum. The central portion of the beam, with components of velocity primarily along the beamline, is collected by the skimmer. The discarded portion of the expansion is pumped by the cryopump, the differential pumping sections ensuring minimal leakage of the relatively high source pressure into the latter higher vacuum regions of the machine, preventing beam attenuation due to collisions with gas phase molecules.

An additional feature of the source is the presence of a laser in line with the skimmer, allowing for visual alignment of some components of the beamline when the nozzle is retracted. The visibility of a laser spot at any point along the beamline indicates

that there is line of sight from the skimmer aperture to that point, in combination with spatial beam profiling (Section 3.6) this can also be used to confirm the beam is striking a desired target.

Source Optimisation:

In contrast to previous experiments[38, 41, 48] which have employed both seeded beams and varied nozzle temperatures when generating their molecular beams, the experiments in this thesis were performed using a pure methane beam with the nozzle at ambient temperature. The choice of pure methane was to ensure maximum flux (and therefore polarisation) of methane along the beamline, without diluting the beam or introducing possible complications due to mass-based segregation of beam components. The choice of ambient temperature was simply due to the lack of need for heating, unlike with water there was no risk of methane condensing at ambient temperature with the nozzle pressures tested. As will be shown later (Section 3.5 & Section 3.6) a beam generated nozzle temperature of 293K was acceptably focussed for the purpose of hyperpolarised deposition.

The two remaining variables to be optimised with regards to the source then are nozzle pressure and position. The maximum possible signal a hyperpolarised deposition can provide (see Section 3.8) is directly tied to the deposition rate. In general, faster is better and the most intense beam possible is desirable. In terms of pressure behind the nozzle (referred to as nozzle pressure below) this may be crudely interpreted to mean higher = better. A complication in this case is the limited size and operating pressure of the mixing cylinder available to hold the methane for the beam. The best compromise found after initial testing was a nozzle pressure of 150 mbar, this gave an easily detectable beam with sufficient runtime (~45 minutes) to average data collection over.

The nozzle position was optimised manually, first with pure argon then pure methane, by adjusting the nozzle position systematically in 3 dimensions, and noting the change in pressure at different points down the machine. The higher the pressure down the beamline, the more of the beam was making it to the target. This procedure allowed the nozzle to be retracted and laser passed without the risk of misalignment when the nozzle was reinserted.

Source Modelling:

Molecules undergoing supersonic nozzle expansions are observed to exhibit rotational cooling, with existing literature[42-44] reporting that in the case of methane this cooling occurs without nuclear spin conversion. As a result, the rotational temperature and therefore average *J* state of a molecule within the beam will be lower than pre-expansion, in contrast to the nuclear spin populations which will remain in their pre-expansion distribution. When applying (Eq. 3.2.5) to calculate the total population in a given rotational state, the calculation will need to be split into three separate branches, each associated with one of the nuclear spin modifications with the energies adjusted to be relative to that of the lowest value of *J* present for that modification. Additionally, the energy from cooling must be transferred somewhere, that somewhere being the translational energy of the molecule. The translational energy, and therefore velocity, of the molecule is an important factor in

the focussing process. The time a molecule spends within the hexapolar lens, and thus the amount of time the inhomogeneous field may act on it, being inversely proportional to the speed the molecule travels through it.

For a gas of molecular mass m expanding from a nozzle with initial temperature (T_N) the terminal velocity (v_∞) of a molecule in an ideal supersonic expansion is given by[49]:

$$v_\infty = \sqrt{\frac{2k_b}{m}\left(\frac{\gamma}{\gamma-1}\right)T_N} \qquad \text{(Eq. 3.4.1)}$$

Where γ in this case is the ratio of the specific heat capacity of constant pressure to constant volume ($\gamma = \frac{C_P}{C_V}$) for the gas. The relationship holds for an ideal gas, with the assumption that the rotational temperature post expansion has fallen to 0K (complete rotational cooling). The real expansions seen in experiments are not ideal, but (Eq. 3.4.1) provides a good starting point estimate for the central/average velocity of the velocity distribution seen in real expansions.

Section 3.5: The Hexapole:

Overview and Structure:

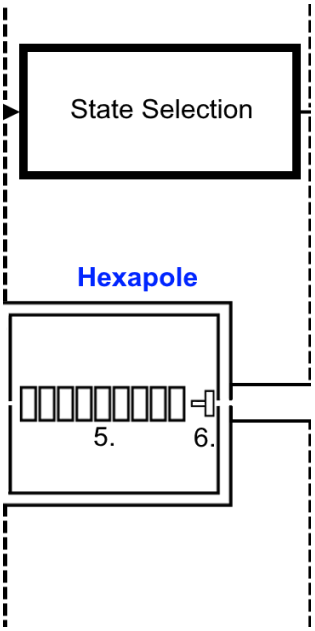

Figure 3.5.1: Subsection of Figure 3.3.1 relevant to this section. "5." Is comprised of hexapole 9 elements (Figure 3.5.2 A) terminating in a hexapole to dipole element (Figure 3.5.2 B). "6." Is an electromagnetic dipole designed to shift quantisation axis of the molecular magnetic moments parallel to the direction of propagation.

Figure 3.5.1 displays the subsection of Figure 3.3.1 responsible for state selective focussing of the molecular beam (via the hexapolar magnetic lens, "5.") and aligning the quantisation axis of the molecular magnetic moments along the beam propagation axis. The hexapole itself is a segmented design consisting of 9 50mm sections with the appearance of Figure 3.5.1 A. The design is an iteration on the hexapolar magnetic lenses developed in Cambridge for the manipulation of ^{3}He molecular beams[32]. The use of a segmented design allows defocused components of the beam to exit the lens, preventing a buildup which could otherwise attenuate the beam. The physical basis for the action of the hexapole is covered later in this section.

The final element of the hexapole is a hexapole to dipole element, the accepting face of this segment has the same appearance as the other segments, the final face having the appearance of Figure 3.5.2 B. Comparing the two reveals that 4 of the 6 pole pieces transition from sharp points to smooth curves over the width of the segment. The final dipole is created by the two remaining sharp pole pieces, oriented perpendicular to the beamline. Final alignment of the spins along the propagation axis is achieved via an electromagnet labelled "6." in Figure 3.5.1. This is a simple solenoid, the direction of current flow being chosen to align the field within perpendicular to the field within the NMR magnet bore. The fields in the transitions between all elements in the assembly, and between the last element and the field produced by the dipole, and were estimated to maintain the conditions for an adiabatic transition (i.e. the frequency of the transition is slow with respect to the Larmor frequency).

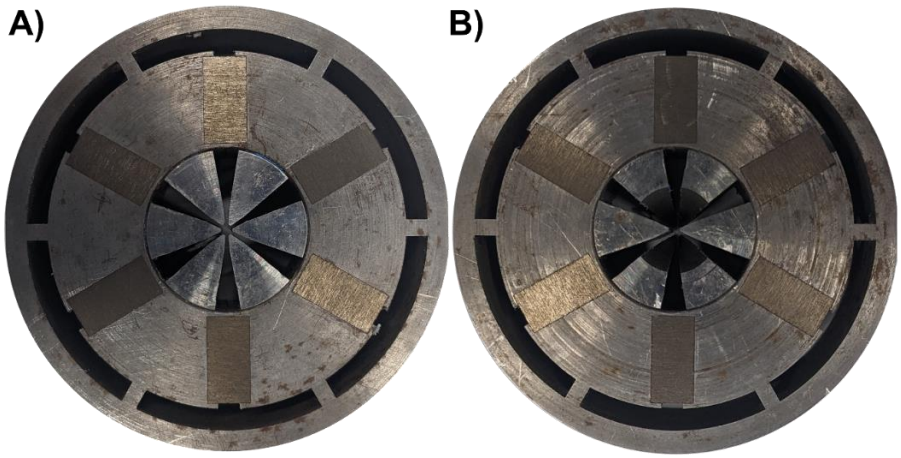

Figure 3.5.2: Face-on Examples of a A) Hexapole element and B) Hexapole to dipole element (dipole side). Both assemblies feature a Halbach array of permanent (NdFeB) magnets (bronze-hued

rectangles) inside a mild steel yoke. The central (silver hued) pole pieces are high magnetic susceptibility alloy (Permandur 49) which focus the field into the desired shape.

Working Principle:

The hexapolar magnetic lenses that the Swansea surface science group works with are based on designs originally made to work with ^{3}He[32]. Neglecting higher order multipole aberrations, within the bore of the hexapole the magnetic field $\boldsymbol{B}_{Hex}$ may be expressed as:

$$\boldsymbol{B}_{Hex} = 3C_3 r^2 \left(\cos 3\theta\, \hat{\boldsymbol{r}} - \sin 3\theta\, \hat{\boldsymbol{\theta}}\right) \quad \text{(Eq. 3.5.1)}$$

In cylindrical polar coordinates, where r is the radius from the hexapole centre, θ is the azimuthal angle and C_3 is an empirical hexapole coefficient. The magnitude of this field is given by:

$$|\boldsymbol{B}_{Hex}| = 3C_3 r^2 \quad \text{(Eq. 3.5.2)}$$

Which can be seen to be purely radial. The field is inhomogeneous, with the magnitude of the field gradient lying along the radius of the bore. Separation of $m_i m_j$ states within the hexapole is achieved by the action of this field gradient on the magnetic moment of the molecules passing through it. From classical physics the potential energy (U) of a magnetic moment ($\boldsymbol{\mu}$) inside an external magnetic field ($\boldsymbol{B}$) may be given as:

$$U = -\boldsymbol{\mu} \cdot \boldsymbol{B} \quad \text{(Eq. 3.5.3)}$$

While the force a magnetic moment experiences due to said field may be given as:

$$\boldsymbol{F} = -\nabla U \quad \text{(Eq. 3.5.4)}$$

The negative sign indicates that the force acts against the gradient in potential energy, i.e. to minimise the potential energy of the magnetic moment. The internal magnetic moment of a molecule may be seen as a sum of multiple components:

$$\boldsymbol{\mu} = \boldsymbol{\mu}_e + \boldsymbol{\mu}_I + \boldsymbol{\mu}_J \quad \text{(Eq. 3.5.5)}$$

Where the subscripts e, I and J correspond from components arising from electron spin, nuclear spin and molecular rotation respectively. All molecules considered in this thesis are closed shell molecules with electron spin of zero, implying $\boldsymbol{\mu}_e = 0$. Furthermore, the rotational g-factor of methane is on the order of 0.3[50], while the g-factor of a single proton is 5.6, implying $\boldsymbol{\mu}_I \gg \boldsymbol{\mu}_J$. Focussing behaviour within the hexapole is therefore assumed to be dominated by $\boldsymbol{\mu}_I$ and $\boldsymbol{\mu}_J$ is neglected in the initial assessments presented in this work. Assigning a sufficiently strong magnetic field along the z axis ($\boldsymbol{B} = B_z \hat{\boldsymbol{z}}$) the magnetic moment of the molecule of total spin I within the field may be expressed as:

$$\boldsymbol{\mu} = m_i \mu_I \hat{\boldsymbol{z}} \quad \text{(Eq. 3.5.6)}$$

Where m_i is the magnetic quantum number associated with the nuclear spin and μ_I the magnitude of the magnetic moment. Substituting this in gives:

$$\boldsymbol{F} = -m_i \mu_I \nabla B_z \quad \text{(Eq. 3.5.7)}$$

Which shows that the force acts along a field gradient. The behaviour of a molecule travelling through the hexapole can be divided into three categories:

- Neutral: Molecules with $\boldsymbol{\mu} = 0$ exhibit this behaviour, passing through the hexapole with their trajectories unaffected.
- High-Field seeking: Molecules with $\boldsymbol{\mu} > 0$ exhibit this behaviour. Trajectories for these molecules are bent outwards from the beam axis towards the edges of the hexapole (defocussed) where the field is strongest.
- Low-Field seeking: Molecules with $\boldsymbol{\mu} < 0$ exhibit this behaviour. Trajectories for these molecules are bent towards the centre of the hexapole where the field is 0.

The sign of $\boldsymbol{\mu}$ is dependent of the sign of the gyromagnetic ratio for the spin-containing nuclei in the molecule. For Hydrogen containing molecules such as methane and water this sign is positive by convention, this implies that positive m_i states are defocussed, negative m_i states are focussed, and $m_i = 0$ is unaffected.

Hexapole Modelling:

Modelling of the behaviour of different projection states within the hexapole allows the spatial distribution and relative populations of states within the final beam to be predicted. The modelling process used is semi-classical. Components of the beam and their overall proportions are taken from spin-statistics, the spin direction is quantised to be either parallel or antiparallel to the field gradient direction, whereas the motion of the particles is derived from classical equations of motion. The behaviour of the particles may be divided between regions with and without a field gradient. In regions of zero or homogeneous magnetic field the model is a simple ray-tracing model which assumes particles travel in straight lines with constant velocity. In regions with a field gradient (inside the hexapole) the space is discretised into short regions (0.1mm was found to be sufficiently small) within which the magnetic forces and changes in velocity of the particles due to (Eq. 3.5.7) are accounted for numerically via a 3rd order Runga-Kutta solver. Input velocities for initial models were taken from (Eq. 3.4.1), with the starting positions for particles being evenly distributed over a region defined by the position and radius of the skimmer.

The hexapole section of the model is the most computationally taxing, requiring heavy discretisation, while geometry beyond the hexapole need only be evaluated at the points said geometry interacts with the beam. To minimise computational cost the hexapole section of the model is run once with a high (~1.2×10^6) number of particles for each m_i state and velocity. The resultant trajectories are saved at the end of the hexapole and may then be used to model any post-hexapole machine geometry desired. Particles which cross into regions where they would meet an obstacle (hexapole / vacuum system wall, apertures) are culled from the modelling process, the likelihood of a particle surviving may therefore be taken as the proportion remaining at the end of the model compared to the number at the start.

Figure 3.5.3 displays slices through a simulated methane beam at 0, 0.7 and 1.4m (A, B and C) from the end of the hexapole. An equal number of particles are shown

for each m_i state in the beam, with more focussed particles being plotted overtop of less focussed particles for visibilities sake. Subfigure A is a slice positioned at the end of the hexapole where the 2mm bore diameter confines all surviving particles to be within 1mm of the bore centre. Subfigures B and C display slices further down the beamline (0.7m and 1.4m from the end of the hexapole) and clearly demonstrate the focussing effects of the hexapole. Low field seeking negative m_i states are focussed toward the centre of the beam while high field seeking positive m_i states diverge, the effect becoming more pronounced as the beam propagates further (subfigure B to C).

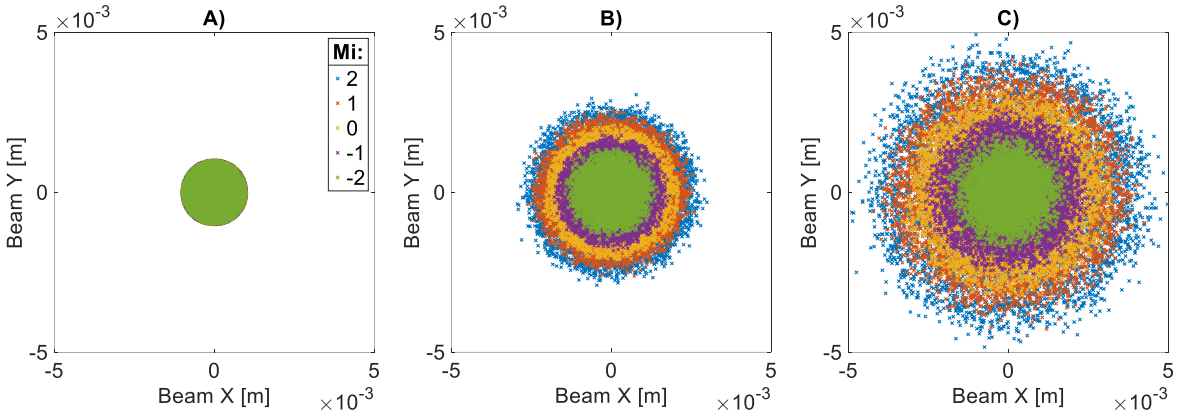

Figure 3.5.3: Slices through model methane beams perpendicular to the direction of propagation. Each plot shows 1000 simulated particles per m_i as state as labelled in A. Distance from the end of the hexapole increases left to right with A) at the end of the hexapole, B) 0.7m from the end of the hexapole, C)1.4m from the end of the hexapole (position of the deposition surface). Particle spread is seen to correlate with m_i state, “high field seeking” negative m_i states spreading out the most while the “low field seeking” positive states remain towards the centre of the beam. m_i zero is seen to diverge an intermediate amount.

The models in Figure 3.5.3 assign no geometrical constraints other than the 2mm diameter of the bore. In the next section apertures (both stationary and moving) will be included to allow direct comparison of the model to experimental beam profiles.

Section 3.6: Beam Profiling:

Introduction and profiler construction:

Profiling the molecular beam allows the focussing of the beam to be verified as well as ensuring that the beam will strike the deposition target. Figure 3.6.1 displays the relevant region of Figure 3.3.1 alongside a photograph of the profiling section of the machine taken during construction.

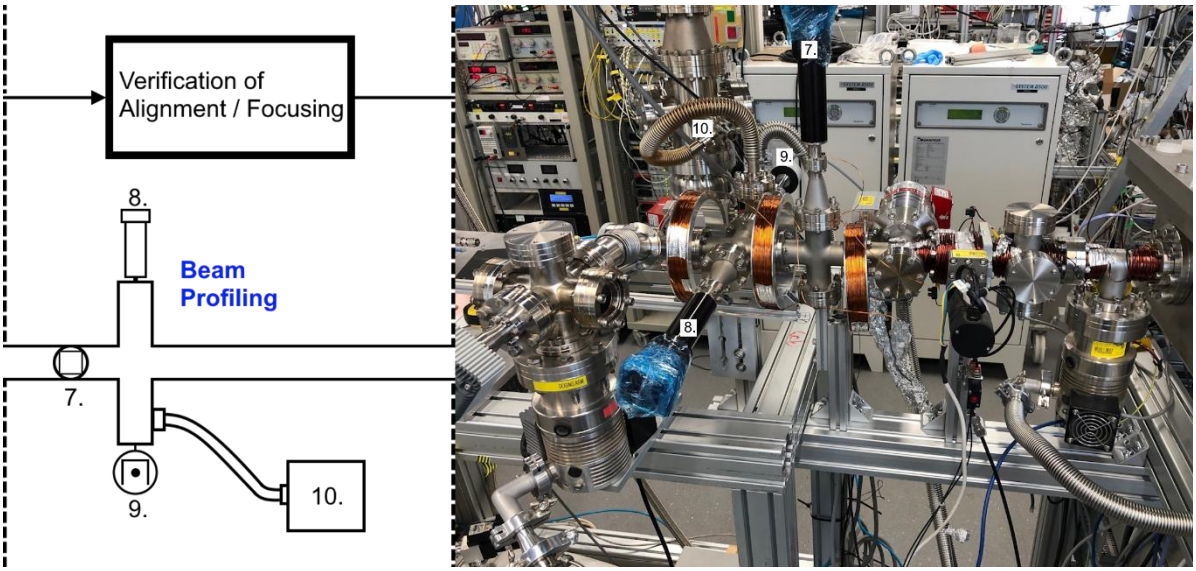

Figure 3.6.1: Region of Figure 3.3.1 (left) showing the beam profiling region of the machine, alongside a photograph of the region (right) during initial construction where the numbered elements are clearly visible. The mass spectrometer (10.) and cold cathode gauge (9.) allow for the detection of deflected / obstructed components of the beam. The vertical (7.) and horizontal (8) manipulators allow slotted flags (see below) to be inserted into the beam path. The ends of these manipulators (wrapped in blue plastic in the image) were fitted with addressable stepper motors in the final setup.

The physical profiling of the beam is achieved via the linear manipulators (“7.” And “8.”) which in the final assembly are motorised, allowing for computerised control of the insertion metal slot plates (dimensions of which are displayed in Figure 3.6.2) into the pathway of the beam. The smallest flag movement possible is 0.2mm, with the total range allowing for all slots to fully cross the ~2mm maximum beam width. As can be seen in Figure 3.6.1 the flags are held perpendicular to one another, careful positioning of flags creating square or rectangular apertures which may be shifted across the 2d plane perpendicular to beam propagation. The mass spectrometer (“10.”) and pressure gauge (“9.”) inline with the horizontal flag (“8.”) allow for the interaction between the flags and molecular beam to be detected. Scripts were constructed in MATLAB allowing the readings from the mass spectrometer to be recorded in sync with the flag motion. The placement of the detectors inline with the second flag, rather than downline of the flags and in the path of the beam, results in the detectors being sensitive to the beam scattering from the surface of the flags. Molecules which either pass through a slot or do not scatter to the detector are eventually turbo-pumped out of the system. Flag positions where the beam passes through the slots will therefore be represented as minima in the data, while obstruction will result in a maxima.

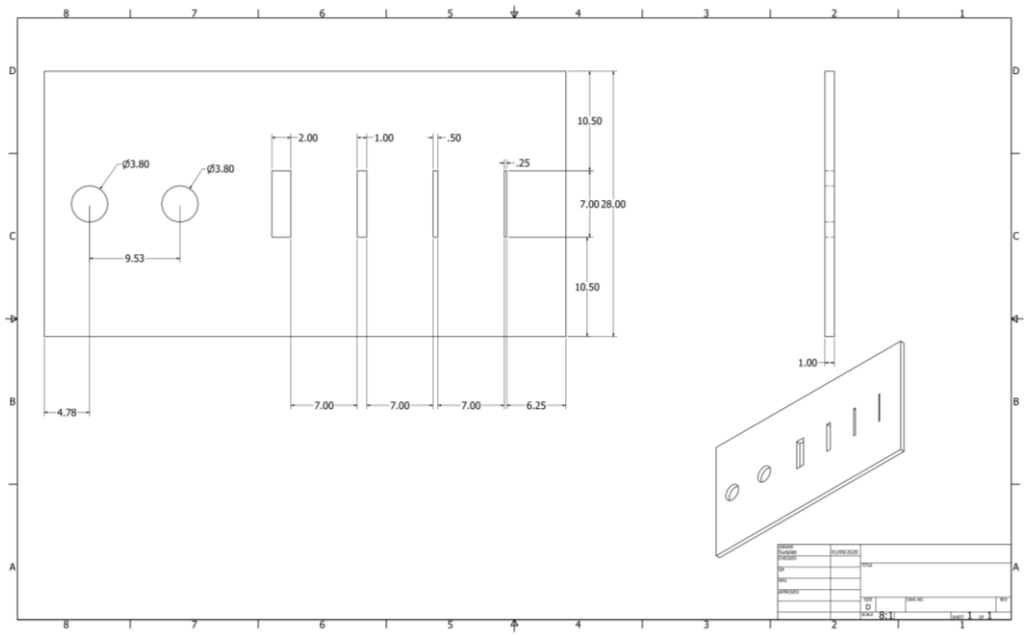

Figure 3.6.2: Design schematic for the flags. All measurements provided in mm. The two 3.8mm holes on the left hand side of the flag are for affixing of the flag to the manipulator arms. The range of slit sizes allow for creation of different rectangular apertures when two plates are aligned perpendicular to each other.

Collecting signal from scattered molecules does present an issue, the sensitivity of the detector is impacted by how easily said molecules can scatter towards the detector. There is no clean line of sight from either flag to the detectors, molecules must therefore first scatter from the flag, eventually arriving at the flags by random motion. The longer the path from initial scattering to point of detection, the less likely it is that a particle will make it to the detector. Signal arising from scattering at the first flag is therefore harder to detect than that from the second, which is closer to the detector. Ideally, the detector would be placed downline of the flags directly in the beam path. The scattering-based method was chosen due to it being significantly simpler to incorporate in-conjunction with the machines final goal of using the beam for deposition, rather than devising a system that allows the detector itself to be inserted / removed from the path of the beam.

Further issues, relating to the flags having physical thickness and not being perfectly perpendicular to the beam path were highlighted during initial profiling of the system using a neutral beam of pure argon.

Initial Profiling:

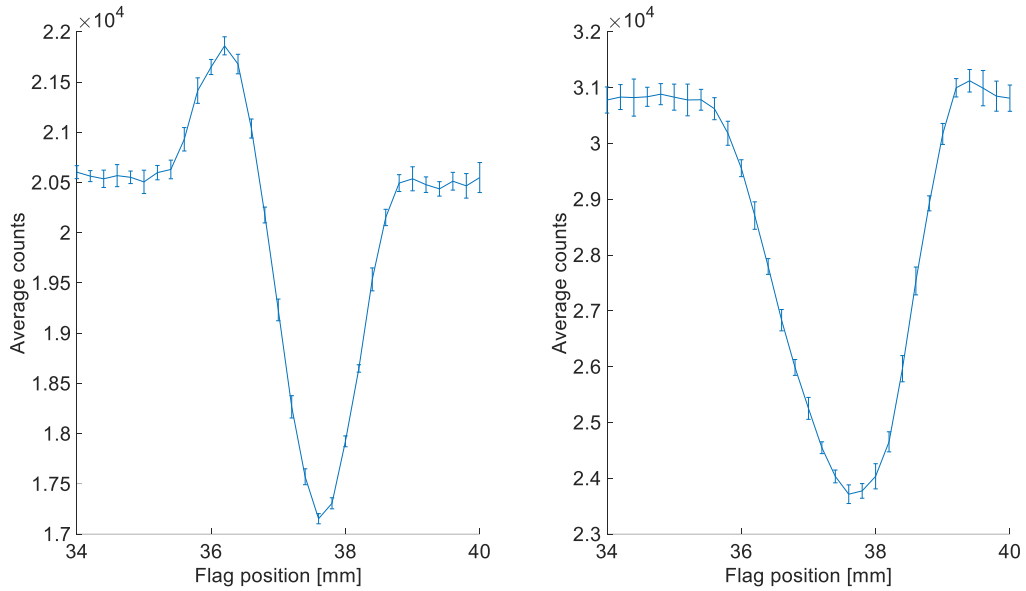

Figure 3.6.3: A) Single flag scan using the vertical flag and a pure argon beam. The manipulator positions displayed correspond to the 2mm slot in the flag. A significant increase in counts is seen between 35 and 37mm, indicating enhanced scattering towards the detector. The apparent minimum correspondent with the centre of slot lies at ~37.6mm. B) Single flag scan using the horizontal flag and a pure argon beam. The manipulator positions displayed correspond to the 2mm slot in the flag. The apparent centre of the 2mm slot from the profile is at ~37.8mm on the flag manipulator.

The profiling system was initially trialled using a pure argon beam. This allowed for testing of the communication scripts between the motors, detector and control computer and verification of the alignment of various components without needing to account for the effect of the hexapole (argon being total spin 0). Figure 3.6.3 displays a subset of the results of one such experiment, corresponding to a scan of the 2mm slot in each flag. In this case, Argon was supplied to the nozzle at a backing pressure of 200mbar and the beam allowed to pass freely from the source to the end of the beamline. An individual flag was selected and allowed to sweep through the beam over its full 40mm range in steps of 0.2mm, the other flag being kept fully retracted out of the beam path.

Both Figure 3.6.3 A) and B) display a clear minimum, representing the position at which the centre of both the 2mm slot and beam are best aligned. The detector settings were the same for both scans, the difference in plateau counts (maximum obstruction) between A) and B) being ~1.05×10^4 with the higher counts being present in the horizontal flag scan. This is inline with the earlier comment that a greater proportion of scattered molecules from the horizontal flag will be detected than from the vertical. An anomaly present in A) but not in B) is the increase in counts on the left-hand-side edge of the 2mm slot for the vertical flag. This indicates enhanced scattering that cannot be explained by the flag sliding smoothly through the beam at 90° to the propagation direction. A likely explanation in this case is misalignment of flag with the plane perpendicular to the beam. In this case the thickness of one edge of the slot would be exposed to the incoming beam, creating a larger surface for scattering and therefore a larger signal. Given that the probe molecules are argon in

this case a deviation from the expected beam direction can be eliminated as a culprit. Identifying the source of misalignment beyond this is difficult, the flags have been observed to exhibit some unintended motion perpendicular to their direction of travel in the plane of the flag itself, but the misalignment could also arise from some other element in the system.

Following the collection of these results the hexapole chamber was opened to check the alignment of the skimmer and hexapole using the laser. The laser was observed to be clipping the inside of the hexapole bore and the hexapole position was adjusted to address this. Subsequent single flag scans with the adjusted hexapole position did not show the anomalous increase in counts seen in Figure 3.6.3 A).

Second Profiling Run:

With the functionality of the profiling setup verified, attention was turned to profiling the methane beam. The mixing cylinder previously used to hold deposition gasses for macro-deposition experiments was filled to 800mbar with pure methane following 3 fill-purge cycles with 800mbar pure argon. During beam operation methane was supplied to the source at a backing pressure of 150mbar, a value found to strike an acceptable balance between beam intensity and total operating time (45mins – 1hour) before the cylinder pressure fell too low to regulate. The nozzle position was optimised using the principles laid out in Section 3.4.

Profiles for this subsection were collected using both flags simultaneously. Signal constraints limited the usable data to that collected with the first (vertical) flag fixed in position, and the second (horizontal) flag being moved through the beam. The vertical flag position was chosen to be aligned with the centre spot of the laser (estimated accuracy within ~0.5mm). The chosen slot width for both flags was 2mm. The resultant profiles are a 2x7mm horizontal slice through the beam at 0.2mm step size, each data point being the average counts for a 2x2mm square aperture.

To accompany the experimental profiles, simulated profiles considering only the m_i states of methane were run. The choice to only consider m_i arises from the unknown rotational temperature of the beam, and therefore difficulty in estimating the statistical weights in m_j. Previous studies have demonstrated m_i-only models to sufficiently explain experimental beam profiles[41], the impact of m_j on focussing being dominated by m_i due to the g-factor associated with nuclear spin being much larger than that for molecular rotation. A range of model velocities were tested, above and below the velocity expected from (Eq. 3.4.1) at a nozzle temperature of 273K.

The results of both experiment and model make up the sub figures of Figure 3.6.4. Figure 3.6.4 A shows normalised (to their respective maxima) experimental profiles for both pure argon and methane. The x-axis is plotted in terms of displacement of the centre of the moving slot from the observed centre of the laser.

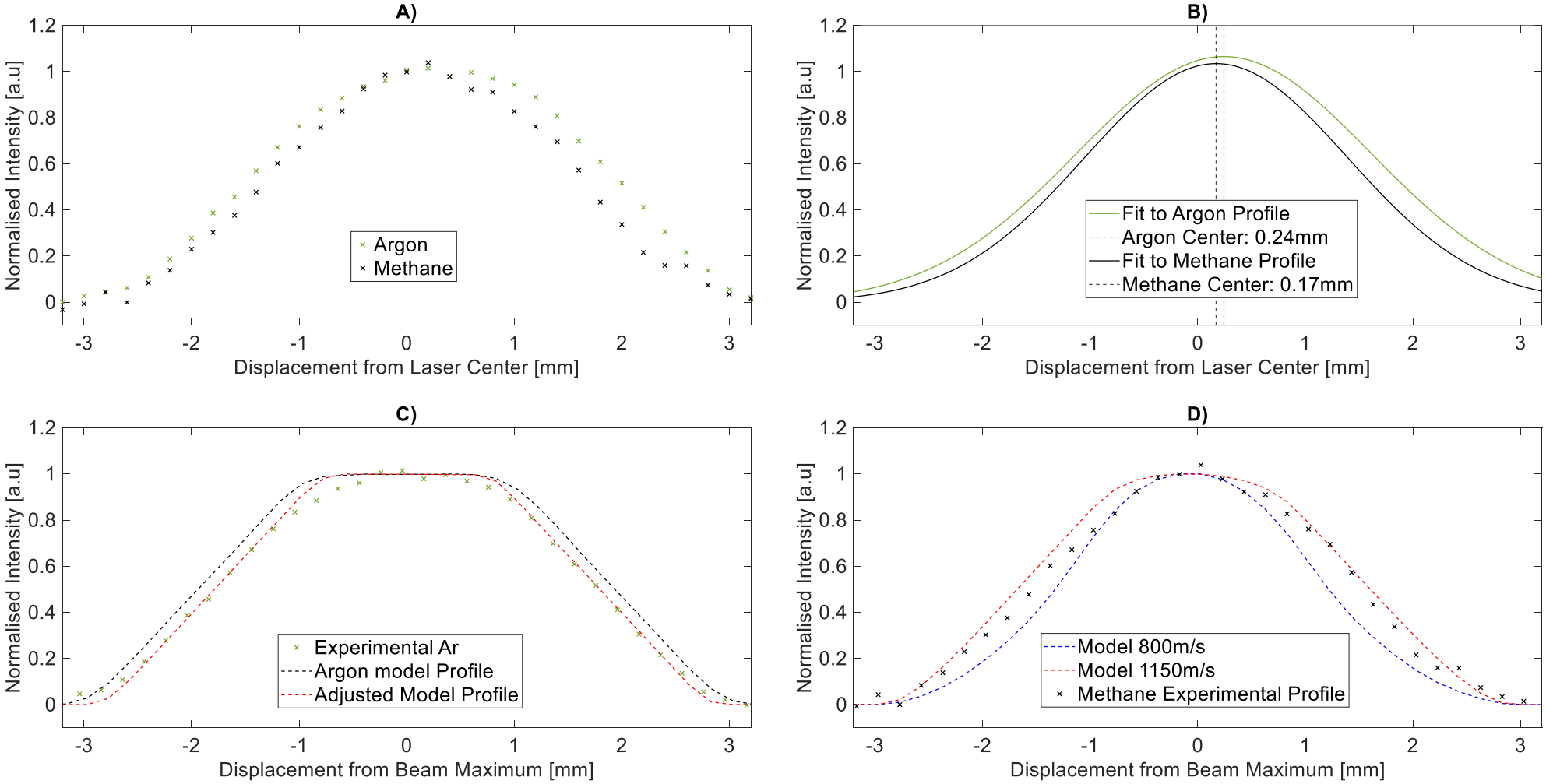

Figure 3.6.4: A) Experimental 2x2mm Square aperture horizontal profiles for Argon (green) and Methane (Black) at 150mbar backing pressure. B) First order Gaussian fits (solid lines) to the profiles shown in A. Dashed lines identify the maxima in each line. Both maxima are off-centre with both the laser and each other. C) Argon experimental profile (green x's) alongside model argon profiles (dashed lines) from the hexapole raytracing model. The black dashed line is modelled using the nominal aperture radii from machine construction, the red dashed line uses an artificially smaller aperture to constrain the profile. D) Methane experimental profile (Black X's) alongside model profiles for methane with beam velocities of 1150ms^{-1} and a lower velocity 800ms^{-1} (blue), employing the same aperture constraints as the red dashed line in C.

Two observations may be taken from Figure 3.6.4 A, firstly, the methane profile is narrower than the argon profile and secondly, both the argon and methane profiles are displaced from the laser centre. The first observation is good initial evidence for magnetic focussing of the methane beam, comparisons of the methane profile to models being displayed in later subfigures. The second point requires further consideration. Figure 3.6.4 B displays gaussian fits to the experimental data of Figure 3.6.4 A. These fits reveal the centres of both distributions to be displaced not only from the laser's centre, but also from each other. The centre of the laser was identified by eye in a dark room, the observed maximum displacement of a profile from this centre being 0.2mm (for argon). With the displacement being on the order of the step size used in measuring the profiles, and the identification method for the laser centre being subjective based on the user's eyesight it is difficult to comment on the difference in alignment other than that some misalignment (equating to ~10% of the final beam diameter) was observed. The shift in centres between the two profiles is more interesting.

The argon beam, being unaffected by the magnetic focussing properties of the lens, is expected to produce its maximum along the centre of the line of sight through the machine from the nozzle to the point measured. The shape and centre of the argon profile are therefore solely properties of the geometry of the machine. The methane beam is subject to the same geometry as the argon beam, but with the added effect of magnetic focussing within the hexapole. The displacement between the argon and methane beams therefore indicates a misalignment of the magnetic lens focus from the centreline of the machine. The fit gives a displacement of 0.07mm between the argon and focussed methane beams at the second flag. This is equivalent to a divergence of 0.0053° at the exit of the hexapole and a maximum displacement of 0.13mm at the position of the deposition surface. This displacement is an order of magnitude smaller than the ~2mm radius of the spots created by both the laser and focussed components of the methane beam (Figure 3.5.3 C, Purple and Green). It can be concluded that the laser still serves as a human-visible indication of the path of the beam. The mismatch in propagation angle between neutral particles ($m_i = 0$) and magnetically sensitive particles ($m_i \neq 0$) has been accounted for in later models of the methane beam.

Figure 3.6.4 C compares the experimental argon profile (green x's) to simulated profiles from the hexapole model (dashed lines). The black dashed line was modelled using apertures matching the nominal values of those in the machine itself. The resultant model profile (black dashed lines) can be seen to be wider than the experimental argon profile. Given argons lack of sensitivity to magnetic focussing, this indicates a difference in beam geometry between the model and experiment, most likely arising from the misalignment discussed in the previous paragraph. An artificially narrower aperture was introduced to the model, its radius being adjusted until a minimum in the root-mean-square-residual (RMSR) between model and experiment was found. The result is plotted as the red dashed line in Figure 3.6.4 C, this is seen to be a much better fit to the experimental data.

It is important to note that the modelled argon profile with the artificial aperture is still wider than the experimental methane profile, implying that the introduction of the

artificial aperture should not adversely affect the accuracy of models of methane, the beam diameters of the focussed states being sufficiently small to pass through the aperture unmolested.

With the model confirmed to be capable of simulating a neutral profile it may now be employed to produce models of the methane beam. Figure 3.6.4 D displays the experimental methane data (black x's) alongside two models of the methane beam at different mean velocity (v_∞) values. A range of velocities were tested, with the displayed velocities of 1150ms^{-1} (red dashed line) and 800ms^{-1} (blue dashed line) seen to bound the experimental profile. It stands to reason that a best fit model profile with a velocity between the bounding values must exist.

Another variable to consider while searching for this best fit velocity is the velocity distribution of the beam. While in a perfect supersonic expansion the velocity of all particles in the beam would be v_∞, real expansion typically exhibits some velocity distribution, the width of said distribution being relatable to the degree of cooling within the molecular beam. To account for this the velocity of each simulated particle in the model is sampled from a normal distribution centred on v_∞, with a standard deviation equal to some fraction of v_∞. This fraction was given an upper bound of 20% to ensure it remains smaller than the Maxwell-Boltzmann distribution of velocities expected at thermal equilibrium. Both model profiles displayed in Figure 3.6.4 D had a standard deviation of 10% of their v_∞.

In the remainder of this section models will be discussed in terms of "effective nozzle temperature" (T_{NE}). The v_∞ values of said models are calculated using (Eq. 3.4.1), the gamma value at a given temperature being estimated from the equations laid out in section 2 of [47]. The velocity distribution then being crudely using a fraction of v_∞ as laid out in the previous paragraph. An inherent flaw in this method is the fact that any beam with a non-zero velocity distribution must not have undergone complete rotational cooling, and v_∞ must inherently be lower than would be predicted by (Eq. 3.4.1). Hence referring to each model by the "effective" nozzle temperature required to produce its v_∞ from (Eq. 3.4.1).

Model profiles were run for nozzle temperatures above and below 0°C (believed to represent the real nozzle temperature) and velocity distributions with standard deviations between 0.05 and 0.2v_∞. Figure 3.6.5 displays the RMSR value between these models and the experimental methane profile in heatmap form. Low values (lighter colours) indicate a better fit to the data. The minimum value is observed to lie at an effective nozzle temperature of -40°C and standard deviation in velocity distribution of 0.05v_∞.

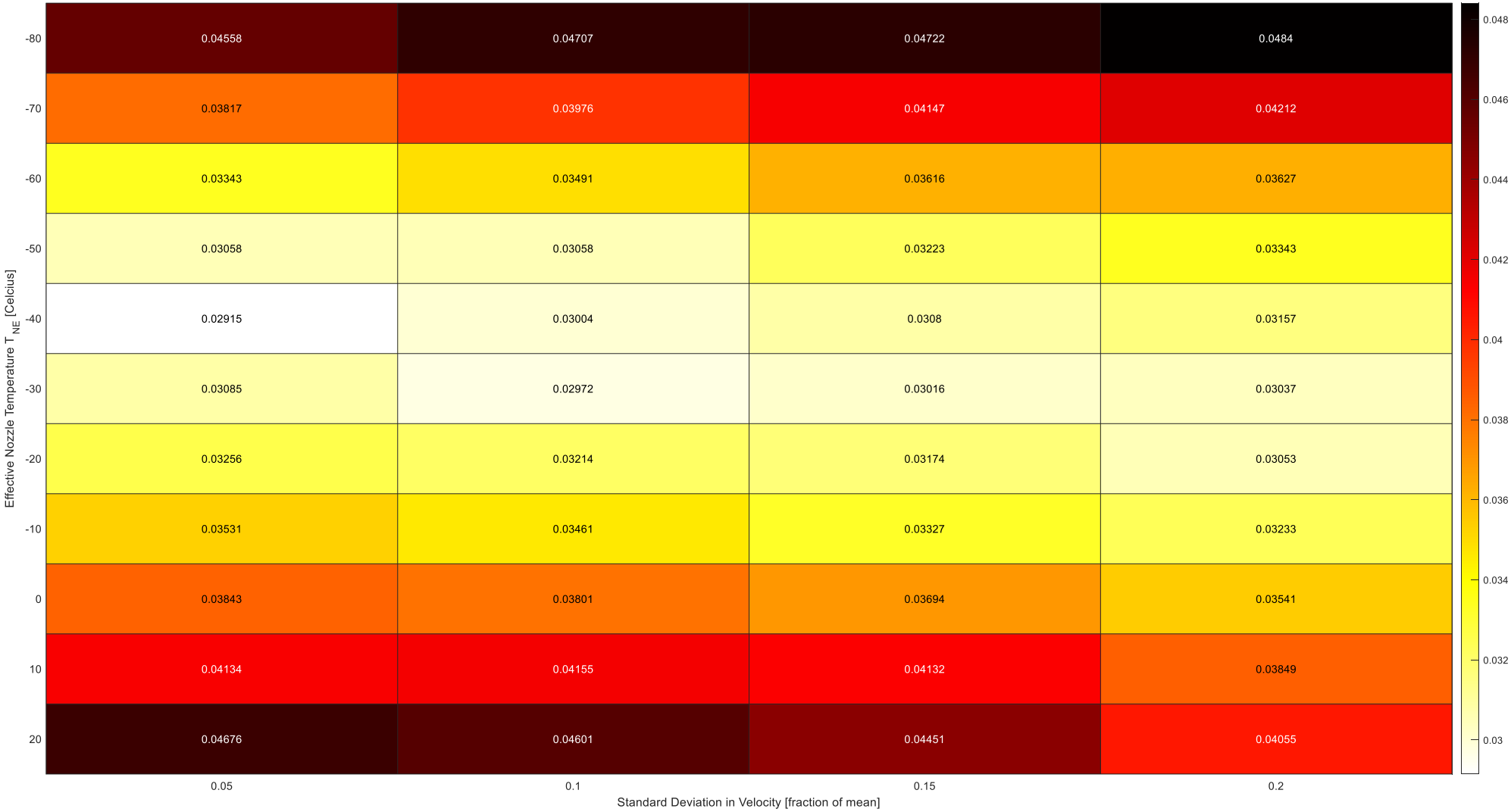

Figure 3.6.5: Heatmap of RMSR values between model and experimental methane profiles for a range of effective nozzle temperatures and standard deviations in nozzle temperature. The minimum is observed to lie at an effective nozzle temperature of -40°C and standard deviation in velocity of 0.05 the mean velocity.

RMSR can be seen to vary more noticeably as a function of T_{NE} than standard deviation in velocity distribution. The best fit temperature being well below the perceived temperature of the nozzle at -40°C suggests that the nozzle is actually colder than was believed, or that rotational cooling of the beam was far from complete. Inability to validate the beam temperature experimentally relates to why Figure 3.6.5 does not display a clear minimum in RMSR with respect to standard deviation in velocity (indicative of velocity distribution breadth). The NMR apparatus does not have a way of accurately measuring beam velocity (and therefore estimating the velocity width), but velocity measurements on the magnetic molecular interferometer (the groups other apparatus[33]) for a variety of seeded beams and comparable nozzles/pressures, have never evidenced velocity distributions with a standard deviation of less than 5% of the mean velocity in the beam, results were therefore truncated at 5%.

The primary reason for modelling the beam in the first place is to enable extraction of the average polarisation. Both to allow comparison to polarisation in a thermal equilibrium sample of methane, and to identify the flux of polarised protons reaching the surface, a number of which will inform the measurement structure for a hyperpolarised deposition experiment. Figure 3.6.6 displays the average polarised protons per molecule (equal to twice the average polarisation) arriving at the deposition surface for the models displayed in Figure 3.6.5, again in heatmap form. For the purposes of the hyperpolarised experiment higher values (lighter colours) are better. Again, the stronger trend is seen in effective nozzle temperature as compared to width of velocity distribution. In general, polarisation increases with decrease in temperature and width of velocity distribution.

Notably, the best fit profile (-40°C, $0.05v_{\infty}$) does not provide the highest average polarised protons per molecule arriving at the surface. The difference between the best fit value and the highest modelled polarisation is ~15% of the best fit value, while the difference between the best fit, and what would have been the first guess model (0°C, $0.01v_{\infty}$) is ~11% of the best fit value. To obtain a flux of polarised protons at the surface, the average polarised protons per molecule is to be multiplied by an estimated flux (calculated in the next section). This estimated flux is itself dependent on pressure measurements using gauges know to generally exhibit errors in absolute pressure measurement of up to 30%. This being at least twice the maximum variation in modelled polarised protons per molecule suggests taking the value from the best fit should at the very least not introduce greater error into the estimation than was already present. The average polarised protons per molecule value taken from the beam profiling experiments is therefore 0.9516.

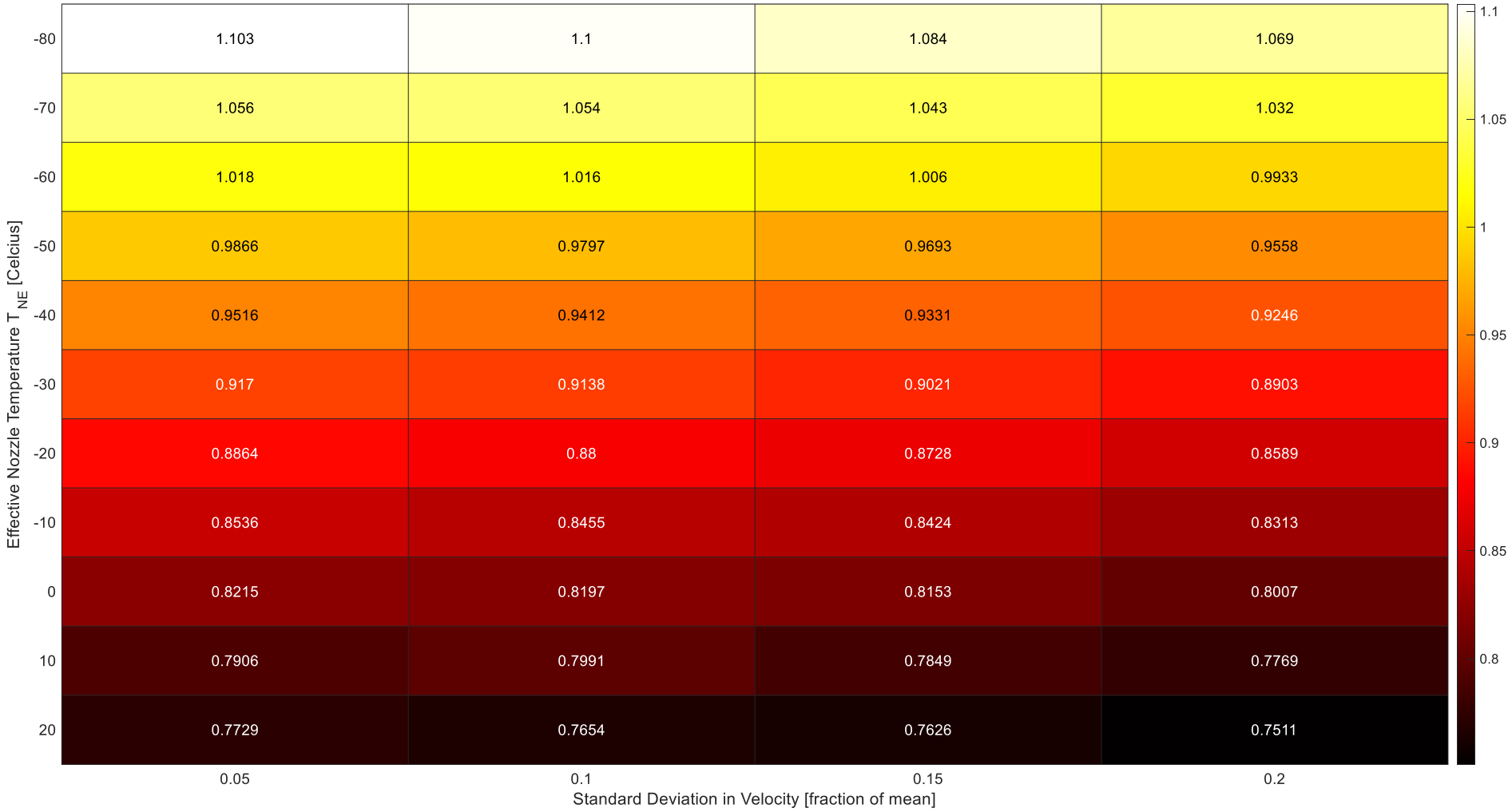

Figure 3.6.6: Heatmap of average polarised protons per molecule arriving at the deposition surface for the model profiles presented in Figure 3.6.5. Equivalent to twice the average polarisation of the profile. Polarisation is seen to increase with decrease in effective nozzle temperature, and decrease with widening velocity distribution.

Estimation of Beam Flux and Final Polarisation:

To convert the average polarised protons per molecule calculated in the previous section to a flux arriving at the surface the molecular flux of the beam must also be calculated. Said flux may be calculated by comparing the pressure in the beam profiling section of the machine when the beam is passing freely, with the pressure when the beam is completely blocked.

The first step is to calculate the pipe conductance (C_{pipe}) from the point the pressure is measured (the cold cathode gauge) to the inlet of the vacuum pump, this is given[51] as:

$$C_{pipe} = \frac{C_L}{1+\frac{C_L}{C_0}} \quad \text{(Eq. 3.6.1)}$$

C_L and C_0 represent the two limiting case conductance's of a pipe with length (L) >> diameter (D) and an aperture ($L = 0$) these may be calculated via:

$$C_L = \frac{D^3}{L}\sqrt{\frac{2\pi RT}{M}} \quad \text{(Eq. 3.6.2)}$$

$$C_0 = \sqrt{\frac{2\pi RT}{M}}A \quad \text{(Eq. 3.6.3)}$$

Where R is the gas constant, T is the temperature, M is the molar mass of the gas in question and A is the aperture area. The value of C_{pipe} may then be combined with the known pumping speed (S^*) of the turbo pump on the beam profiling section to calculate and the pumping speed (S) at the pressure gauge via:

$$S = \frac{S^* \times C_{pipe}}{S^* + C_{pipe}} \quad \text{(Eq. 3.6.4)}$$

The molecular flux (Φ_m) corresponding to the pressure increase (ΔP) at the gauge when the beam is blocked may then be calculated as:

$$\Phi_m = \Delta P \times S \quad \text{(Eq. 3.6.5)}$$

Inputting the measured pressure difference of $2.5\text{x}10^{-7}$ Pa, the pipe diameter of 32mm, the pipe length of 290mm and pumping speed of the pump (Pfeiffer hiPace80) at $67\text{x}10^{-3}$ m^3s^{-1} gives a Φ_m value of $7.92\text{x}10^{11}$ molecules per second. This is the molecular flux at the scanning aperture, as a final step this flux must be adjusted to reflect the number of molecules which make it to the surface. This may be achieved through multiplication with a simple constant taken from the hexapole model, representing the fraction of surviving particles at the scanning flags that land on deposition surface, this is 0.9721 for the best fit profile. Accounting for this and multiplying by the polarised protons per molecule of 0.9515 determined earlier gives a flux of polarised protons ($\Phi_{Polarised}$) striking the deposition surface of: $7.32\text{x}10^{11}$ polarised protons per second.

Section 3.7: The deposition target and NMR probe:

The deposition target underwent multiple iterations between the four attempted hyperpolarised depositions due to efforts to minimise coil arcing. Three of the four attempts were conducted with a flat sapphire window as the target, with the final experiment employing the taller, stepped, top-hat shaped sapphire used in the H_2O@Ar experiments. Figure 3.7.1 displays the two sapphires as mounted to the end of the cold finger.

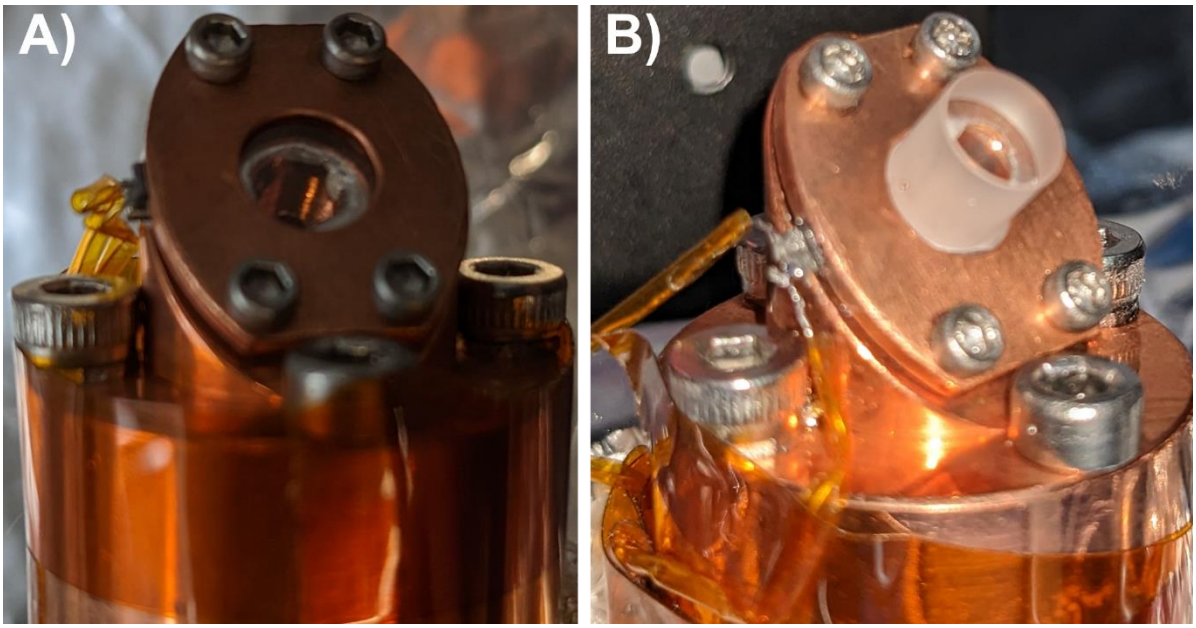

Figure 3.7.1: Images of deposition surface mount containing, A**:** the flat sapphire window and B: the top hat shaped sapphire. The exposed surface of the sapphire window has a diameter of 6mm, while the diameter of the polished upper surface on the top hat shaped sapphire is 5.5mm, the surface projecting 5mm above the upper surface of the copper retaining plate. To the left of the sapphire in both images the wires leading to the Cernox temperature sensor may be seen.

No significant differences in NMR characteristics for macro-deposited samples were noted following the change in sapphire, results in the following sections will be presented without reference to the specific target used.

While for the H_2O@Ar measurements presented in Chapter 2 the stepped sapphire was used alongside an NMR coil directly attached to the cold finger, the NMR coil for the hyper-polarised experiments presented below was instead attached to the macro-deposition nozzle. This was again an attempt to minimise coil arcing, allowing the coil position above the surface to be adjusted. Further to this, a PTFE shroud was introduced to the coil for the first three hyperpolarised experiments. Figure 3.7.2 provides a photograph of the complete nozzle and coil assembly alongside a circuit diagram.

The matrix gas for the hyperpolarised depositions was again argon. This could be provided either from the macro deposition nozzle (backing pressure 50mbar), depositing directly through the coil onto the sapphire, or via an external leak valve adjusted until a $1x10^{-6}$ mbar pressure rise was seen in the bore.

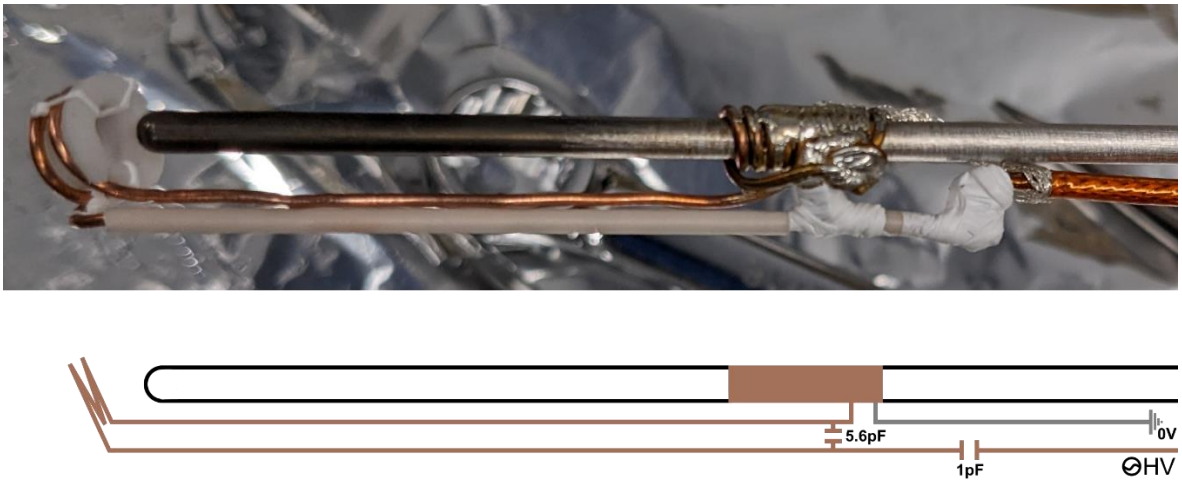

Figure 3.7.2: Photograph of nozzle-coil assembly with accompanying circuit diagram. High voltage AC is provided along the central line of a vacuum compatible coaxial cable. The grounding outer layer of the cable is connected directly to the ground side of the NMR coil. Two capacitors are present, insulated with PTFE tape. The coil has two complete turns with an inner diameter of 6mm. A hollow cylindrical PTFE shroud (5mm bore diameter) is present secured inside the coil.

Before starting a hyperpolarised deposition, the alignment of the beam with the surface was checked. The laser was passed down the beam line and the illumination of the sapphire was observed via a fibre-optic feedthrough into the bore. While the fibre-optic also allowed for illumination of the surface with a white light source, and subsequent photographing of the surface, the laser was typically only visible to the camera with the white light off. Figure 3.7.3 shows an example pair of images with the laser on, A shows the surface mount with the lighting on, B with the lighting off and the sapphire illuminated by the laser. A red circle has been placed over the edge of the fibre-optics field of view in both images as a visual aid.

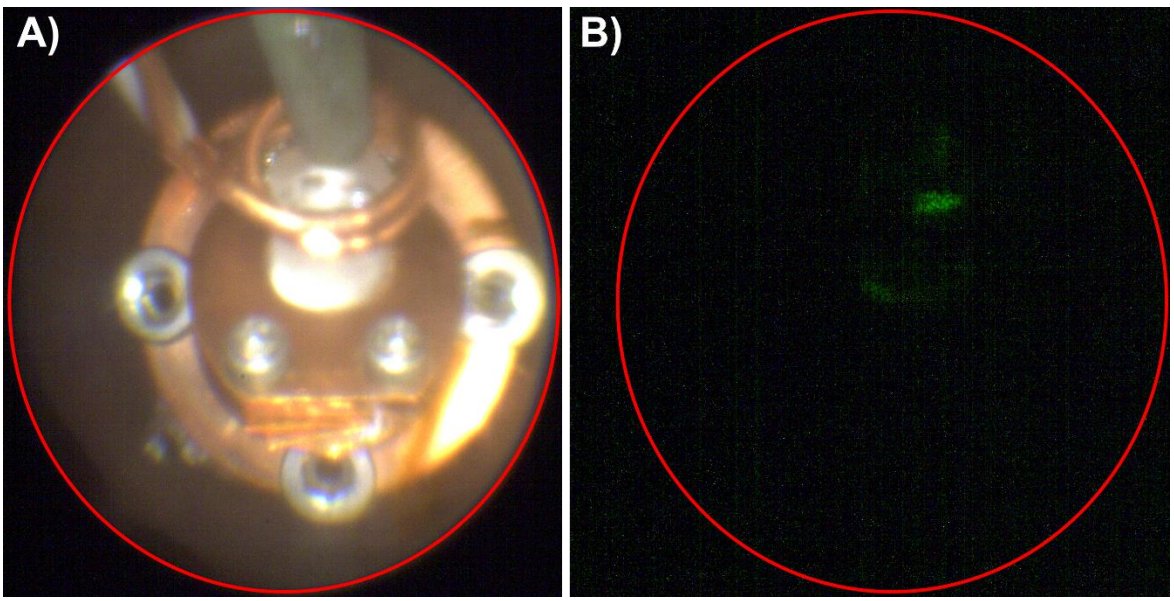

Figure 3.7.3: Images of the deposition surface illuminated by the laser, with (A) and without (B) additional illumination. A red circle is superimposed over both images showing the edges of the field of view of the fibreoptic. The position of the green spots in B are seen to overlay the sapphire in A.

Section 3.8: Designing HPD measurement Sequence:

As was the case for the water NSC measurements, design of a suitable NMR measurement structure for the hyperpolarised deposition requires some understanding of the NMR characteristics of methane in an argon matrix. Exploratory work using the macroscopic deposition nozzle found a concentration of ~6% methane in argon to provide easily detectable reproducible samples. This does mean that the designed sequence relies on ~6% samples having similar NMR characteristics to the much lower concentration samples expected in HPD. A necessary assumption without the benefit of an already measured hyperpolarised sample to optimise against. Argon pressures used in the HPD attempts will be kept inline with those used for macroscopic depositions, with macroscopic measurements working on the assumption that the majority of NMR signal is coming from methane isolated as a monomer (as was the case for water).

Macroscopic Deposition Procedure:

Figure 3.8.1 displays the modified gas handling system for macroscopic methane depositions. Changes from Figure 2.3.2 include replacement of the water ampule with a methane transfer cylinder and introduction of an O_2 trap between the regulator and nozzle isolation valve. Before use the gas lines up to the nozzle isolation valve were purged and pumped 3 times with 800mbar argon. After pumping again, the mixing cylinder was filled to 50mbar pure methane and then diluted with pure argon to 800mbar. Both gasses used were rated 99.999% pure research grade quality.

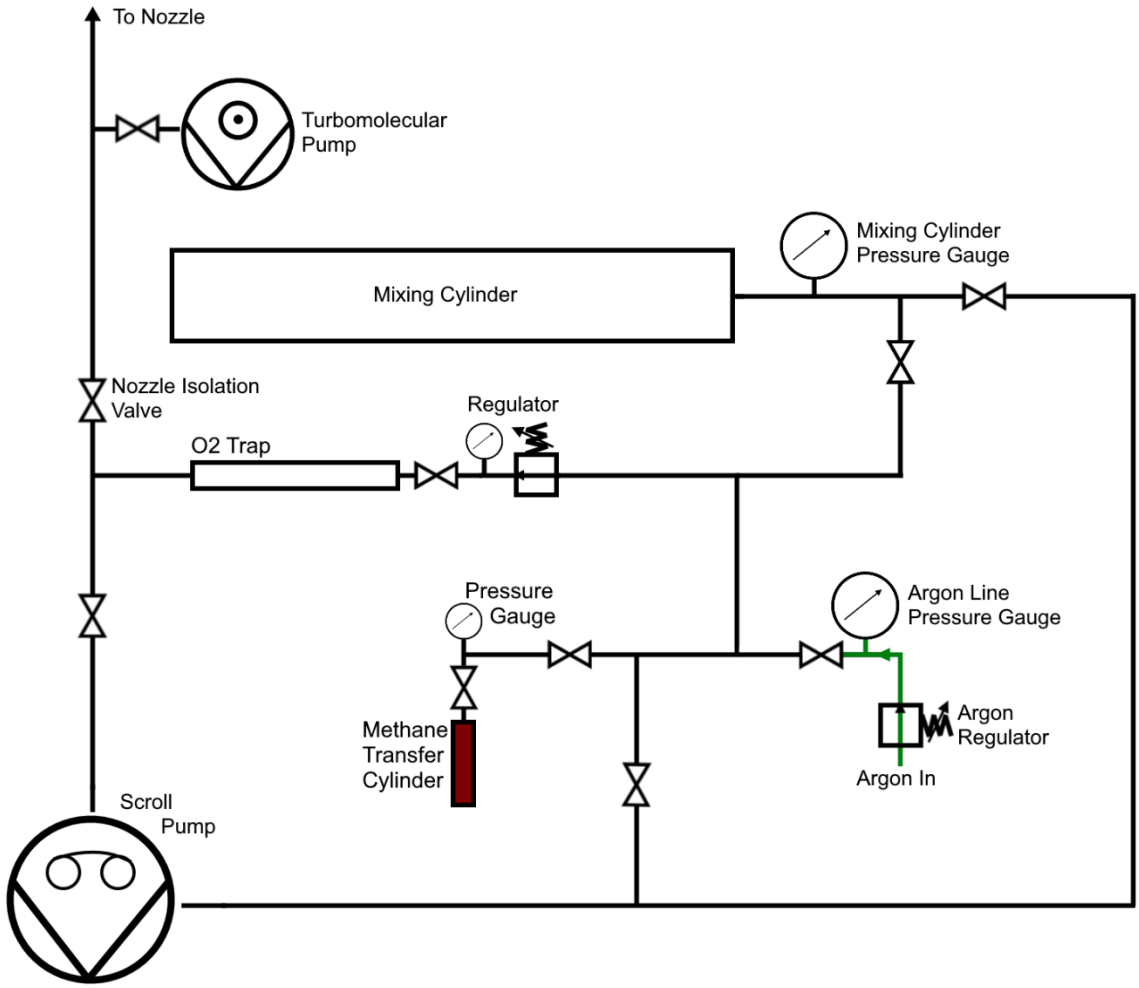

Figure 3.8.1: Diagram of the gas handling system for macroscopic methane depositions. Changes from Figure 2.3.2 include replacement of the water ampule with a connection for the methane transfer cylinder, and insertion of an O2 trap between the regulator and nozzle isolation valve.

The diluted mixture would then be fed into the O_2 trap via the regulator to a pressure of 500 mbar. The valve between the O2 trap and regulator would be closed and the O_2 trap opened to the nozzle for the duration of the deposition (30 minutes). Deposition was performed with the sample heating turned off, the temperature reading for the sapphire substrate reading between 5 and 6 Kelvin.

Acquisition window size: T_2^*:

T_2^* is of interest to determine the appropriate acquisition window duration for the experiment. For CH_4@Ar samples T_2^* was determined by fitting a single exponential the free induction decay of the sample following a 90° pulse. Figure 3.8.2 provides an example of such a fit.

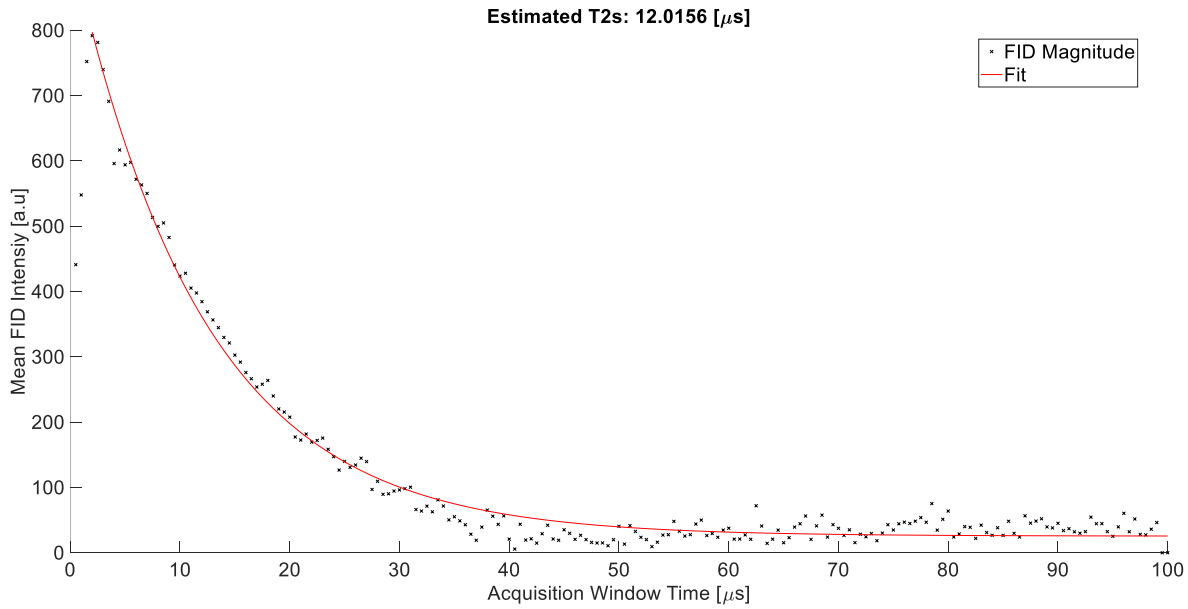

Figure 3.8.2: Example $T2^*$ fit to the magnitude of an FID measurement on a ~6% CH_4@Ar sample. The extracted value of $T2^*$ for this sample was 12μs. The simple single exponential fit is seen to underestimate the data in the region between 10 and 20μs as well as the region between 70 and 100μs. Overestimation is evident between 30 and 50μs.

The overall quality of the fit to the data is poor, both under and overestimating the data across the duration of the acquisition window. This can be expected as there is no apriori reason for the decay to follow a simple exponential form. Nevertheless, the insight into the signal decay rate is sufficient to determine a sensible maximum window size. The observed T_2* of the sample was 12μs. Across 8 measurements for samples deposited at 5K the average T_2^* was 9.43μs with a standard deviation of 1.23μs. An acquisition window of 100μs (such as that used in the T_2^* measurement) is therefore more than sufficient to capture the entirety of the usable signal. Shorter windows are possible with the Redstone apparatus, but would involve either shortening the time between pulses, increasing the duty cycle of the coil and increasing the risk of arcing and unwanted sample heating, or padding of the time either side of the acquisition window with the risk of missing the echo maximum. A 100μs window avoids these issues and was carried forward for the hyperpolarised measurement. No change in T_2^* was observed with changes in sample temperature from 5 to 30 Kelvin.

<u>Measurement repetition rate: Measuring T_1:</u>

The signal available in a single hyperpolarised measurement is a product of three competing factors, the number of hyperpolarised spins deposited, how many of said spins have relaxed to thermal equilibrium over the deposition time and the thermal equilibrium signal that has arisen from spins deposited in previous measurement periods. The latter two of these components require an understanding of T_1. To measure this, the 6%CH_4@Ar sample was subjected to a spoiler pulse train, followed by a variable recovery time, measurement pulse sequence and acquisition. The resultant signal was plotted against recovery time and fit to (Eq. 1.5.3).

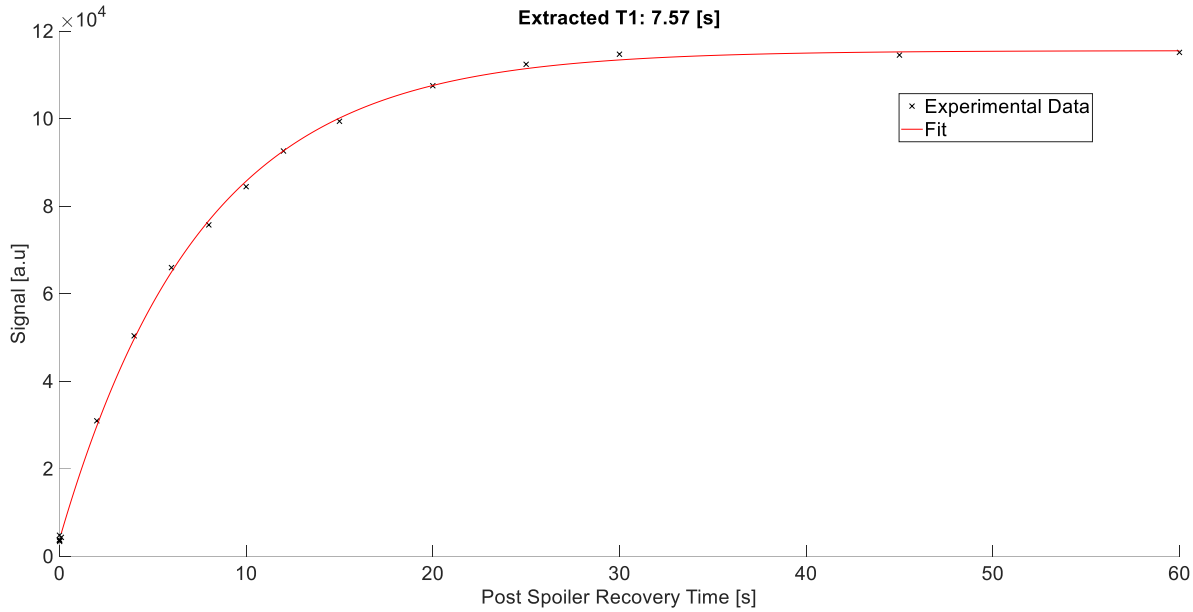

Figure 3.8.3: Example of a T1 measurement on a ~6% CH_4@Ar sample. The observed T1 from this experiment was 7.57s.

The extracted value of T_1 varied significantly from sample to sample. Over 16 samples the mean T_1 was 13.13s, with a standard deviation of 4.9s. Unlike in the case of water the nozzle temperature is not believed to be low enough for significant condensation to occur, this rules out differences in concentration caused by as a source of variance in T_1. The only remaining known difference between depositions would be in the nozzle-surface distance and positioning. While the exact shape of the distribution of gasses exiting the nozzle is not know it is not expected to be isotropic, and variance in the surface to nozzle distance and angle could lead to more rapid / slow sample growth and variance in the quality of the argon crystal. Such variations are partially evidenced by T_1 measurements were taken at different temperatures. In one run the sample was brought from 5 to 20K in steps, T_1 increasing with each temperature increase from an initial value of 13 seconds to a final value of 25 seconds. The increased T_1 of 25 seconds was noted to persist following subsequent cooling back to 5 Kelvin. This change in T_1 may is attributable to a permanent change of the sample with heating, possibly due to annealing. Regardless of the specific origin of the change, T_1 is clearly sensitive to small differences in conditions between different deposition despite best efforts to keep conditions identical.

<u>Measurement Repetition Rate: Modelling the Signal:</u>

The final value for the repetition rate (from here denoted as t_{dep}) was placed at 20s. This being the closest value to T_1 that was feasible bearing in mind the practical requirements of physically moving around the apparatus and manually operating it during the experiment, while ensuring that any changes fell in time with the appropriate section of the measurement sequence. The remainder of this subsection will model the impact of this decision on the expected signal.

The first element to consider is the amount of signal available due to hyperpolarised spin in a single measurement. The relevant flux here is $\Phi_{Polarised}$ as introduced at the end of Section 3.6. To a first approximation there are two components to

consider here, the growth of hyperpolarised signal due to the beam, and the loss of hyperpolarised signal due to relaxation, which is inversely proportional to T_1. The hexapole focuses spins with projection aligned antiparallel to the beam, denoting the number of these spins as a function of time as $N_{\downarrow}(t)$ and considering an infinitesimal deposition time dt, the change ($dN_{\downarrow}(t)$) in $N_{\downarrow}(t)$ may be modelled as:

$$dN_{\downarrow}(t) = \Phi_{Polarised}dt - \frac{1}{T_1}N_{\downarrow}(t)dt \quad \text{(Eq. 3.8.1)}$$

Dividing through by dt gives an ordinary differential equation of the form:

$$\frac{dN_{\downarrow}}{dt} = \Phi_{Polarised} - \frac{1}{T_1}N_{\downarrow} \quad \text{(Eq. 3.8.2)}$$

The solution to which is:

$$N_{\downarrow}(t) = T_1\Phi_{Polarised}\left(1 - \mathrm{e}^{-\frac{t}{T_1}}\right) \quad \text{(Eq. 3.8.3)}$$

The value of $N_{\downarrow}(t)$ for a given t_{dep} is the maximum number of hyperpolarised spins available to measure in a given measurement. Figure 3.8.4. plots this solution taking $T_1 =$ 13.13s and time in terms of fraction of T_1. The number of spins is seen to asymptotically approach a maximum around 9.3x10^{12} as t increases. Roughly 70% of the asymptotic value is reached by $1T_1$ with much of the remainder being recovered by the point growth near-plateaus at $5T_1$. The ideal measurement would therefore repeat, at minimum, every $1T_1$, with longer times providing ever decreasing gains in single-measurement SNR. In the case the signal is to be averaged, $1T_1$ is ideal, providing the best signal-per-measurement when simultaneously maximising the number of measurements per unit time to be averaged.

Assuming the T_1 of the hyperpolarised sample is the same as for the 6% sample then, in the limit of a single measurement, there is no downside to setting t_{dep} = 20s. For averaged measurements there will be a decrease in the number of averages per unit time but being at a value of t_{dep} greater than $1T_1$ is preferable to a lower one.

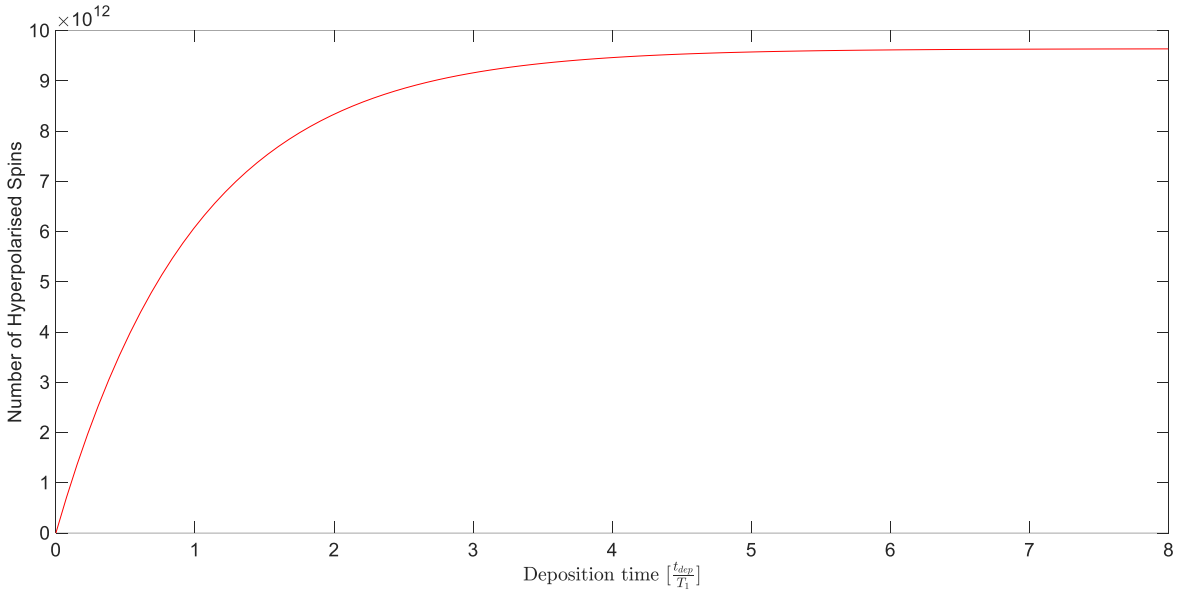

Figure 3.8.4: Plot of number of hyperpolarised spins $N_{\downarrow}$ vs deposition time (as a fraction of T_1). The number of hyperpolarised spins asymptotically approaches a value in the range of 9.3x10^{12}.

One feature (Eq. 3.8.3) does not account for is what happens to the spins that are no longer hyperpolarised. For a group of protons, which have a positive gyromagnetic ratio, the net magnetisation at thermal equilibrium inside a magnetic field will align with that field. This implies that any thermal equilibrium spin which arises will be oriented antiparallel to the hyperpolarised spin, actively negating it.

Rigorously determining the number of thermal equilibrium spins at time t would require solving a separate differential equation. This is expected to be a small number, as the time each spin has to relax to thermal equilibrium is at most t_{dep}, with most spins having less time as their arrival time is evenly distributed across the deposition window. Further to this the total number of spins considered is very small, being equal to the proton flux (Φ_{Proton}) which is 4 times the molecular flux of the beam, multiplied by the total deposition time t_{dep}. Before attempting the rigorous solution, we can first consider a scenario where all protons arrive at the start of the 20s window, this must inherently be larger than the rigorous solution as the average time for relaxation is longer. In this case we may fall back on the accepted formula for T_1 processes (Eq. 1.5.3) to get the number of protons that are at thermal equilibrium. Multiplying this by the expected population difference $\frac{P(\uparrow)-P(\downarrow)}{P(\uparrow)+P(\downarrow)}$ (Section 1.4) to get the maximum number of protons ($N_{\uparrow,max}$) that could be subtracting from our signal. The resultant equation takes the form of Eq 3.8.4:

$$N_{\uparrow,max}(t_{dep}) = \frac{1}{2}\,\frac{P(\uparrow)-P(\downarrow)}{P(\uparrow)+P(\downarrow)}\,\Phi_{Proton}\,t_{dep}\left(1-e^{-\frac{t_{dep}}{T_1}}\right) \qquad \text{(Eq. 3.8.4)}$$

The factor $\frac{1}{2}$ accounting for maximum magnitude of the spin vector of a single proton. Substituting in the relevant values from Section 3.6, taking T_1 as 13.13s and t_{dep} as 20s gives $N_{\uparrow,max}(20) = 2.94\text{x}10^{10}$. The value of $N_{\downarrow}(20)$ meanwhile is 7.54x10^{12}. This indicates that, even when overestimating the maximum time for relaxation, within a single measurement $N_{\uparrow,max}$ is less than 1% of $N_{\downarrow}$ and can be safely neglected.

Where it may become an issue is later in an experiment after a significant number of measurements. The maximum runtime for the methane beam without refilling is ~45minutes. At a repetition rate of 20s, this is a total of 135 measurements. The measurement sequence is intended to contain a spoiler pulse chain that randomises the orientation of all present spins immediately before the deposition window begins. Neglecting any thermal equilibrium spin that arises from molecules deposited during this window, the number of proton spins to consider is the fraction of all previously deposited protons that return to thermal equilibrium within the deposition window. These protons are all present at the beginning of the window with their spin orientation randomised and may be addressed using the same procedure as for (Eq. 3.8.4). The experiment is modelled as discrete in the time domain, such that $t = nt_{dep}$ where n is an integer. The net thermal equilibrium spin arising at measurement n due to previously deposited protons is then:

$$N_{\uparrow}(t = nt_{dep}) = \frac{1}{2} A \Phi_{Proton} (n-1) t_{dep} \left(1 - e^{-\frac{t_{dep}}{T_1}}\right) \quad \text{(Eq. 3.8.5)}$$

Where $A = \frac{P(\uparrow) - P(\downarrow)}{P(\uparrow) + P(\downarrow)}$. The total number of measurable protons at $t = nt_{dep}$ spins is therefore:

$$N_{net}(t = nt_{dep}) = N_{\downarrow}(t_{dep}) - N_{\uparrow}(t) \quad \text{(Eq. 3.8.6)}$$

Before plotting this, it is important to consider how the number of spins relate to signal from the NMR probe. Ideally these factors would be related by taking calibration measurements with macroscopic samples of CH_4@Ar with known numbers of spins. Accurately estimating the number of spins within a macroscopic deposition is difficult. While the total amount of molecules which stick to the cold finger per unit time can be estimated from the pressure difference observed when gas is introduced to the bore with the cooling on versus when the surface is at room temperature (no sticking) it is not possible to determine where on the cold finger the sticking is occurring. The NMR probe is only sensitive to a small area at the end of the cold finger, assuming all particles stick within this region would lead to a massive overestimation. Similarly, while the amount of methane present within the sensitive region of the probe could be estimated from the sample dimensions, said samples tended to have transparent regions and were difficult to assess visually.

A workaround is to use a calibration sample of a material with similar NMR characteristics to methane and more easily assessable proton content. The best candidate tested for this turned out to be the polymer polyether-ether-ketone (PEEK). At room temperature this was observed to have a T_2^* on the order of 10μs, with comparable T_1 and T_2 to the 6% methane. PEEK is a solid at room temperature, a sample was cut from a 5mm diameter machine stock rod and its mass measured with an electronic balance. Measurements of single echoes were taken and their SNR calculated. The number of spins within the sample was estimated by comparing the mass of the sample to the mass of a single PEEK monomer, the estimated number of monomers in the sample was then multiplied by the number of hydrogen

molecules per monomer, giving an estimation of the proton count. Dividing this estimation by the SNR of the sample places the number of spins required to achieve an SNR of 1 using a single echo at: 1.1×10^{14} spins.

Plotting (Eq. 3.8.6) and dividing by this value gives Figure 3.8.5, a graph of the change in SNR over experiment time assuming the beam was switched on at t=0 and left on for the duration. For ease of discussion the x axis is given in terms of measurement number.

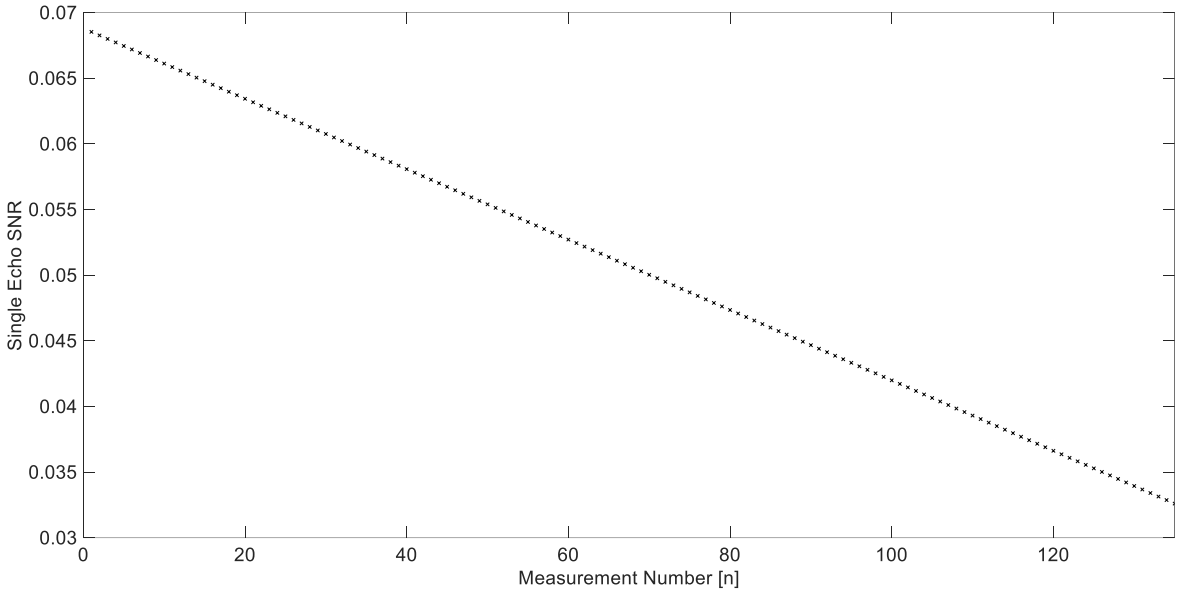

Figure 3.8.5: Model single echo SNR vs measurement number for a hyperpolarised experiment. The SNR is seen to decrease linearly as a function of measurement time. For the chosen inter-measurement time of 20s, the final plotted point at 135 measurements is equivalent to 45 minutes of continuous measurement. The maximum value at n=1 is 0.069, while the value at n=135 is 0.033. At n=90 (30 minutes runtime) the value is 0.045.

The first observation to take away from Figure 3.8.5 is that the single-echo SNR at all values of n is less than 1. The SNR starts at a value of 0.069, falling to 0.033 by 135 measurements (45 minutes). Practically, running the beam for a 30minute period, refilling the mixing cylinder and running the beam again makes more sense than running the beam for 45minutes at the risk of including data where the backing pressure of the source has become difficult to regulate. At 30 minute of deposition (n=90) the SNR is 0.045. Considering a 30 minute run the SNR is expected to fall to 35% of its maximum by the end of the run. The average SNR of a measurement within this period is 0.057.

The maximum achievable SNR averaging over 90 measurements with an SNR of 0.057 is ~0.54. This suggests that measuring the hyperpolarised deposition using a single echo sequence for 30 minutes would produce signal on the level of half the noise. The problem persists if we consider 60 minutes of deposition (two 30 minute periods). Here the average SNR falls to 0.044, averaging over 180 measurements producing a final SNR of ~0.6, a negligible increase.

The conclusion to be drawn here is that signal is unlikely to be observable on a level greater than the noise without additional averaging within each measurement. This

additional averaging could be provided by running an echo train, rather than a single echo. The feasibility of this is the topic of the next subsection.

As a final note (Eq. 3.8.6) can also be used to identify the total beam runtime required for the signal from thermal equilibrium spin to reach a level greater than the experimental noise. This is the value of n such that SNR < -1, and is equivalent to 3987 measurements, or 22.15 hours. Measurement of thermal equilibrium signal from the beam would be a good method for debugging alignment of the beam with the surface. For a single echo measurement, the total deposition time required for this renders it impractical.

T2:

With the repetition rate for the experiment largely being fixed by T_1 the question remains whether additional signal could be reaped via the application of an echo train. The viability of this depends on the T_2 of the sample. T_2 measurements were conducted using a single-echo measurement sequence with varied inter 90-180º pulse time. The signal at the resultant echo time was extracted, plotted and fit to a single exponential decay function. Example results from such a measurement are plotted in Figure 3.8.6.

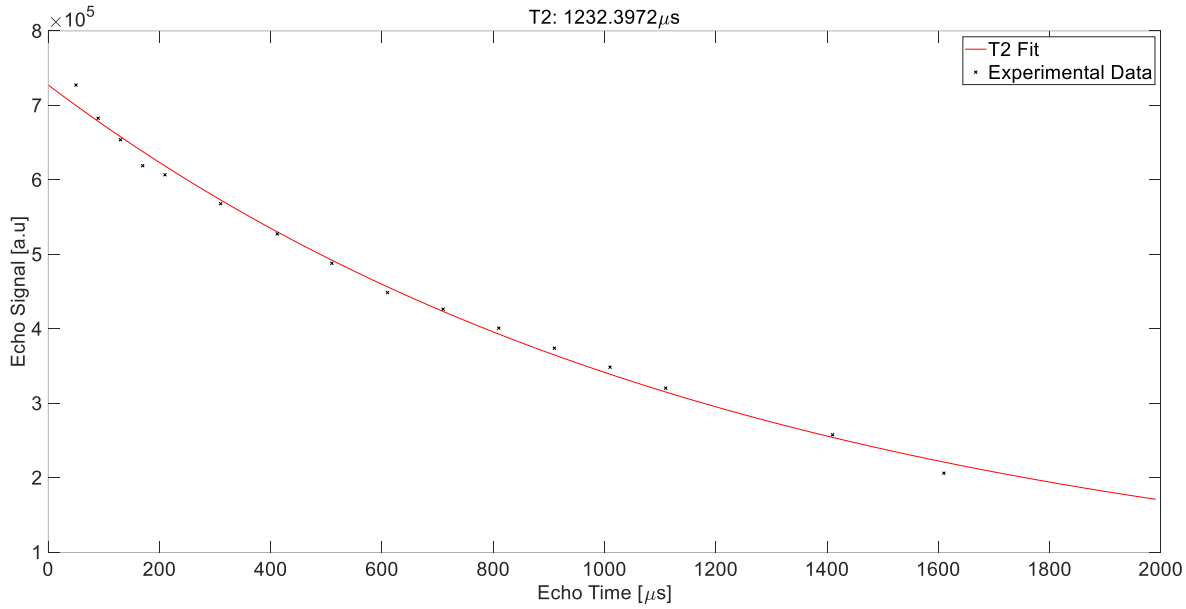

Figure 3.8.6: Example plot of the results of a T_2 measurement on a ~6% CH_4@Ar sample. T_2 for the sample was fit using a simple single exponential decay. The observed T_2 for this sample was 1232.4μs.

The observed T_2 for the sample displayed in Figure 3.8.6 was 1232.4μs. Overall the mean value of T_2 across 10 measurements at 5K was 1475.2μs with a standard deviation of 800μs. The large standard deviation is most likely attributable to three exceptionally low values of T_2 in the data set. Two of these are associated with the first sample deposited (187 and 214μs) while a third is associated with a sample that had been brought to 20K and then cooled (384μs). Notably, the pre-heating T_2 for this sample at 5K was 616μs. As was the case for T_1 it appears the T_2 of the sample is highly sensitive to both sample deposition and thermal history. At the low end of the measured T_2 values T_2 is on the order of a single acquisition window, while at the high end it is roughly 10 acquisition windows. This does not bode well for potential

echo measurements. Regardless, a CPMG type echo train measurement analogous to that used in the H_2O@Ar measurements was attempted. The train was 256 echoes long with the time between 180º pulses (and therefore the echo spacing) in the train being 120µs. The whole train was repeated 128 times for averaging purposes. The resultant echoes are plotted in Figure 3.8.7.

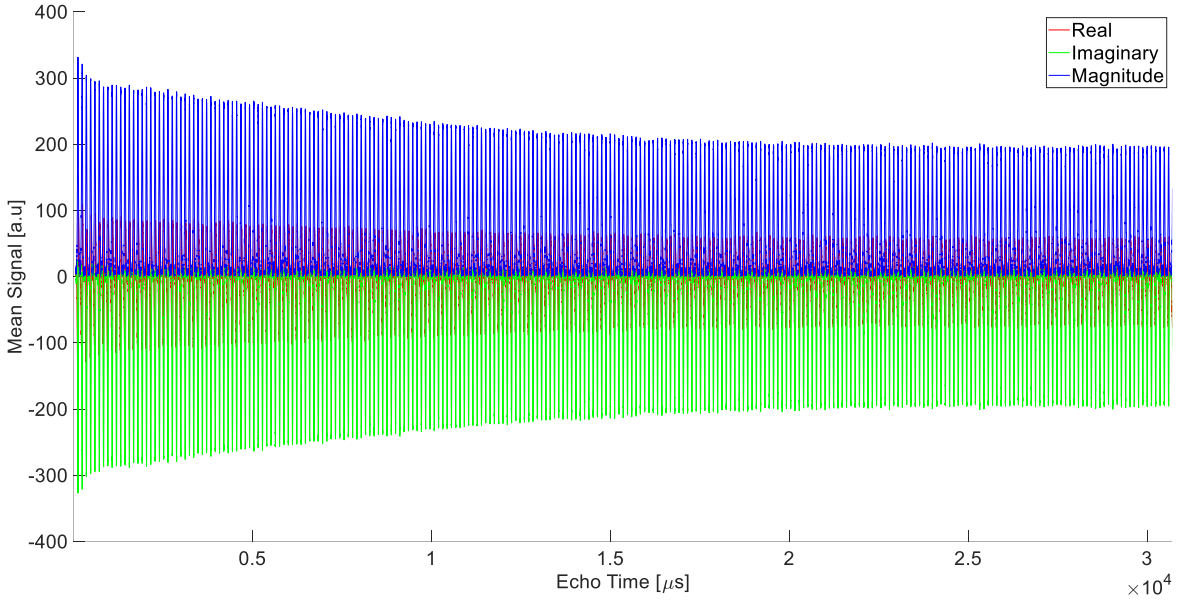

Figure 3.8.7: Real (red), imaginary (green) and magnitude (blue) components of signal from an echo train measurement averaged over 128 trains. The signal is noted to barely decay within the train, despite the overall length of the train being more than an order of magnitude greater than the largest observed value of T_2.

The total time spanned by the 256 echoes in Figure 3.8.7 is 30720µs, more than an order of magnitude greater than the largest observed T_2 for CH_4@Ar at 2450µs. Despite this extensive duration the signal is noted to have barely decayed at all by the end of the train.

This appears to be a reemergence of the CPMG extension effect previously observed for water. This is highly fortuitous as, despite the sample-to-sample variability observed in T_2 the presence of the CPMG extension effect was confirmed in all samples tested, allowing echo trains to be employed in the hyper polarised deposition (HPD) measurement for the purposes of averaging / SNR enhancement. The expected SNR of the final measurement structure is discussed in the next subsection.

<u>Chosen Hyperpolarised Measurement Structure:</u>

With the CPMG effect determined to be present the ideal pulse sequence for the hyperpolarised deposition is to be a CPMG type echo train measurement. The measurement will feature a spoiler pulse train, followed by a recovery time T_{rec}, a 90° excitation pulse (P1), pulse interval, and 180° measurement pulse (P2). After an appropriate wait the acquisition window will be placed to capture the centre of the echo, followed by another wait period. The 180° pulse/wait/window/wait section will be repeated N_{echoes} times, with the whole sequence then being repeated for the next measurement.

In diagram form this appears similar to the structure used for water measurements (copied forward as Figure 3.8.8). T_{rec} in this case is both the recovery and deposition time. For the previously discussed reasons this is set at 20s. The pulse durations and intensities for P1 and P2 are largely predetermined, being the shortest and closest to the desired tip angle pulses they can be while minimising arcing. The values of the wait times τ_1 and τ_2 are chosen to facilitate the 100μs (dictated by T_2*) acquisition window with minimal time between the acquisition pulse and centre of the first window. 50μs has been suitable in previous measurements. The value of N_{echoes} will be as high as possible. The maximum possible within the limits of the device memory is 256, though lower numbers have been used in the past to combat coil arcing.

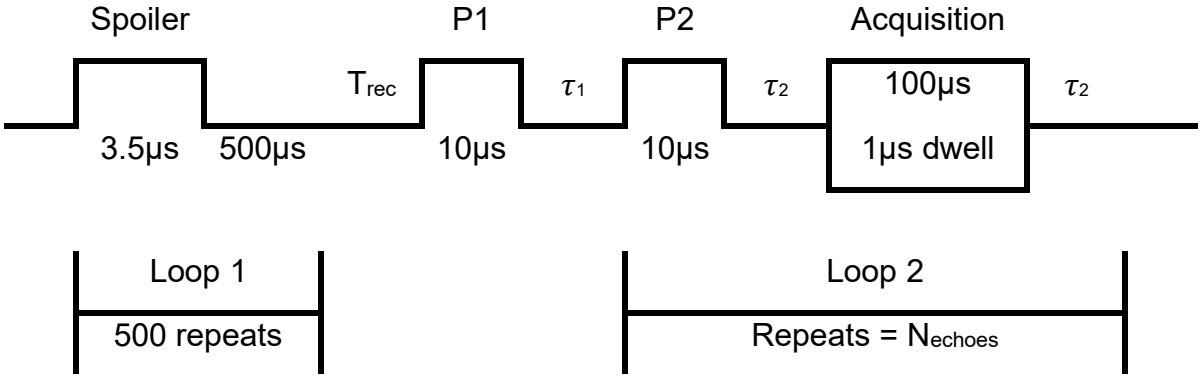

Figure 3.8.8: Diagram of pulse sequence. The key structure is identical to that presented in Figure 2.6.1, with the exception that the values of the pulse variables have changed (see text) and that no phase cycling is employed in this measurement.

The increase in SNR due to averaging over the echo train is at most a factor of $\sqrt{N_{echoes}}$. For 256 echoes this is a factor of 16. Multiplying the values in Figure 3.8.6 by this produces Figure 3.8.9.

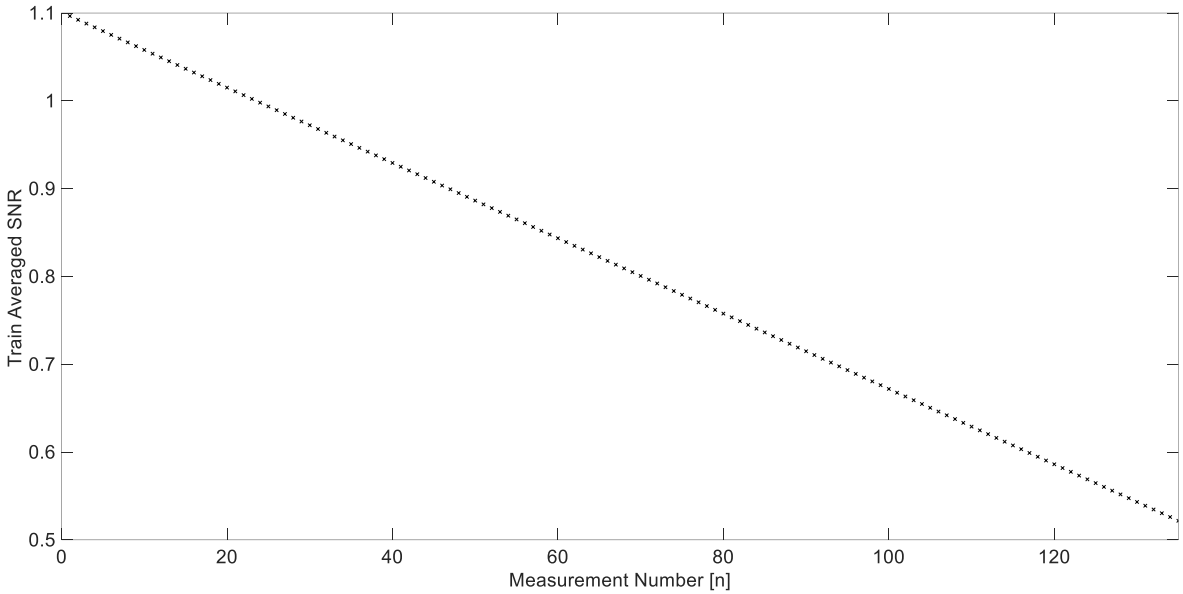

Figure 3.8.9: Model train averaged SNR vs measurement number for a hyperpolarised experiment using an echo train measurement with 256 echoes. The SNR is seen to decrease linearly as a function of measurement time. For the chosen inter-measurement time of 20s, the final plotted point at 135 measurements is equivalent to 45 minutes of continuous measurement. The maximum value at n=1 is 1.1, while the value at n=135 is 0.53. At n=90 (30 minutes runtime) the value is 0.72.

In this case the signal level starts above the level of the noise at an SNR of 1.1, falling to 0.72 by the 30 minute (90 measurements) mark. The average SNR of measurements in this period is 0.9057, averaging over all 90 measurements would give an SNR of 8.6. As a final note, the improvement in SNR places the deposition time required to measure thermal equilibrium signal at 490 measurements or ~2 hours and 42 minutes. A significantly more practical amount of time in terms of verifying beam alignment.

A final, harder to quantify improvement, to SNR may be achieved by the introduction of phase cycling to the measurement. The phase cycling regime that has previously been used for echo train measurements has four phase groups, with the aim of minimising the impact of pulse artifacts and DC noise. This is suitable for application here, comparison of single measurement points in this regime requires they be spaced 4 measurements apart. Any averaging done during analysis must similarly be done over a multiple of 4 measurements.

Section 3.9: Experimental Procedure and Results:

Preparation for a hyperpolarised measurement would begin with alignment of the NMR coil with the deposition surface. The resonant frequency of the coil would be checked and if necessary, the magnetic field would be adjusted to match. With the coil in place the laser could be passed from the source to the surface to confirm that the laser was passing the coil (evidenced by illumination of the sapphire). The gas handling system would be purged 3 times with 800mbar of Argon, the O_2 trap would then be filled to 500mbar pure argon and valved sealed. A pipe was run from the O_2 trap to the inlet of a leak valve which could be opened to the inside of the NMR magnet bore. The O_2 trap was opened to this pipe with the valve initially closed. The mixing cylinder would be filled to 850mbar pure CH_4 and opened to the regulator. A gate valve between the beam profiling section of the machine and the NMR magnet would be closed and methane introduced to the source from the regulator at a pressure of 150mbar. The source nozzle would be brought into position such that the pressure at the cold cathode gauge (9. Figure 3.3.1) was maximised. The supply of methane to the nozzle would be shut off, and the gate valve opened.

Following a test measurement on the clean surface to verify the NMR system was running correctly the leak valve would be opened until a pressure rise of $1x10^{-6}$ mbar was observed in the NMR bore. The measurement would then be started taking the form of a looping measurement file using the measurement sequence outlined in the previous section. The initial 30-minute period (equivalent to ~92 loops [23 complete phase cycles]) this measurement would capture only measurements of the sapphire with the pure argon matrix depositing. Methane would then be reintroduced to the source nozzle and the measurement would capture signal with the beam depositing for a further 30 minutes. The methane supply would then be switched off and another 30 minutes of pure argon data collected. This alternating pattern continued for the duration of the measurement, typically totalling 1 hour each of both pure argon and Argon+Methane beam measurements. The mixing cylinder would be topped up with CH_4 between methane exposures, if necessary, the rate of argon depletion was not sufficient to require refilling of the O_2 trap or adjustment of the leak valve during the experiment.

Results:

The measurement sequence used was a CPMG type echo train measurement with 4 phase cycling. Raw data from a single phase takes the form of a series of echoes with real, imaginary and magnitude components. A complete 256 echo train was possible with all measurements, Figure 3.9.1 A) provides an example of the first 10 echoes from a single measurement from the initial argon-only portion of the beam. Initial signal extraction from the echo trains involves averaging over the whole train and then taking the Fourier transform, the signal could then be extracted as the mean over the peak at 0Hz (three data points at the measured resolution), subtracting the mean of the remaining points as a baseline correction. The phase cycling was constructed such that any signal would appear with the same sign and distribution over the real and imaginary components of the output data, while pulse artifacts and DC noise would cancel out when summing across phases. When considering individual measurements, it is important to only compare points from the

same part of the phase cycle. Figure 3.9.1 B) Shows the result of this over the first phase set.

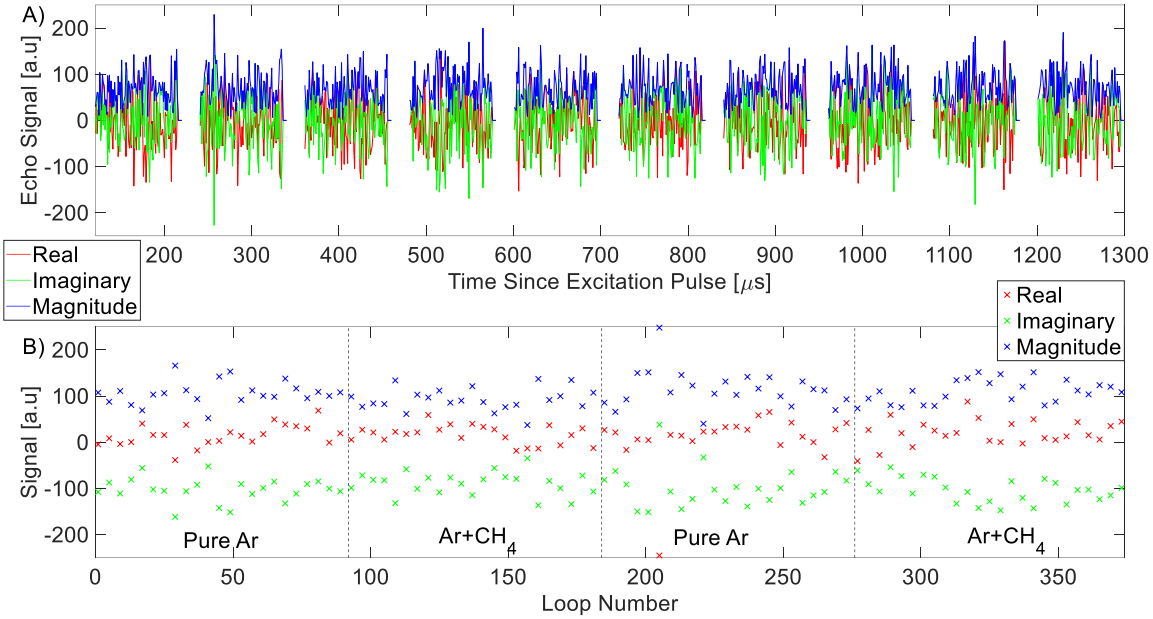

Figure 3.9.1: A) Plot of the first 10 echoes in the time domain for the first echo train in a hyperpolarised deposition measurement where only argon deposition is present. All three components of the signal, real (red), imaginary (green) and magnitude (blue) are shown. The echoes appear to just show random noise. B) Plot of the extracted signal for only trains within the first phase group over the entirety of the measurement which produced A. All three components are shown, with black dashed lines delineating periods with and without the methane beam as labelled. Signal levels appear largely flat across all regions with the real component containing very little signal, imaginary (and therefore magnitude) component contains some signal with absolute magnitude around 100 signal units.

The echoes observed in Figure 3.9.1 A) are consistent with what would be considered a “zero-signal” measurement for the apparatus. Signal appears to oscillate randomly about some fixed value over the duration of each acquisition window. With only Argon present in the bore the observed non-zero signal could be due to permanent proton contamination within the sapphire itself, proton contamination within the argon being introduced to the bore, electrical noise arising from the pulses or RF interference from some external source. If the origin is from contamination in the argon supply the signal would be expected to increase as further argon is deposited. This is not seen in Figure 3.9.1 B), in fact, the overall signal level across the entire experiment appears roughly constant. An exception occurs at loop 205, where there is a sudden spike in all three components of the signal. Analysis of the time domain signal for this data point reveals severe distortion of the signal, of the kind typically associated with coil arcing. This point may therefore be discarded as an outlier. The constancy of the signal level allows two observations to be made: Firstly, the observed small signal is intrinsic to the apparatus, ruling out argon contamination and transient rf interference. Secondly, the addition of methane to the surface does not cause an appreciable change in the observed signal.

The signal calculations in the previous section place the single echo SNR for a measurement with an inter-measurement time of 20s at a maximum of 0.069. Averaging over 256 echoes should provide a 16x increase in SNR, giving a single-

measurement SNR of: 1.1. The difference in signal between measurement points with and without CH_4 present is therefore expected to be on the level of the noise for a single measurement.

Averaging over multiple measurements should allow for further improvement of SNR, both through averaging out of random noise and subtraction of DC noise and pulse artifacts via the phase cycling regime. The greatest SNR is achieved by averaging over each region of the measurement, averaging alone in this case providing a 9.6x (sqrt 92) in SNR. Figure 3.9.2 presents Fourier transforms of the average over all echoes in all trains in each region of the experiment which produced Figure 3.9.1. The transforms are plotted side to side without subtraction of the baseline noise level to allow direct comparison.

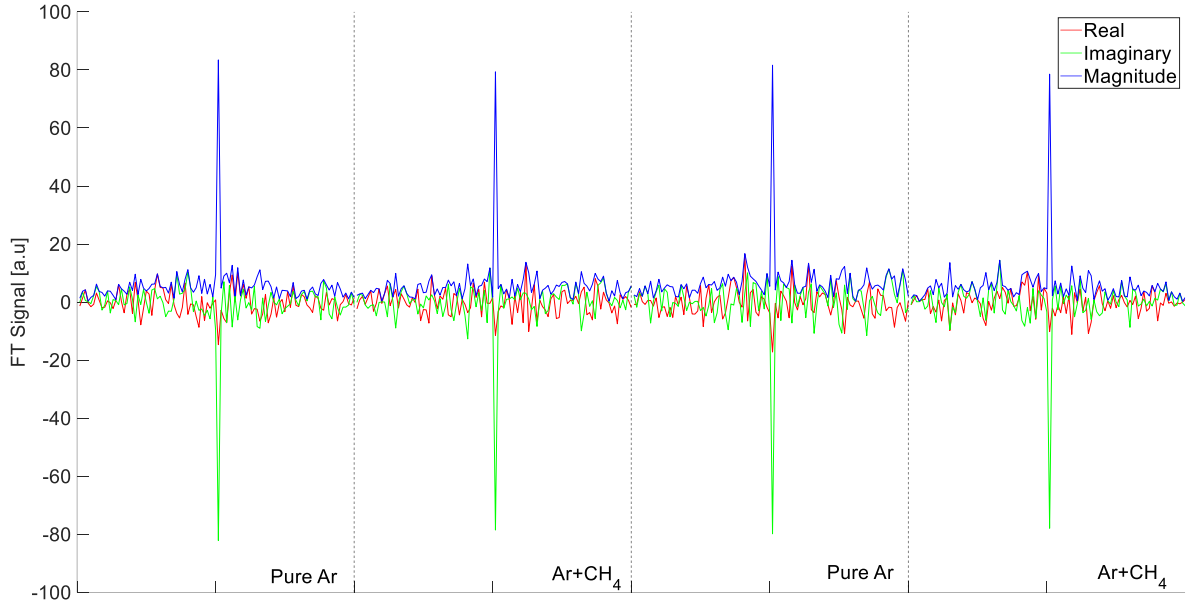

Figure 3.9.2: Average Fourier transforms over all trains within each region of the hyperpolarised deposition experiment which produced Figure 3.9.1. Baselines have been left uncorrected to provide clearer depiction of the noise level in the data. For reference, the signal values for the magnitude peak in each region, left to right are: 83.4, 79.3, 81.6 and 78.5 respectively. The magnitude of the noise regions either side of the peaks is bounded between 0 to 17 across all regions.

As noted in the caption for Figure 3.9.2, the peaks in the transforms for each region left to right are 83.4, 79.3, 81.6 and 78.5 respectively. All regions contain some signal, with the two regions where the methane beam is present having slightly lower maximum signal than the regions without. A decrease in signal with the beam on is the expected trend in the case the methane signal is competing against a larger signal arising from hydrogen spin at thermal equilibrium. The presence of some thermal equilibrium spin being a potential explanation for the pre-existing approximately constant signal seen in Figure 3.9.1. Contrary to this the second methane regions displays a lower overall signal level than the first, as does the second argon deposition. This is the opposite trend expected if the changes are due to protons from the methane beam, later measurements are expected to have higher total proton counts and therefore larger thermal equilibrium signals. Finally, the difference in signal between regions is at most 4.9 signal units. The maximum and minimum in the magnitude of the side regions of the transforms are 17 and 0

respectively, the observed differences in signal therefore fall well within the noise and the observed trends cannot be considered statistically significant.

Given the expected SNR after averaging is ~10, the only conclusion that can be drawn is that hyperpolarised NMR signal is not observable within the measurement.

Discussion:

The overall result of the hyperpolarised measurement was an inability to observe the hyperpolarised signal expected from the signal calculation. There are several possible explanations for this being the case:

Firstly, the signal calculation itself may be flawed, either in its overall construction or the values of the constants used to complete it. Of particular interest here is T_1. The value of T_1 used for the calculation was 13s, being the average of all T_1 measurements conducted on macro-deposited samples at a concentration of ~6%CH_4@Ar and a deposition temperature of 5K. T_1 is generally regarded [ref] as descriptive of the local environment of the spin under study. The concentration of methane in the matrix under deposition is expected to be well under 6%. Treating Argon as an ideal gas, at room temperature a pressure of $1x10^{-6}$ mbar would be roughly equivalent to an impingement rate of $2.44x10^{18}$ molecules/m^2s. Over the ~24mm^2 surface of the sapphire gives Φ_{Ar} = $5.18x10^{13}$ molecules per second. Taking this and Φ_m allows the final methane concentration to be calculated as $\frac{\Phi_m}{\Phi_m+\Phi_{Ar}}$ equating to ~1.4%, more than 3x lower than the concentration initially tested. The increased methane-methane distance within the sample this represents could change its NMR characteristics, making the signal level calculation incorrect and choice of repetition time for the measurement suboptimal.

Secondly, the hyperpolarised methane may not be depositing on the surface. This is unlikely to be due to methane not sticking, the macro-deposition experiments discussed in Section 3.8 clearly evidence sticking of methane within the matrix at 5K. More likely is either a misalignment of the beam and the surface, or loss of hyperpolarisation between the point the methane leaves the hexapole and the point that it is measured.

With regards to misalignment, the beam profiles conducted in Section 3.6 confirmed that the laser is reasonable indicator for the position the molecular beam will strike. However, while illumination of the sapphire with the laser was confirmed before the beginning of each HPD experiment it was not possible to accurately determine -how- the sapphire was being illuminated. The sapphire itself is transparent, mounted with its back to a highly polished and reflective copper surface. The surface itself is mounted at a 45-degree angle to the incoming laser beam. Further to this, the illumination of the sapphire could only be observed from a single direction. It is possible to envision a scenario where some small portion of the laser, or even a portion of reflected light from the laser striking elsewhere, could be reflected through the sapphire towards the viewport, leading to a false belief that the surface was well aligned. In the ideal case the laser travels through the centre of the NMR and strikes the sapphire, but the sapphire could appear illuminated even if the laser was striking the coil and reflecting down towards it. The issue could be addressed in future by

using a more quantitative method of assessing alignment, such as a photodiode mounted beneath the sapphire itself.

With regards to loss of polarisation, the state of the methane could change at multiple points along the beam path. Section 3.2 referred to measurements with hydrogen[33-36] which were dependent on a clear understanding of the magnetic field profile along the entire length of the magnetic molecular interferometer, along with the magnetic Hamiltonian governing the evolution of the *mimj* states within the beam. Neither an accurate magnetic profile of the NMR beamline, nor a complete magnetic Hamiltonian for methane is available. Small solenoidal coils producing a field of ~20 Gauss at the centre of the beamline and midpoint of two coils were installed along the line to ensure that the dominant magnetic field within *should* be aligned with the NMR magnet field, but the impact of these fields on the projection states within the beam during propagation has not been assessed by simulation. Further to this, there is little understanding in literature regarding whether the projection state of the molecule is conserved during the sticking process. IR measurements on a water-in-krypton system using a similar hexapole setup have shown preservation of spin polarisation on deposition from a molecular beam[52], but similar measurements have not been conducted for methane in argon.

Chapter 4: Summary and Outlook:

Section 4.1: Overview:

The stated aim of the thesis in the introduction was twofold. To demonstrate the feasibility of measuring nuclear spin conversion using MIS NMR, and secondly, to measure signal from hyperpolarised molecules deposited from a magnetically focussed molecular beam.

With regards to NSC measurements, the ability to measure NSC of H_2O@Ar with NMR has been demonstrated and the extracted time constants for cooling experiments are on a similar order of magnitude to those observed in other studies on similar systems[5, 11]. Difficulty was encountered in fitting heating experiments due to low signal to noise. Further development of the techniques should focus on increasing the signal to noise level. This would have benefits both for cooling experiments (in the form of reduced uncertainty) and would allow for easier fitting of the heating data. The application of measurements with a greater resolution in time would allow for better understanding of the rapid phenomena observed immediately following temperature jumps observed in Section 2.9. These phenomena are not observed in IR data[5], and only briefly considered in NMR data regarding H_2O@C_{60}[11, 12]. Finally, improvements to the deposition setup allowing for measurements at different concentrations would make discerning the molecularity of the mechanism easier.

With regards to hyperpolarised measurements, no hyperpolarised signal was observed above the noise floor of the experiment. The potential reasons for this lack of hyperpolarised signal were numerous, including technical issues such as potential loss of hyperpolarisation beyond the end of the hexapole, potential misalignment and overall low signal to noise, as well as the more fundamental question of whether hyperpolarisation is preserved during adsorption to the surface.

Providing a more definite answer to this question would require ruling out all other potential causes for lack of signal, something that would require significant additional investigation and was beyond the scope of this thesis. Alignment can be tested with additional rounds of beam profiling. During their construction of the third arm of the molecular interferometer, a previous PhD student in the group performed 2 dimensional scans of the magnetically focussed hydrogen beam used on that system[53], revealing that the real beam deviated from the ideal circular cross section. The profiling setup on the NMR apparatus should be capable of similar measurements, provided a more long-lived source of methane than the mixing cylinder could be introduced to the system. The resultant profile would be insightful for assessing whether the beam is performing as expected. It would also allow for further validation of the hexapole model, as it should be possible to simulate the cross section.

Understanding of the evolution of the states within the methane beam and how they arrive at the surface would require understanding and adaptation of the available literature on the methane magnetic Hamiltonian[50] into a numerical simulation code which calculates quantum mechanically the propagation of the spin and rotation

quantum states through the magnetic field the molecules pass through, from the hexapole until they reach the sample, in a similar manner as is currently done for the H_2 beam on the molecular interferometer[33]. This would also require measurement of all three cartesian components of the magnetic field profile from the end of the hexapole to the deposition surface[53]. The only way to eliminate signal to noise as a cause would be to improve the overall signal to noise of the machine (through further iterations of coil and measurement sequence design), finally, determination of whether hyperpolarisation is lost on absorption could only be made when the other potential factors had been mitigated.

While the level analysis performed in Section 3.8 suggest that the hyperpolarised signal should be unambiguously detectable, improving the SNR of the setup further would be beneficial for all measurements the apparatus performs. With specific regard to the hyperpolarised signal, if the lack of detection is due to only some small fraction of the beam arriving at the surface, or loss of a significant proportion of the polarisation on adsorption then enhancing the system NMR would give a better chance of detecting it. It is easiest to optimise the molecular beam when it can be directly detected, improving the SNR would give a better chance of achieving this.

An issue which proved prohibitively troublesome for both experiments was coil arcing. This limited the voltage the coil could be supplied with, requiring longer pulses (with shorter bandwidth) and sub-optimal tip angles. One way to address this issue would be to find a coil geometry that requires lower voltages to achieve sufficient fields at the sample, though what form such a coil would take is up for debate. A potentially promising option is the planar surface coil, discussed later in Section 4.3.

With regards to future work, there are several avenues that could be taken. The remainder of this short chapter will cover some promising examples, in order of increasing modification to the extant apparatus.

Section 4.2: Change of Sample: Hydrogen NSC

While NSC in water is a field of active study, it is but one of many molecules of interest that undergoes nuclear spin conversion. Ordinary di-hydrogen, which in the introduction was used to demonstrate the concept of spin isomerism, is another example. Interest in $^1H_2$ NSC originates from the fields of astrophysics and energy storage[54], with NSC being studied in a wide range of systems with a variety of methods, including MIS and molecular-cage[54] studies with NMR, Raman and Infrared[55-57] spectroscopy.

Conversion times in rare gas matrices have been observed to be long with NSC seeming to only progress immediately following deposition[58]. Conversely NSC in other solids, such as CO_2 has been observed to be comparatively rapid[55, 57]. With explanations for this behaviour still being developed, more data regarding H_2 NSC could only be beneficial.

With regards to hyperpolarisation, the generation and control of non-thermal equilibrium molecular beams of $^1H_2$ is arguably the Swansea Surface Dynamics research groups area of expertise[33-36]. As previously mentioned, accurately

modelling the evolution of the methane molecular wavefunction as it travelled from source to surface would require the construction of a completely new model. This would not be the case for hydrogen. If the magnetic field profile of the beamline were accurately mapped then the same numerical tools used in the simulation and understanding of experiments on the magnetic molecular interferometer could be applied to the NMR apparatus.

Hydrogen does have some downsides, most notably being explosive if improperly handled. Further to this, the small size of the hydrogen molecule limits the temperature range it can be studied under, being capable of diffusive motion in rare gas matrices above ~15K. Further to this, in accordance with (Eq. 3.4.1) a room temperature beam of hydrogen would be traveling significantly faster than a methane beam, leading to less time spent in the hexapole and poorer focussing. Properly focusing a hydrogen beam using the existing hexapole (which was designed for the heavier, slower methane) would require either direct cooling of the nozzle or seeding in a denser carrier gas.

Section 4.3: Modification of apparatus: Surface Coils:

In both types of experiment presented in this work, the NMR coils employed have been simple 2 or 3 turn loops with an internal diameter of ~6mm. The exact shape of the samples under study has been difficult to determine, to the eye samples appear disc like, with diameter matching the deposition surface and a thickness of a few mm. While the coils used here were sufficient to transmit and receive signals at the desired frequency, little direct thought or analysis was devoted to optimising them beyond this point.

The adaptation of NMR coil geometry and electronics is a field as wide as an ocean and comparatively as deep. One geometry, currently under study for use in MRI at short penetration depths[59], and in the NMR study of thin samples[60] is the surface coil. In their simplest form these are planar spirals of conducting material, which are most sensitive immediately at their surface with said sensitivity rapidly dropping off as distance from the surface increases, the effect being more noticeable in smaller coils (see for example Fig 4 of [59]).

As a result, these coils are particularly well suited to the study of thin films, as the entirety the sample may be placed near the coil. The proposed change to the apparatus would be the replacement of the wound coils with a planar spiral coil at the deposition surface. This may be either on the vacuum side of the surface, or on the cold head facing side of a suitably thin (ensuring the sensitive region of the coil still penetrates the sample) deposition plate. Assuming sapphire is again chosen as the surface material, the latter may offer benefits in terms of reducing coil arcing (as the coil is not directly exposed to deposition gas) though the impacts of reducing the thermal contact area between the plate and the cold finger would have to be assessed.

Potential gains in signal are difficult to quantify numerically without further investigation / modelling, although there is anecdotal evidence from this work that deposition directly on to the coil leads to very high signal levels. In some of the (failed, due to arcing) deposition icing was visible on the solenoidal coil, and what

signal was measurable from the depositions was of exceptionally high signal to noise.

A further benefit to a planar coil design is specifically relevant to the hyperpolarised experiment. The solenoidal coil required the sample and probe be oriented at 45º to the static field (rather than the ideal 90º) to give the best chance of the beam passing through the coil and reaching the surface. With the coil on the deposition surface plane, while the surface would still have to be off-perpendicular for the beam to strike it and deposit the angle could be much shallower (albeit with the consideration that the shallower the angle the more the nominally circular depositing beam front would be “smeared” into an ellipse).

Section 4.4: Modification of the apparatus: Deposition System:

In characterisation of both H2O@Ar and CH4@Ar samples, different samples generated under nominally identical conditions were noted to exhibit variance in NMR characteristics. Furthermore, for water control over sample concentration was greatly limited by apparent condensation of water vapour along the deposition line.

For water then the most obvious improvement that could be made would be temperature control for both the deposition nozzle and the entirety of the feed line running up to it. This would most simply be achieved by wrapping said lines with resistive heating elements and insulation. Keeping the lines at a temperature with a vapour pressure of water above that which is supplied from the mixing cylinder should ensure that loss of water vapour to the walls of the lines and nozzle, allowing for multiple water concentrations to be employed and greater confidence in the water concentration within the sample. This would however introduce additional concerns regarding potential heating of the deposition surface from the nozzle.

An improvement which would benefit all kinds of depositions would be the stabilisation and quantisation of the relative positions of surface and nozzle within the magnet bore. While both can be nominally fixed in place, the deposition surface notably wandered following cleaning cycles, with relative positioning of the nozzle with respect to the surface being achieved qualitatively using a camera feed from a single perspective. The introduction of a camera feed from a second perspective, alongside the introduction of marked fixed reference points within the bore and at the ends of the nozzle and cold finger would theoretically allow the absolute positions of both within said bore to be calculated. This would be aided by the introduction of more sophisticated manipulators at the rear of the cold finger and input of the nozzle. Both currently rely on ungraduated port aligners, with the nozzle having an additional ungraduated linear feed to control insertion depth. Replacement of any of these features with graduated x/y/z manipulators would allow more quantitative positioning of both elements.

Section 4.5: Reconstruction of apparatus: Combined NMR/IR

This final avenue for research would require significant, costly and work intensive changes to the apparatus and is presented largely as an aspirational discussion. The baseline of the argument is this: NMR and IR techniques do not have any requirements that make them mutually exclusive. NSC requires both a change in

spin (a spin flip) and a change in rotational energy, NMR is sensitive to the first, while IR and Raman are sensitive to the latter. A machine which could simultaneously measure both would provide a more complete insight into the underlying processes.

As an example: in IR it is possible to clearly distinguish signal from single monomers of water as sharp peaks[5] while dimers and aggregates appear as a broad poorly defined peak. At the fields and sensitivities, the machine currently works at, all water signal appears as a single peak. By fitting NSC curves to a cooling experiment on the same sample using both IR and NMR, it should be possible to identify the component in the NMR decay which matches the monomer-only decay in the IR measurement. Any remaining component could then be attributed to the multimers. This opens the doorway to investigating the correlation between the proportion of multimers in the sample and the monomer NSC rate. Further to this, IR and NMR struggle at different ends of the concentration spectrum for water. IR works best at low concentrations where the peaks are easily differentiable (low multimer count), while NMR requires higher concentrations to produce detectable signal. By running both simultaneously correlations between the two can be used to reinforce the conclusions taken from the technique which performs worse under the given conditions.

The requirements for NMR NSC studies have been briefly covered in both Chapter 1 & Chapter 2. The requirements for an IR study depend on the type of IR spectroscopy being undertaken. These may loosely be categorised by how the IR laser light interacts with the sample and reaches the detector. The IR NSC studies cited in this work have all employed reflective IR, the samples being deposited on polished mirrors, the IR light introduced at an angle to the sample, passing through it, reflecting, passing through the sample again and reaching the detector.

The current NMR setup has very limited space in-bore, while mounting a deposition surface with a reflective face would be a minor modification, but the tight spatial constraints make allowing for IR light to enter and reflect complicated. This would be less of a concern were the planar spiral coil to be implemented, as there would be significantly less competition for space within the bore.

Alternative modes of IR are transmission and attenuated total reflectance (ATR). In the first light passes directly through the sample to a detector, while in the latter IR radiation is introduced to the interface between the sample and a crystal which is strongly refractive at the frequency of IR used. Some of the IR is absorbed by the sample, while the remainder reflects and is detected.

Both cases would likely best be served by a modification to the cold finger. The introduction of an IR transmissive fibre optic along the centre of the cold finger would allow for direct introduction or collection of IR radiation from the surface. The deposition surface would have to be constructed of a suitably transmissive (or in the case of ATR refractive) material, but this would provide a collection / transmission pathway which was independent of any other obstructions within the bore. Transmission based measurements would likely be restricted to ones where the laser is passed along the line typically reserved for the hyperpolarised beam (meaning the setup would be unsuitable for HPD measurements).

Much as was the case for planar coils, an ATR setup is appealing for its applicability to thin samples, this type of spectroscopy being most sensitive to the interface between the refractive crystal and the sample under study. A drawback here is that should the behaviour of molecules at the interface differ greatly from those in the bulk material it will not provide an accurate view into the behaviour of the bulk.

A good candidate for a feasibility study, regardless of the chosen IR method, would be an attempt to repeat the water NSC measurements conducted in this thesis with both NMR and IR simultaneously.

References:

1. Telkki, V.V. and V.V. Zhivonitko, *Ultrafast NMR diffusion and relaxation studies*, in *Annual Reports on Nmr Spectroscopy, Vol 97*, G.A. Webb, Editor. 2019. p. 83-119.
2. Feng, L. and H. Chandarana, *Accelerated Abdominal MRI: A Review of Current Methods and Applications.* Journal of Magnetic Resonance Imaging, 2025.
3. Vahlensieck, M., *MRI of the shoulder.* European Radiology, 2000. **10**(2): p. 242-249.
4. Behzadmehr, R. and M. Salarzaei, *THE ROLE OF MRI IN PATIENTS WITH OSTEOARTHRITIS -A REVIEW ARTICLE.* Indo American Journal of Pharmaceutical Sciences, 2017. **4**(9): p. 2745-2747.
5. Pardanaud, C., *Etude de la conversion de spin nucléaire de l'eau en matrices de gaz rares : mesures, modélisation de l'influence des interactions spinspin intermoléculaires et contexte astrophysique.* . 2007, Sorbonne Université.
6. Lekic, A., *Etude de la conversion de spin nucléaire du méthane en matrices d'Argon et de Krypton*. 2011, Sorbonne Université.
7. Atkins, P., J. De Paula, and J. Keeler, *Atkins' Physical Chemistry, 12th edition*. 2023, New York: Oxford University Press.
8. Hougen, J.T. and T. Oka, *Nuclear Spin Conversion in Molecules.* Science, 2005. **310**(5756): p. 1913-1914.
9. Cacciani, P., J. Cosléou, and M. Khelkhal, *Nuclear spin conversion in H2O.* Physical Review A, 2012. **85**(1).
10. Dello Russo, N., et al., *Water production rates, rotational temperatures, and spin temperatures in comets C/1999 H1 (Lee), C/1999 S4, and C/2001 A2.* Astrophysical Journal, 2005. **621**(1): p. 537-544.
11. Mamone, S., et al., *Nuclear spin conversion of water inside fullerene cages detected by low-temperature nuclear magnetic resonance.* Journal of Chemical Physics, 2014. **140**(19).
12. Meier, B., et al., *Spin-Isomer Conversion of Water at Room Temperature and Quantum-Rotor-Induced Nuclear Polarization in the Water-Endofullerene $H_2O@C_{60}$.* Physical Review Letters, 2018. **120**(26).
13. Wespiser, C., et al., *Ro-translational dynamics of confined water. I. The confined asymmetric rotor model.* Journal of Chemical Physics, 2022. **156**(7).
14. Levitt, M.H., *Spin Dynamics: Basics of Nuclear Magnetic Resonance*. 2nd ed. 2008: Wiley.
15. Keeler, J., *Understanding NMR Spectroscopy*. 2nd ed. 2011: Wiley.
16. Young, H., D. and R. Freedman, A., *University Physics with Modern Physics*. 14th, Global ed. 2016: Pearson.
17. Greenberg, Y.S., *Application of superconducting quantum interference devices to nuclear magnetic resonance.* Reviews of Modern Physics, 1998. **70**(1): p. 175-222.
18. Augustine, M.P., D.M. TonThat, and J. Clarke, *SQUID detected NMR and NQR.* Solid State Nuclear Magnetic Resonance, 1998. **11**(1-2): p. 139-156.
19. McDermott, R., et al., *SQUID-detected magnetic resonance imaging in microtesla magnetic fields.* Journal of Low Temperature Physics, 2004. **135**(5-6): p. 793-821.
20. Ahmad, S.F., et al., *Recent Progress in Birdcage RF Coil Technology for MRI System.* Diagnostics, 2020. **10**(12).

21. Hahn, E.L., *Spin Echoes.* Physical Review, 1950. **80**(4): p. 580-594.
22. Carr, H.Y. and E.M. Purcell, *Effects of Diffusion on Free Precession in Nuclear Magnetic Resonance Experiments.* Physical Review, 1954. **94**(3): p. 630-638.
23. Herzberg, G., *Molecular Spectra and Molecular Structure II: Raman and Infrared Spectra of Polyatomic Molecules*. 1945: Lancaster Press.
24. Ridge, C.D., L.F. O'Donnell, and J.D. Walls, *Long-lived selective spin echoes in dipolar solids under periodic and aperiodic π-pulse trains.* Physical Review B, 2014. **89**(2).
25. Eills, J., et al., *Spin Hyperpolarization in Modern Magnetic Resonance.* Chemical Reviews, 2023. **123**(4): p. 1417-1551.
26. Halse, M.E., *Perspectives for hyperpolarisation in compact NMR.* Trac-Trends in Analytical Chemistry, 2016. **83**: p. 76-83.
27. Green, R.A., et al., *The theory and practice of hyperpolarization in magnetic resonance using para-hydrogen.* Progress in Nuclear Magnetic Resonance Spectroscopy, 2012. **67**: p. 1-48.
28. Adams, R.W., et al., *Reversible Interactions with para-Hydrogen Enhance NMR Sensitivity by Polarization Transfer.* Science, 2009. **323**(5922): p. 1708-1711.
29. Ni, Q.Z., et al., *High Frequency Dynamic Nuclear Polarization.* Accounts of Chemical Research, 2013. **46**(9): p. 1933-1941.
30. Gerlach, W. and O. Stern, *Der experimentelle Nachweis der Richtungsquantelung im Magnetfeld.* Zeitschrift für Physik, 1922. **9**(1): p. 349-352.
31. Schmidt-Böcking, H., et al., *The Stern-Gerlach experiment revisited.* European Physical Journal H, 2016. **41**(4-5): p. 327-364.
32. Jardine, A.P., et al., *Hexapole magnet system for thermal energy ^{3}He atom manipulation.* Review of Scientific Instruments, 2001. **72**(10): p. 3834-3841.
33. Alkoby, Y., et al., *Setting benchmarks for modelling gas-surface interactions using coherent control of rotational orientation states.* Nature Communications, 2020. **11**(1).
34. Godsi, O., et al., *A general method for controlling and resolving rotational orientation of molecules in molecule-surface collisions.* Nature Communications, 2017. **8**.
35. Chadwick, H., et al., *Stopping molecular rotation using coherent ultra-low-energy magnetic manipulations.* Nature Communications, 2022. **13**(1).
36. Chadwick, H. and G. Alexandrowicz, *Measuring surface phonons using molecular spin-echo.* Physical Chemistry Chemical Physics, 2022. **24**(23): p. 14198-14208.
37. Lowe, M., et al., *Neutral beam microscopy with a reciprocal space approach using magnetic beam spin encoding.* Nature Communications, 2024. **15**(1).
38. Kravchuk, T., et al., *A Magnetically Focused Molecular Beam of Ortho-Water.* Science, 2011. **331**(6015): p. 319-321.
39. Baranovsky, E., *Magnetically manipulated molecular beams: studying the structure and dynamics of water surfaces*. 2016, Technion - Israel Institute of Technology.
40. Ramsey, N.F., *Theory of Molecular Hydrogen and Deuterium in Magnetic Fields*.* Physical Review, 1952. **85**(1): p. 60-65.
41. Krüger, C., et al., *A magnetically focused molecular beam source for deposition of spin-polarised molecular surface layers.* The Journal of Chemical Physics, 2018. **149**(16).

42. Amrein, A., M. Quack, and U. Schmitt, *High-Resolution Interferometric Fourier-Transform Infrared-Absorption Spectroscopy in Supersonic Free Jet Expansions - Carbon-Monoxide, Nitric-Oxide, Methane, Ethyne, Propyne, and Trifluoromethane.* Journal of Physical Chemistry, 1988. **92**(19): p. 5455-5466.
43. Hepp, M., G. Winnewisser, and K.M.T. Yamada, *Conservation of the Nuclear-Spin Modification of CH_4 in the Cooling Process by Supersonic Jet Expansion.* Journal of Molecular Spectroscopy, 1994. **164**(1): p. 311-314.
44. Hippler, M. and M. Quack, *High-resolution Fourier transform infrared and cw-diode laser cavity ringdown spectroscopy of the v_2+2v_3 band of methane near 7510 cm^{-1} in slit jet expansions and at room temperature.* Journal of Chemical Physics, 2002. **116**(14): p. 6045-6055.
45. Setzmann, U. and W. Wagner, *A New Equation of State and Tables of Thermodynamic Properties for Methane Covering the Range from the Melting Line to 625K at Pressures up to 1000-MPa.* Journal of Physical and Chemical Reference Data, 1991. **20**(6): p. 1061-1155.
46. Rogdakis, E.D. and P.A. Lolos, *Simple generalized vapour pressure-and boiling point correlation for refrigerants.* International Journal of Refrigeration-Revue Internationale Du Froid, 2006. **29**(4): p. 632-644.
47. Friend, D.G., J.F. Ely, and H. Ingham, *Thermo-Physical Propteries of Methane.* Journal of Physical and Chemical Reference Data, 1989. **18**(2): p. 583-638.
48. Vermette, J., et al., *Quantum State-Resolved Characterization of a Magnetically Focused Beam of ortho-H2O.* The Journal of Physical Chemistry A, 2019. **123**(42): p. 9234-9239.
49. Scoles, G., *Atomic and molecular beam methods*. Vol. 1. 1988, New York: Oxford University Press.
50. Anderson, C.H. and N.F. Ramsey, *Magnetic Resonance Molecular-Beam Spectra of Methane.* Physical Review, 1966. **149**(1): p. 14-24.
51. Chambers, A.F., R K.; Halliday, R S. , *Basic Vacuum Technology, Second Edition*. 2 ed. Vol. 1. 1998, Institute of Physics Publishing, Dirac House, Temple Back, Bristol BS1 6BE, UK: Institute of Physics Publishing.
52. Turgeon, P., A., et al., *Preparation, isolation, storage and spectroscopic characterisation of water vapor enriched in the ortho-H_2O nuclear spin isomer.* Physical Review A, 2012. **86**(6): p. 062710.
53. Alkoby, Y., *Studying Molecule-Surface Interactions Using Magnetically Manipulated Molecular Beams*, in *College of Science, Department of Chemistry*. 2021, Swansea University.
54. Ilisca, E., *Hydrogen Conversion in Nanocages.* Hydrogen, 2021. **2**(2): p. 160-206.
55. Ueta, H., K. Fukutani, and K. Yamakawa, *Fast ortho-to-para conversion of molecular hydrogen in chemisorption and matrix-isolation systems.* Frontiers in Chemistry, 2023. **11**.
56. Yamakawa, K. and K. Fukutani, *Nuclear Spin Conversion of H2, H2O, and CH4 Interacting with Diamagnetic Insulators.* Journal of the Physical Society of Japan, 2020. **89**(5).
57. Yamakawa, K., et al., *Fast nuclear-spin conversion of H2 trapped and polarized in a CO2 matrix.* Physical Review B, 2020. **102**(4).
58. Alikhani, M.E., et al., *Reinvestigation of the Raman-Spectra of Dihydrogen Trapped in Rare-Gas Solids .1. H-2, HD, and D2 Monomeric Species.* Journal of Chemical Physics, 1989. **90**(10): p. 5221-5231.

59. Massin, C., et al. *Magnetic Resonance Imaging using microfabricated planar coils*. in *2nd Annual International IEEE/EMBS Conference on Microtechnologies in Medicine and Biology*. 2002. Madison, Wi.
60. Liu, W., L. Lu, and V. Mitrovic, *Application of surface coil in nuclear magnetic resonance studies of physical properties of quasi-2D materials.* Review of Scientific Instruments, 2017. **88**(11).